Evolution, interaction, and intrinsic properties of dislocations in intermetallics: Anisotropic 3D dislocation dynamics approach

by

Qian Chen

A dissertation submitted to the graduate faculty

in partial fulfillment of the requirements for the degree of

DOCTOR OF PHILOSOPHY

Major: Materials Science and Engineering

Program of Study Committee:
Bulent Biner, Major Professor
Alan M. Russell
Xiaoli Tan
Ashraf Bastawros
Ambar K. Mitra

Iowa State University

Ames, Iowa

2008

TABLE OF CONTENTS

LIST OF TABLES

LIST OF FIGURES

ACKNOWLEDGEMENTS

First of all, I would like to express my sincere gratitude to my supervisor, Dr. Bulent Biner, for his guidance, patience, understanding and encouragement over the past five years, all of which have definitely lent a solid foundation for the present thesis. His well-rounded knowledge on computational material science and logic way of thinking to solve research problems have been of great value for me. He is responsible for involving me into this 3D anisotropic dislocation dynamics project at the first place. He taught me how to develop skills on analyzing and solving problems in my research work as well as make decent scientific writings. And more importantly, he always encouraged me to be persistent to accomplish any goal. I cordially acknowledge his generous help during my graduate studies at Iowa State University.

I'm also very grateful for each doctoral committee member, Prof. Alan M. Russell, Prof. Xiaoli Tan, Prof. Ashraf Bastawros, and Prof. Ambar Mitra, for their continuous support and encouragement.

I would like to thank Dr. Cai-Zhuang Wang, Prof. Kai-ming Ho, and Dr. Min Ji for their meaningful discussion and suggestion on my research project regarding the 2D generalized P-N model. And I'm also grateful for the assistance and guidance on the methodology of kinetic Monte Carlo simulation I obtained from Dr. Xiang-Yang Liu.

Additionally, I'm indebted to Prof. Thomas Rudolphi and Prof. Richard Lesar for their guidance on overall computational modeling methods on materials science.

Last but not least, I would like to express my special gratitude to my family: my husband, Hesong Cao, my parents, Xiaoyong Wang and Naixin Chen, and my brother, Keyu Chen. I would not have accomplished my research work without your care and support.

ABSTRACT

The generation, motion, and interaction of dislocations play key roles during the plastic deformation process of crystalline solids. 3D Dislocation Dynamics has been employed as a mesoscale simulation algorithm to investigate the collective and cooperative behavior of dislocations. Most current research on 3D Dislocation Dynamics is based on the solutions available in the framework of classical isotropic elasticity. However, due to some degree of elastic anisotropy in almost all crystalline solids, it is very necessary to extend 3D Dislocation Dynamics into anisotropic elasticity. In this study, first, the details of efficient and accurate incorporation of the fully anisotropic elasticity into 3D discrete Dislocation Dynamics by numerically evaluating the derivatives of Green's functions are described. Then the intrinsic properties of perfect dislocations, including their stability, their core properties and disassociation characteristics, in newly discovered rare earth-based intermetallics and in conventional intermetallics are investigated, within the framework of fully anisotropic elasticity supplemented with the atomistic information obtained from the *ab initio* calculations. Moreover, the evolution and interaction of dislocations in these intermetallics as well as the role of solute segregation are presented by utilizing fully anisotropic 3D dislocation dynamics. The results from this work clearly indicate the role and the importance of elastic anisotropy on the evolution of dislocation microstructures, the overall ductility and the hardening behavior in these systems.

CHAPTER 1

INTRODUCTION

Plasticity is one of the most important features of crystalline solids and results from the relative sliding of one set of atoms in a certain crystallographic plane (slip plane) along a certain direction (slip direction) over the atoms in an adjacent crystallographic plane. There are certain slip planes and slip directions for each different crystal structure. For instance, for face-centered cubic (fcc) crystal structure, the slip direction is usually toward <110> directions on {111} slip planes; for body-centered cubic (bcc) structure, the normal slip directions and slip planes are <111> directions and {110} or {112} planes. In general, slip planes and slip directions correspond to close-packed planes and directions of the crystal structure. In 1926, Frenkel [1] first calculated the shear stress required to perform this relative gliding behavior. The schematic figure of the atomic arrangement is illustrated in Figure 1.1. a and b are the distance between two rows of atoms and the spacing of atoms in the direction of the shear stress, respectively. x is the distance apart from the equilibrium positions.

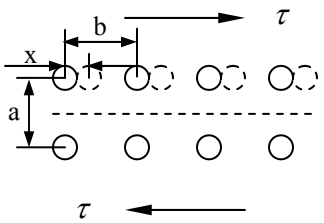

Figure 1.1 Schematic atomic positions used to calculate theoretical critical shear stress.

Under the shear stress, the atoms deviate from their equilibrium positions and result in an increase of the energy. It was assumed that the change of energy is the cosine function of position x and the resulting force can be expressed as

$$F = \frac{\mu b}{2\pi a}\sin\frac{2\pi x}{b} \tag{1.1}$$

where μ is the shear modulus. Then the critical shear stress is

$$\tau = \frac{\mu b}{2\pi a} \tag{1.2}$$

With the assumption of $b \approx a$, the critical shear stress can be given further as

$$\tau = \frac{\mu}{2\pi} \tag{1.3}$$

Obviously, the calculated results from this simple approach are many orders of magnitude larger than the real values obtained from the experiments. This significant difference motivated many researchers to consider the already pre-existence of defects (dislocations) in real crystals. The works of Taylor [2], Orowan [3], and Polanyi [4] in 1930s can be regarded as the foundations of the modern dislocation theory. They thought that the relative displacements of two parts of crystals across the glide plane result from the atomic movements of the dislocations which are spread continuously on the glide plane as shown in Figure 1.2, rather than the results of the motion of blocks of atoms simultaneously. The dislocation theory accounted for the large difference between real shear strength and theoretical one and was verified further with the direct observation of dislocations by Transmission Electron Microscopy (TEM).

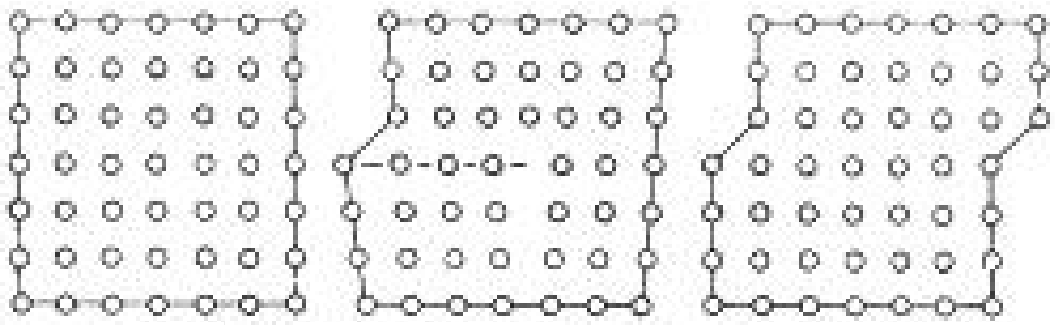

Figure 1.2 Atomic positions when a dislocation passes through a crystal [2].

1.1 Geometry of dislocations and Burgers vector

The dislocation discussed before can be formed by introducing an extra half atomic plane into the crystal, as shown in Figure 1.3(a). The line *DC* is called a *positive edge* dislocation and designated with sign $\perp$. If the extra half atomic plane is inserted below the glide plane, a *negative edge* dislocation is obtained and represented by $\top$. To define an arbitrary dislocation quantitatively, the concept of *Burgers vector* was introduced [5]. For an edge dislocation, the definition of Burgers vector is illustrated in Figures 1.3(b) and 1.3(c). A Burgers circuit shown in Figure 1.3(b) is a closed atom-to-atom path around a dislocation taken in a crystal. If the same atom-to-atom path is now made without any dislocations in a perfect crystal as shown in Figure 1.3(c), the same loop cannot be closed. The vector required to close this circuit is called *Burgers vector.* Thus the Burgers vector of an edge dislocation is always perpendicular to the dislocation line.

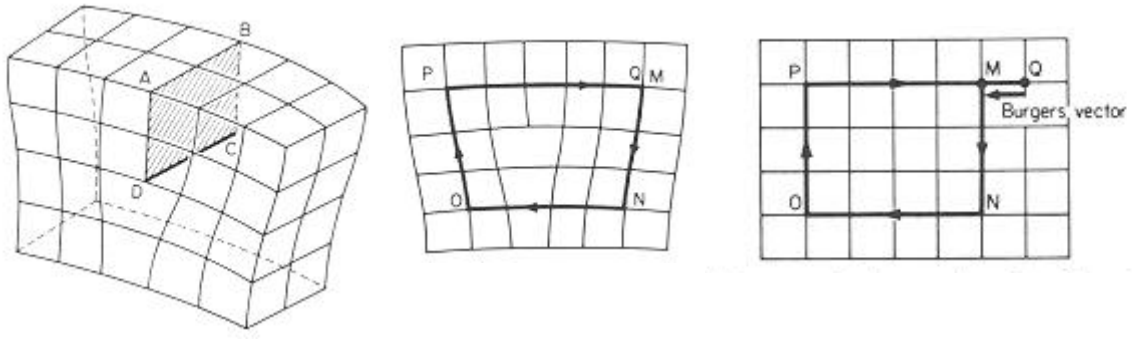

(a) (b) (c)

Figure 1.3(a) Forming a positive edge dislocation;
(b) and (c) definition of the Burgers vector of a edge dislocation [6].

As seen in Figure 1.4(a), if the displacements in the crystals are on the one side of the glide plane relative to the other side one atom lattice distance along the arrow direction, a dislocation line is also generated along the intersection line between the regions with slip and without slip. But the atomic plane is no longer a flat surface but a helicoid. Therefore, this dislocation type is called *screw* dislocation. The Burgers vector of a screw dislocation can also be defined by a Burgers circuit as shown in Figures 1.4(b) and 1.4(c).

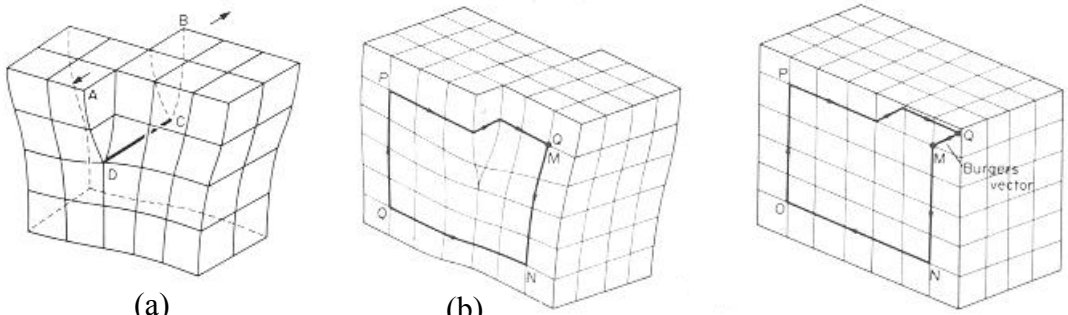

(a) (b) (c)

Figure 1.4(a) Forming a screw dislocation;
(b) and (c) definition of the Burgers vector of a screw dislocation [6].

Moreover, when a dislocation line forms an arbitrary angle with its Burgers vector, the dislocation character is mixed, which can be decomposed into pure edge and pure screw components.

1.2 Elastic properties of dislocations

1.2.1 Stress field of a dislocation

In the isotropic media, consider the line of a straight dislocation with infinite length along the z-axis and located at the origin ($x = 0$; $y = 0$). In rectangular coordinate system, the stress components of a screw dislocation can be expressed as given in [7]:

$$\begin{aligned}
&\sigma_{xz} = \sigma_{zx} = -\frac{\mu b}{2\pi}\frac{y}{x^2 + y^2} \\
&\sigma_{yz} = \sigma_{zy} = \frac{\mu b}{2\pi}\frac{x}{x^2 + y^2} \\
&\sigma_x = \sigma_y = \sigma_z = \sigma_{xy} = \sigma_{yx} = 0
\end{aligned} \tag{1.4}$$

where μ is the shear modulus. The stress field of an edge dislocation is more complex than that of a screw dislocation. The straight dislocation line is still put along the z-axis with infinite length and its Burgers vector is along x-direction. Thus the stress components of an edge dislocation within the framework of isotropic elasticity are given as [7]:

$$\begin{aligned}
&\sigma_x = -\frac{\mu b}{2\pi(1-\nu)}\frac{y(3x^2 + y^2)}{(x^2 + y^2)^2} \\
&\sigma_y = \frac{\mu b}{2\pi(1-\nu)}\frac{y(x^2 - y^2)}{(x^2 + y^2)^2} \\
&\sigma_{xy} = \frac{\mu b}{2\pi(1-\nu)}\frac{x(x^2 - y^2)}{(x^2 + y^2)^2} \\
&\sigma_z = \nu(\sigma_x + \sigma_y) \\
&\sigma_{xz} = \sigma_{zx} = \sigma_{yz} = \sigma_{zy} = 0
\end{aligned} \tag{1.5}$$

where ν is Poisson's ratio. For a mixed straight dislocation with the angle θ between the dislocation line and the Burgers vector, based on the superposition principle, its stress

field will be the sum of the stress of a screw dislocation with Burgers vector $b = b\cos\theta$ and an edge dislocation with Burgers vector $b = b\sin\theta$.

For arbitrary dislocation configurations, a sequence of straight-line segments are usually used to approximate the real configuration and then the overall stress field can be regarded as the summation of the stress field of the each segment. Peach and Koehler [8] first derived the stress tensor of a closed dislocation loop and expressed as

$$\begin{aligned}\sigma_{\alpha\beta} = &-\frac{\mu}{8\pi}\oint_C b_m \varepsilon_{im\alpha}\frac{\partial}{\partial x_i'}\nabla'^2 R\, dx_\beta' - \frac{\mu}{8\pi}\oint_C b_m \varepsilon_{im\beta}\frac{\partial}{\partial x_i'}\nabla'^2 R\, dx_\alpha' \\ &-\frac{\mu}{4\pi(1-\nu)}\oint_C b_m \varepsilon_{imk}\left(\frac{\partial^3 R}{\partial x_i'\,\partial x_\alpha'\,\partial x_\beta'} - \delta_{\alpha\beta}\frac{\partial}{\partial x_i'}\nabla'^2 R\right) dx_k'\end{aligned} \tag{1.6}$$

Where μ and ν are shear modulus and Poisson's ratio, respectively;

b is Burgers vector of Cartesian components b_i;

ε_{ijk} is permutation operator, satisfying

$$\begin{aligned}&\varepsilon_{123} = \varepsilon_{231} = \varepsilon_{312} = 1 \\ &\varepsilon_{132} = \varepsilon_{321} = \varepsilon_{213} = -1\end{aligned} \tag{1.7}$$

δ_{ij} is Kronecker delta, satisfying

$$\delta_{ij} = \begin{cases} 0\, i \neq j \\ 1\, i = j \end{cases} \tag{1.8}$$

R is the magnitude of the radius vector connecting a source point on the loop to a field point and $\nabla'^2 R = \frac{\partial^2 R}{\partial x_i'^{\,2}}$. Thus, the stress field of an arbitrary curved dislocation can be obtained with line integration by utilizing Eq. 1.6.

In the case of anisotropic elasticity, there is no explicit expression for stress components of dislocations. However, we can resort to numerical approach to obtain the solutions of the Green's function [9], the derivative of which can be integrated over a surface bounded by a dislocation to calculate the elastic field of this dislocation. The details regarding this calculation will be discussed in Chapter 2.

1.2.2 Strain energy of a dislocation and line tension

An elastically distorted region around a dislocation produces an extra strain energy. Due to the large strain within the dislocation cores radius (around 1~2 $|b|$), the elasticity is not applicable any more within this range. Thus, the total energy can be divided into

$$E_{total} = E_{elastic\,strain} + E_{core} \tag{1.9}$$

The elastic strain energy per unit length can be expressed as [10]

$$E = \frac{\mu b^2 (1 - \nu \cos^2 \theta)}{4\pi(1-\nu)} \ln\left(\frac{R}{r_0}\right) \tag{1.10}$$

where μ is the shear modulus; b is the Burgers vector; ν is the Poisson's ratio; θ is the angle between the dislocation and the Burgers vector; R is the outer radius of integration; r_0 is the dislocation core radius. For isotropic elasticity,

$$K = \frac{\mu(1 - \nu \cos^2 \theta)}{1-\nu} \tag{1.11}$$

is defined as the energy factor of a dislocation. Then the Eq. 1.10 can be given as

$$E = \frac{Kb^2}{4\pi} \ln\left(\frac{R}{r_0}\right) \tag{1.12}$$

Accordingly, the line tension T_L per unit length of a straight dislocation depends on the energy factor K and its second derivative as [11]

$$T_L = \frac{b^2}{4\pi}\ln\left(\frac{R}{r_0}\right)\left(K(\theta)+\frac{\partial^2 K(\theta)}{\partial\theta^2}\right) \tag{1.13}$$

For anisotropic elasticity, the determination of K requires numerical approaches, and can be evaluated by using either the sextic formalism [12,13] or the integral formalism [14,15]. The details of those formalisms will be discussed in Chapter 2.

The core energy of dislocations will be evaluated by the generalized 2D Peierls-Nabarro model [16,17] in Chapter 3. Under the force from the atoms on the two sides of the glide plane, a dislocation is usually in an equilibrium position. When the dislocation is slightly displaced from its equilibrium position, an extra force is required to maintain the dislocation in this position. This force is calculated from the change in the misfit energy due to the dislocation motion. Discussion regarding this variation of the misfit energy (Peierls energy) and resulting applied shear stress (Peierls stress) will also be discussed in Chapter 3.

1.2.3 Forces on dislocations and between dislocations

As discussed before, the motion of dislocations is the result of external applied stresses and strains. The force F acting on per unit length of a dislocation can be calculated as

$$F = \tau b \tag{1.14}$$

where τ is the applied shear stress, and b is the Burgers vector. The force is always normal to a dislocation line to motivate the motion of the dislocation. In addition to the

force due to an applied stress, a dislocation has a line tension as given in Eq. 1.10, which can be defined as the energy increase with per unit increase in the length of a dislocation line. Due to the stress field of each dislocation line, forces also exist between dislocations. Based on the sign of the stress fields of dislocations and their relative positions, these interactions could be attractive or repulsive between the dislocations. For example, consider two infinite pure edge dislocations I and II with the same Burgers vector along the x-direction and the same line direction along the z-direction. Their positions are (0,0) and (x,y), respectively, where both x and y are positive. According to Eqs. 1.5 and 1.14, the two force components acting on dislocation II from dislocation I, F_x and F_y are shown as follows:

$$\begin{aligned} F_x &= \sigma_{xy} b = \frac{\mu b^2}{2\pi(1-\nu)} \frac{x(x^2-y^2)}{(x^2+y^2)^2} \\ F_y &= \sigma_x b = -\frac{\mu b^2}{2\pi(1-\nu)} \frac{y(3x^2+y^2)}{(x^2+y^2)^2} \end{aligned} \tag{1.15}$$

It can be clearly seen that, the F_x is positive when $x > y$, leading to the repulsion between two dislocations, and the F_x is negative when $x < y$, which means two dislocations will attract each other.

Moreover, the other crystalline defects such as impurities, vacancies, solute atoms, and grain boundaries also produce extra forces on dislocations, resulting in significant changes in the behavior of ordinary dislocations. In Chapter 5, the interactions of solute atoms with dislocation junctions (a configuration formed by two dislocations located on two intersecting slip planes) will be discussed in detail.

1.2.4 Movement of dislocations and interaction of dislocations

A dislocation can glide on its slip plane under an applied shear stress or even move out of this plane (climb) due to higher temperature and the effect of a normal stress. For a pure screw dislocation, its slip plane is not unique because the Burgers vector is parallel to the dislocation line. Thus screw dislocations may cross-slip in order to circumvent internal obstacles and to reduce internal stresses once the external stress reaches a certain value to overcome the line tension on the cross-slip plane, as schematically shown below.

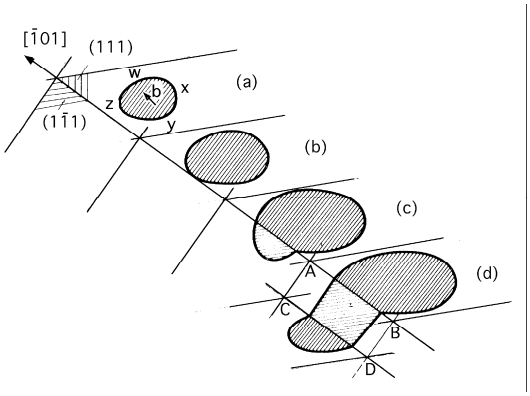

Figure 1.5 Cross-slip in a face-centred cubic crystal [6].

In addition, the intersection of two dislocations can form kinks (the steps of the dislocation lines on the slip planes), jogs (the parts of the dislocation lines that are not contained in the glide planes), or even sessile junctions (the parts formed along the intersection line of two slip planes). All these interaction mechanisms can make significant effects on the motion of dislocations and can change the macroscopic deformation behavior of crystals.

1.2.5 Multiplication of dislocations

Dislocation generation and multiplication, through Frank-Read mechanism, is one of the main sources for the increase in plastic strain during the course of deformation. Assuming an initially straight dislocation line pinned at two ends on a given glide plane, a shear stress is applied to make it bow out. At the beginning, the curvature is almost zero everywhere and the effects of the self-forces (line tension) are negligible. When the dislocation line bows out, the local curvature increases gradually to allow the self-forces balance the applied force and reach an equilibrium state at every time step. When the average curvature of the dislocation line reaches a maximum at a critical stress (the Orowan stress), which is the transition point from the stable configuration to the unstable one, the self-forces cannot balance the external applied stress. After that, the average curvature decreases although the dislocation line will expand continuously. Eventually, the segments near two ends with the same Burgers vector and the opposite line direction would get close each other and annihilate. Thus, a new dislocation loop is formed. The original dislocation line pinned at two ends continues to bow out again to generate more dislocation loops, as long as applied external stresses are maintained.

1.3 Dislocations in fcc and bcc crystals

Given the condition of crystal structure and energy, the Burgers vectors of dislocations in fcc and bcc crystals are closely related to the lattice constant, and their orientations tend to obtain the minimized energy with the existence of dislocations.

1.3.1 Unit dislocations

In fcc crystals, the closed-pack direction for atomic arrangement is <110> and the distance between atoms along this direction is $\frac{\sqrt{2}}{2}a$ (a is the lattice constant), which is the smallest atomic distance. Thus, the relative sliding of two sets of atoms leads to the relative displacement of one-atom distance, which will not significantly alter the bonds in crystals. Therefore, the Burgers vector $b = \frac{a}{2} < 110 >$, which is called unit dislocation because the magnitude of the Burgers vector equals to one atomic distance, can exist in fcc crystals due to its associated lower energy. And it can also be seen that the existence of this unit dislocation fully corresponds to the slip system {111}<110> in fcc crystals. Likewise, the Burgers vector of the unit dislocation in bcc crystals is $\frac{a}{2} < 111 >$, the magnitude of which also equals to one atomic distance along the close-packed direction.

1.3.2 Dislocation reactions, partials and sessile dislocations

In order to avoid the energy peak along the direct unit lattice vector, it was proved that the energy would be favorable if the unit dislocation can dissociate into two partials, for which the magnitude of the Burgers vector of a partial is not a unit lattice vector, and a stacking fault between the two partials. For instance, in fcc crystals, the unit dislocation with the Burgers vector $b_1 = \frac{a}{2}[10\bar{1}]$ can dissociate into two fractional dislocations with $b_2 = \frac{a}{6}[11\bar{2}]$ and $b_3 = \frac{a}{6}[2\bar{1}\,\bar{1}]$. The resulting two partials, called Shockley partials, repel each other due to the elastic interaction; in addition, there will be a band of stacking

fault between them associated with stacking fault energy to pull these two partials together. An equilibrium position will be reached once the attractive force and the repulsive force balance each other (see Chapter 3). For alloy systems exhibiting a lower stacking fault energy, the dissociation of a perfect dislocation can happen more readily.

Thompson's Tetrahedron [18] as shown in Figure 1.6 describes all the important dislocations and dislocation reactions in fcc crystals. In this tetrahedron, the four corners

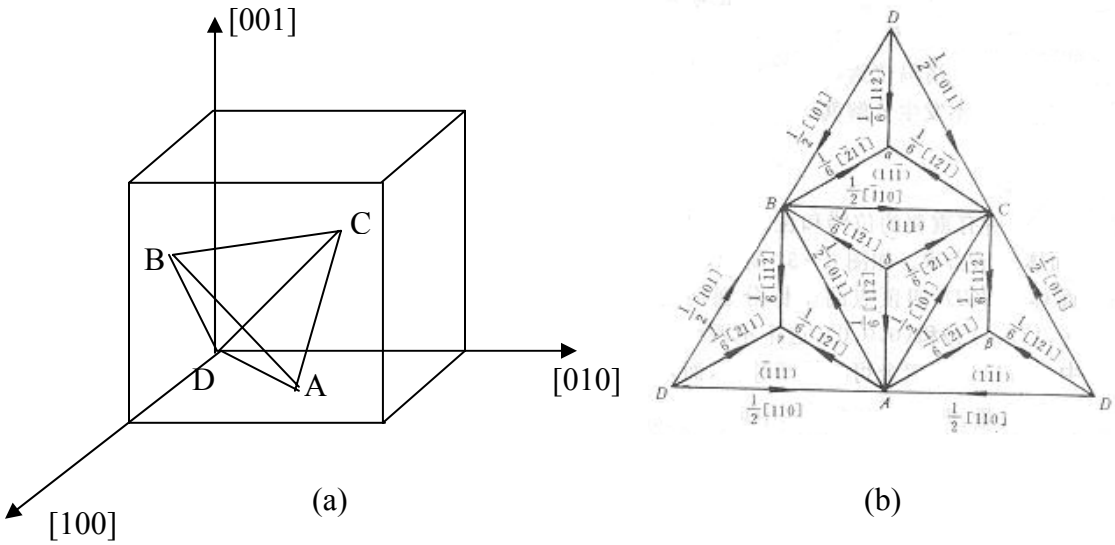

Figure 1.6 (a) Thompson's Tetrahedron; (b) unfolded Thompson's Tetrahedron [18].

are denoted by A, B, C, D and the mid-points of each faces are designated by $\alpha, \beta, \gamma, \delta$. Thus, the four faces of this tetrahedron correspond to four possible {111} planes and six edges represent $\frac{a}{2}<110>$ Burgers vectors. Similarly, the Burgers vector of Shockley partials can be expressed by the line from a corner to the center of a face where this corner is located, such as Aβ, Aγ etc. Also, the line from a corner to the center of the

opposite face can be defined as another kind of partial with the Burgers vector $\frac{a}{3}[111]$, which is called Frank partial and is a sessile partial because its Burgers vector is not in any {111} slip planes.

Moreover, the important dislocation reactions were also designated by this tetrahedron. Firstly, it can be determined that a unit dislocation can dissociate into two Shockley partials in a certain slip plane. Secondly, two unit dislocations can react to form a new unit sessile dislocation, which is called Lomer dislocation. The condition to form a Lomer dislocation is that the two unit dislocations are located at two intersected slip planes separately and both parallel to the intersection line of the slip planes. Then a Lomer reaction can be expressed as

$$\frac{a}{2}[110]+\frac{a}{2}[0\bar{1}1]\rightarrow\frac{a}{2}[101] \tag{1.16}$$

Thirdly, before the Lomer reaction, each unit dislocation could dissociate into two Shockley partials if the stacking fault energy between them is low and then the four partials can react further to form a new sessile unit dislocation, which is called Lomer-Cottrell dislocation. The detailed reactions are as follows.

$\frac{a}{2}[110]\rightarrow\frac{a}{6}[121]+\frac{a}{6}[21\bar{1}]$ in the $(1\bar{1}1)$ plane

$\frac{a}{2}[0\bar{1}1]\rightarrow\frac{a}{6}[\bar{1}\bar{1}2]+\frac{a}{6}[1\bar{2}1]$ in the (111) plane

$$\frac{a}{6}[121]+\frac{a}{6}[21\bar{1}]+\frac{a}{6}[\bar{1}\bar{1}2]+\frac{a}{6}[1\bar{2}1]\rightarrow\frac{a}{6}[121]+\frac{a}{6}[101]+\frac{a}{6}[1\bar{2}1] \tag{1.17}$$

where $\frac{a}{6}[101]$ is not in $(1\,\bar{1}\,1)$ plane or (111) plane and is a sessile dislocation.

There are more possible slip planes reported as {110}, (112}, and {123} in bcc crystals. Each of these planes contains $\frac{a}{2}<111>$ vectors. Therefore, under an applied stress, screw dislocations may cross slip on different slip planes if the variation of the energy is favorable. The possible dislocation dissociations proposed in {110} and {112} planes are

$$\frac{a}{2}[111] \rightarrow \frac{a}{6}[111] + \frac{a}{6}[111] + \frac{a}{6}[111] \text{ in } \{112\} \text{ plane}$$

$$\frac{a}{2}[111] \rightarrow \frac{a}{8}[110] + \frac{a}{4}[112] + \frac{a}{4}[111] \text{ in } \{110\} \text{ plane} \qquad (1.18)$$

In addition, it was reported that two $\frac{a}{2}<111>$ unit dislocations might interact to form a <100> unit dislocation as follows:

$$\frac{1}{2}[\bar{1}\,\bar{1}\,1] + \frac{1}{2}[111] \rightarrow [001] \qquad (1.19)$$

In Chapter 3, some results from the dissociation of <111> and <001> dislocations in B2 intermetallics by 2D generalized P-N model analysis will be discussed.

1.4 Dislocation dynamics

As discussed in the preceding sections, for special geometries of a single straight dislocation or a single circular dislocation loop (slip or prismatic), analytical solutions are available for their stress fields, interaction forces, and energies [7,19-22]. However, the difficulty in explaining the collective and dynamic behaviors of a large group of

dislocations still exists; and to achieve this objective numerical modeling and simulation techniques have been explored recently. First, two dimensional (2D) dislocation dynamics was introduced by Forman [23] to study the interaction between dislocations and undeformed obstacles, such as precipitates and inclusions. After that, a number of studies [24-29] have been carried out, focusing on straight, infinitely long dislocation distributions. Owing to the limitation of 2D geometry, these simulations could not directly give all the explanations for the characteristics of collective dislocations, including multiplication of Frank-Read sources, annihilation, dipole formation, junction formation etc. However, these studies clearly indicated the importance of such simulations to elucidate the mechanisms of plastic deformation. Currently, the efforts are made on three dimensional, 3D, dislocation dynamics [30-37]. Almost all 3D models are based on the discretization of dislocation curves into succession of dislocation segments of a finite length. The main differences among them are: how the topology of the dislocation is described (pure edge, pure screw, or mixed), the manner by which the stress or energy fields are calculated, and the introduction of the boundary conditions to the simulations.

Most research on dislocation dynamics utilizes the solutions available in the framework of classical isotropic elasticity. However, almost all the crystalline solids exhibit some degree of elastic anisotropy, ranging being moderately anisotropic such as in aluminum to highly anisotropic such as in zinc and intermetallic alloys. It is also known that the elastic anisotropy plays a significant role in the evolution of dislocation microstructures, such as formations of kinks, cross-slips, and junctions. Due to the computational

complexity, the extension from simple isotropic elasticity to anisotropic elasticity somewhat has not progressed. Therefore, it is extremely desirable to extend 3D dislocation dynamics into anisotropic elasticity in order to improve the quantitative predictive capabilities of the discrete dislocation dynamics.

1.5 Intermetallic compounds and RM B2 alloys

Intermetallic compounds are defined as solid phases containing two or more metallic elements, with optionally one or more non metallic elements, whose crystal structure is same from that of the other constituents [38]. Due to their superior mechanical and physical properties, the studies on intermetallic compounds have attracted the attention of researchers over the years. Owing to their strong internal order and bonds, intermetallics display prominent magnetic, superconducting, and chemical properties, for example, alnico being as permanent magnet, niobium-tin as type II superconductor, and nickel metal hydride battery etc. Moreover, intermetallic compounds present high strength and strong ability to resist high temperatures, such as nickel aluminide and titanium aluminide for the high temperature applications both as base and as coating materials. However, the potential of most of intermetallics for engineering applications remains to be limited because of their relatively low ductility and their unacceptable fracture toughness values at homologous temperatures [39-44]. Accordingly, some approaches have been investigated to improve the ductility of intermetallics at room temperature [45-50]. Without those contrivances, Gschneidner et al. have discovered a new class of fully ordered and ductile intermetallic compounds [51], which consist of a rare earth element and a main group or transition metal (RM). These RM intermeallics are fully

stoichiometric and have the CsCl (B2) structure. Apparently, there are 120 such alloys; most of these have not been studied, but at least 12 such compounds have been found to possess significantly high ductility and fracture toughness in polycrystalline form when tested at room temperature and in air [52-54]. Also, the bulk and defect properties of YAg and YCu have been recently studied by *ab initio* calculations [55]. The results indicate that, these have also high antiphase boundary energies as in NiAl; however, the unstable stacking fault for the <100> slip modes has lower energy in comparison to NiAl, suggesting a higher mobility of these modes. Most numerical calculation and simulation results in the following chapters will be based on three new B2 alloys YCu, YAg, and YZn. The corresponding results from normal intermetallic compounds NiAl and Fe-25Al will also be presented for comparison.

Reference

[1] Frenkel J., 1926, *Z. Fiz.*, **37**, 572.

[2] Taylor, G. I., 1934, *Proc. R. Soc.* **A145,** 362.

[3] Orowan, E., 1934, *Z. phys.* **89,** 634.

[4] Polanyi, M., ibid., 660.

[5] Burgers, J.M., 1939, *Proc. Kon. Ned. Akad. Wetenschjap.*, **42,** 293, 378.

[6] Hull, D., Introduction to dislocations, 2nd ed. (Pergamon, New York, 1975).

[7] Hirth, J. P. and Lothe J., Theory of Dislocations, 2nd ed. (McGraw-Hill, New York, 1982).

[8] Peach, M. O. and Koehler, J. S., 1950, *Phys. Rev.,* **80**, 436.

[9] Volterra, V., 1907, *Annal. Sci. Ec. Norm. Super.* **24**, 401.

[10] Forman A. J. E., 1955, *Acta Met.*, , **3**, 322.

[11] de Wit, G., and Koehler, J. S., 1959, *Phys. Rev.*, **116**, 1113.

[12] Stroh, A. N., 1958, *Phil. Mag.* **3**, 625.

[13] Eshelby, J. D., Read, W.T., and Shockley, W., 1953, *Acta Meta.* **1**, 251.

[14] Barnett, D. M. and Lothe, J., 1973, *Phys. Norv.* **7**,13.

[15] Wang, L., and Lothe, J., 1995, *Phil. Mag.* **71**, 359.

[16] Peierls, R., 1940, *Proc. Phys. Soc.* **52**, 34.

[17] Nabarro, F. R. N., 1947, *Proc. Phys. Soc.* **59**, 256.

[18] Thompson, N., 1953, *Proc. Phys. Soc.B*, **66**, 481.

[19] Nabarro, F. R. N., Theory of Cystal Dislocations (Clarendon, Oxford, 1967).

[20] Kroupa, F., *Czech. J. Phys., Sect. B*, 1960, **10**, 284.

[21] Kroupa, F., Theory of Crystal Defects, edited by B. Gruber (Academia Publishing House, Prague, 1966), pp. 275.

[22] de Wit, R., 1960, *Solid State Phys*., **10**, 269.

[23] Forman, A. J. E., 1968, *Philos. Mag*., **17**, 353.

[24] Groma, I. and Pawley, G. S., 1993, *Phil. Mag. A*, **67** (6), 1459.

[25] Gulluoglu, A. N., Srolovitz, D. J., LeSar, R., and Lomdahl, R. S., 1989, *Scripta Metall.*, **23,** 1347.

[26] Lepinoux, J. and Kubin, L. P., 1987, *Scripta Metall.*, **21,** 833.

[27] Wang, H. Y. and LeSar, R., 1995, *Phil. Mag.* A, **71,** 140.

[28] van der Giessen, E. and Needleman, A., 1995, *Mater. Sci. Eng.* **3,** 689.

[29] Ghoniem, N. M. and Amodeo, R. J., 1990, Numerical simulation of dislocation patterns during plastic deformation *Patterns, Defects and Material Instabilities* ed Walgraef, D. and Ghoniem, N. M. (Kluwer Academic) pp. 303-329.

[30] Kubin L. P., 1993, *Phys. Status Solidi* (a), **135,** 433.

[31] Kubin L. P. and Canova G., 1992, *Scripta metall.*, **27,** 957.

[32] Zbib H. M., Rhee M., and Hirth J. P., 1998, *Int. J. Mech. Science*, **40,** 113.

[33] Rhee M., Zbib H. M., and Hirth J. P., 1998, *Mod. Sim. Mat. Sci. Engr.*, **6,** 467.

[34] Ghoniem, N. M. and Sun, L.Z., 1999, *Phys. Rev. B*, **60**(1), 128.

[35] Ghoniem, N. M., Tong, S. H., and Sun, L. Z., 2000, *Phys. Rev. B*, **61**(2), 913.

[36] Ghoniem, N. M., Huang, J., and Wang Z., 2002, *Phil. Mag. Lett.*, **82**(2), 55.

[37] Huang, J. and Ghoniem, N. M., 2002, *Mod. Sim. Mat. Sci. Engr.*,**10**, 1.

[38] Schulze, G. E. R., 1967, *Metallphysik*, Berlin: Akademie-Verlag, pp. 1-76.

[39] Cahn, R. W., 2001, *Contemp. Phys.*, **42,** 365.

[40] Chen, G. L. and Liu, C. T., 2001, *Int. Mater. Rev.*, **46,** 253.

[41] Shi, X., Mahajan, S., Pollock, T. M., and Arunachalam, V. S., 1999, *Phil. Mag. A*, **79**, 1555.

[42] Liu, C. T., Stringer, J., Mundy, J. N., Horton, L. L., and Angelini, P., 1997, *Intermetallics*, **5**, 579.

[43] Yoo, M. H., Takasugi, T., Hanada, S. , and Izumi, O., 1990, *Mat. Trans. JIM*, **31**, 435.

[44] Jiao, Z., Whang, S. H., and Wang, Z., 2001, *Intermetallics*, **9**, 891.

[45] Hahn, K.H. and Vedula, K., 1989, *Scripta Metall*, **23,** 7.

[46] Liu, C. T., George, E. P., Maziaz, J. H., and Schneibel, J. H., 1998, *Mater. Sci. Eng. A*, **258**, 84.

[47] Takasugi, T., Masahashi, N., and Izumi, O., 1987, *Acta Metall.*, **35**, 381.

[48] Reed-Hill, R. E. and Abbaschian, R., *Physical Metallurgy Principles* 3rd ed. (PWS Kent, Boston, 1992), pp. 357.

[49] Liu, C. T., White, C. L. and Horton, J. A., 1985, *Acta Metall.*, **33**, 213.

[50] Sutou,Y., Omori, T., Kainuma, R., Ono,N., and Ishida, K., 2002, *Metall. Mater. Trans. A*, **33**, 2817.

[51] Gschneidner, K. Jr., Russell, A., Pecharsky, A., Morris, J.R., Zhang, Z., Lograsso T., Hsu D., Lo, C. H. C., Ye, Y., Slager A., and Kesse D., *Nature Mat.*, 2003, **2**, 587.

[52] Russell, A., Zhang, Z., Lograsso, T. A., Lo, C., Pecharsky, A., Morris, J. R., Ye, Y., Gschneidner, Jr. K., and Slager, A., 2004, *Acta Mater.*, **52**, 4033.

[53] Russell, A., Zhang, Z., Gchneidner, Jr. K., Lagrasso T., Pecharsky, A., Slager, A., and Kesse, D., 2005, *Intermetallics*, **13**, 565.

[54] Zhang, Z., Russell, A., Biner, S. B., Gschneidner, Jr. K., and Lo, C., 2005, *Intermetallics*, **13**, 559.

[55] Morris, J., Ye, Y., Lee, Y-B, Harmon, B., Gschneidner, Jr. K., and Russell, A., 2004, *Acta Mater.*, **52**, 4849.

CHAPTER 2

FORMALISM FOR 3D ANISOTROPIC ELASTICITY

2.1 Dislocation line discretization

To perform 3D dislocation dynamics calculations, dislocation loops need to be divided into several contiguous segments, which could be parametric space curves as in [1-4] (see Figure 2.1) or straight line segments as in [5,6] (see Figure 2.2). Straight-line segments to approximate the dislocation loops rather than curved segments were utilized in this thesis, because of computational advantages that will be given later. Each linear segment is terminated by a node, which connects two neighbor segments. For each segment, the Burgers vector keeps same as the one for the whole dislocation loop. The position vector $\boldsymbol{r}$ of an arbitrary point on a segment with two ends positioned at $\boldsymbol{r_1}$ and $\boldsymbol{r_2}$ can be parameterized as

$$r(u) = N_1 r_1 + N_2 r_2 \tag{2.1}$$

$N_1 = 1-u$ and $N_2 = u$ are shape functions, where $0 \le u \le 1$. Based on the desired number of integration points (Gauss quadrature points) on each segment, the Gauss-Legendre weights and abscissas for each point can be calculated from the subroutine GAULEG [7].

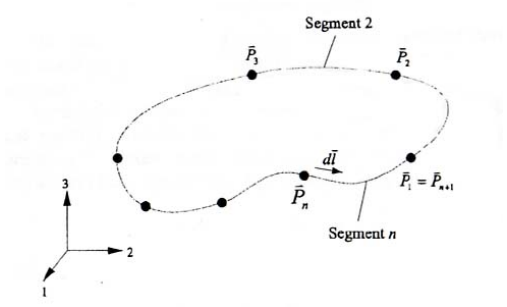

Figure 2.1 A discretized dislocation loop with finite curved segments [1].

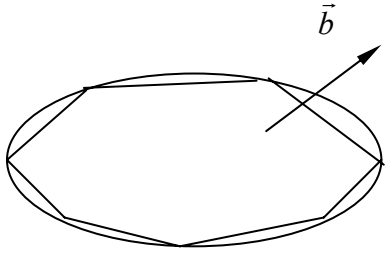

Figure 2.2 A discretized dislocation loop with finite straight segments.

2.2 Nodal force calculation

The force on each Gauss quadrature point can be obtained by Peach-Koehler formula (PK force):

$$\vec{F} = ((\sigma^D + \sigma^A) \bullet \vec{b}) \times \vec{t} + \vec{F}_{self} \tag{2.2}$$

where σ^D is the stress tensor from other remote segments; σ^A is the applied stress tensor; b is the Burgers vector of the dislocation; t is the unit tangent vector of the segment in question; and $\vec{F}_{self}$ is the force arising from the segment itself and immediate adjacent segments.

2.2.1 Stress field of dislocations and Integral Formalism

For σ^D, in the case of the full isotropic elasticity, the stress field induced by a closed dislocation loop at an arbitrary field point was given in Eq. 1.6, the integral of which can be carried out by using numerical gauss integration and summing the contribution of each segment to overall dislocation line as given below [1].

$$\sigma_{ij} = \frac{\mu}{4\pi} \sum_{\gamma=1}^{N_{loop}} \sum_{\beta=1}^{N_s} \sum_{\alpha=1}^{Q_{\max}} b_n w_\alpha \left[\frac{1}{2} R_{,mpp} (\varepsilon_{jmn} \hat{x}_{i,u} + \varepsilon_{imn} \hat{x}_{j,u}) + \frac{1}{1-\nu} \varepsilon_{kmn} (R_{,ijm} - \delta_{ij} R_{,ppm}) \hat{x}_{k,u} \right] \tag{2.3}$$

Where μ, b_i, R, ε_{ijk}, ν, and δ_{ij} represent the same meaning as in Eq. 1.6. N_{loop}, N_s, and $Q_{\max}$ represent the number of dislocation loops, the number of segments, and the number of Guass quadrature points on each segment, respectively. w_α is the weight for the Gauss point in question and $R_{,ijk}$ is the corresponding partial derivatives of radius vectors.

Within the framework of anisotropic elasticity, there is no available analytical solution for the stress tensor; however, due to the intrinsic character that the elastic field of an arbitrary dislocation can be expressed as the integral over a surface bounded by the dislocation of the derivative of a function known as the Green's function of elasticity [8], the numerical approach was employed to obtain the solutions of the Green's function.

In an infinite elastic medium, the tensor Green's function $G_{ij}(\vec{x}-\vec{x}')$ is defined as the displacement component in x_i direction at point $\vec{x}$ due to a unit force applied in the x_j direction at $\vec{x}'$. The displacement field caused by a dislocation can be given as [8]:

$$u_i(\vec{x}) = \int_s C_{jlmn} b_m G_{ij,l}(\vec{x}-\vec{x}') n_n ds(\vec{x}') \tag{2.4}$$

where *S* is the surface bounded by a dislocation line; C_{jlmn} is the fourth order elastic stiffness tensor; b_m is the components of the Burger's vector; $G_{ij,l}(\vec{x}-\vec{x}') = \partial G_{ij}(\vec{x}-\vec{x}')/\partial x_l$, and n_n are components of the unit normal vector to S. Differentiating Eq. 2.4, the elastic distortion tensor can be expressed as [9]:

$$u_{i,j}(\vec{x}) = \varepsilon_{jnk} C_{pqmn} b_m \int_L G_{ip,q}(\vec{x}-\vec{x}') \nu_k dl(\vec{x}') \tag{2.5}$$

where ε_{jnk} is the permutation tensor; ν_k is the unit tangent vector of the dislocation line; and *dl* is the dislocation line element.

To numerically obtain derivatives of the Green's functions, Stroh [10,11] developed a six-dimensional theory, in which the elastic strains are represented in terms of the products of the eigenvalues and their associated eigenvectors. However, it is not easy to

solve sextic algebraic equations, the roots of which generally need to be solved numerically. In addition, root degeneracy in isotropic case also leads to the inconvenience during the computation. To circumvent these difficulties, Barnett [12] developed the integral formalism to evaluate Green's tensor and its derivatives.

To evaluate G_{ir}, Barnett [13] considered a spherical coordinate system as schematically shown in Figure 2.3.

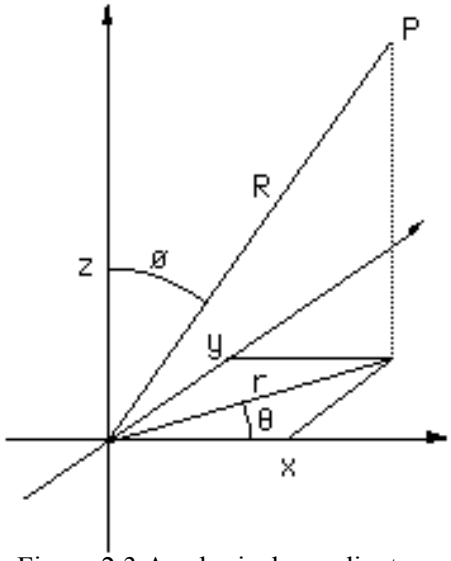

Figure 2.3 A spherical coordinate system.

$\vec{T}$ is the unit vector in the direction of $\vec{x} - \vec{x}'$, which can be expressed as:

$$T_1 = \sin\varphi\cos\theta, \quad T_2 = \sin\varphi\sin\theta, \quad T_3 = \cos\varphi \tag{2.6}$$

where $\varphi[0,\pi]$ is the angle between the x_3-axis and the vector $\vec{x} - \vec{x}'$, and $\theta[0,2\pi)$ is the angle between the positive x_1-axis and the vector $\vec{x} - \vec{x}'$ projected onto the x_1x_2-plane.

In addition, two orthogonal unit vectors, $\vec{a}$ and $\vec{b}$, in the plane perpendicular to $\vec{T}$ are defined as:

$$a_1 = \sin\theta, \quad a_2 = -\cos\theta, \quad a_3 = 0,$$
$$b_1 = \cos\varphi\cos\theta, \quad b_2 = \cos\varphi\sin\theta, \quad b_3 = -\sin\varphi \tag{2.7}$$

Thus, the arbitrary vector $\vec{z}$ in this plane is given by

$$\vec{z} = \vec{a}\cos\psi + \vec{b}\sin\psi \tag{2.8}$$

where ψ is the angle between $\vec{z}$ and $\vec{a}$.

Then the Green's function expression is given as

$$G_{ir} = \frac{1}{4\pi^2\left|\vec{x}-\vec{x}'\right|}\int_0^{\pi} M_{ir}^*(\vec{z}(\psi))d\psi \tag{2.9}$$

where $M_{ir}^*(\vec{z}) = \dfrac{N_{ir}(\vec{z})}{D(\vec{z})}$ is the inverse matrix of symmetric Christoffel stiffness matrix $M_{ir}(\vec{z}) = C_{ijrs}z_j z_s$ [14]. $N_{ir}(\vec{z}) = \dfrac{1}{2}\varepsilon_{ikl}\varepsilon_{rmn}M_{km}M_{\ln}$ is a cofactor of the matrix $M_{ir}^*(\vec{z})$ and $D(\vec{z}) = \varepsilon_{mnl}M_{m1}M_{n2}M_{l3}$ is the determinant of it.

For derivatives of G_{ir}, Barnett [13] also showed it's simple integral expression as

$$G_{ir,s}(\vec{x}-\vec{x}') = \frac{1}{4\pi^2\left|\vec{x}-\vec{x}'\right|^2}\int_0^{\pi}\left\{-T_s M_{ir}^* + z_s F_{ir}\right\}d\psi \tag{2.10}$$

where $F_{ir} = C_{jpnw}M_{ij}^*M_{nr}^*(z_p T_w + z_w T_p)$.

Combining Eqs. 2.5 and 2.10, the strain tensor at field points can be calculated numerically.

During the course of simulations, to reduce the heavy computational burden for the evaluation of multiple integrals associated with the Eq. 2.10 to a manageable level, 18 preprocessed look-up tables (overall Einstein summation for *i, j* and *k*) with 5° angle

separation were formed, for which φ and θ vary within the ranges mentioned above. For given angles φ and θ in real dislocation configurations, interpolation scheme (subroutine LOCATE and BILINEAR) [7] was employed to get the value of the derivative of the Green's function. The error involved in this approach is around 2%.

2.2.2 Calculation of self-force and Sextic formalism

To evaluate this self-force term, several approaches are available. Brown [15] considered to add an additional small loop around the segment, that is, calculate the stress on the points, which have normal distance $\pm\varepsilon$ to the point in question, respectively, and then take the average value. Zbib et al. [16] introduced superposition procedure by considering the force at certain distance from bend resulting from the semi-infinite segment (starting from the bend) first and then subtracting the force from the semi-infinite segment (starting from the other end of the finite segment) via far-field equations as given earlier. Anton et al. [17] also calculated the self-force by fitting a circle on three adjacent nodes and then using the stress field arising from two fitted arcs (subtracting cut-off distance), the analytical expression of which is available. Barnett [18] showed the in-plane self-force at the point P on the loop can be written as:

$$F^S = \kappa E(\alpha) - \vec{b} \cdot \tilde{\sigma}^S \cdot \vec{n} \tag{2.11}$$

where κ is the in-plane curvature at point P; $E(\alpha)$ is the elastic energy of per unit length of a straight dislocation line; $\tilde{\sigma}^S = \frac{1}{2}[\sigma^S(P+\varepsilon m) + \sigma^S(P-\varepsilon m)]$ is the average self-stress at P, approaching it from an infinitesimal distance along the in-plane vector $P \pm \varepsilon m$; and

$\vec{n}$ is the in-plane unit normal vector to the tangent vector at point P. Gavazza and Barnett [19] derived a more explicit expression from Eq. 2.11, that is;

$$F^S = \kappa\{E(\alpha) - [E(\alpha) + E''(\alpha)]\ln(\frac{8}{\varepsilon\kappa}) - [F(\alpha) + F''(\alpha)]\} - J[L, P] \tag{2.12}$$

where the first term results from the loop stretching during the infinitesimal motion; the second and third terms are major contributions for self-force, which are usual line tension approximation. The fourth and fifth terms are dislocation core contributions, and $J[L, P]$ is a non-local contribution from other parts of the loop. It was shown [2] that the total contributions from the dislocation line stretching, the dislocation core, and the non-local terms are less than 18%. The sextic formalism given by Stroh [10] was adopted to determine the values of E and its second derivative.

Here, a short summary for sextic formalism is given as follows. The basic equation of linear relation between the stresses σ_{ij} and the strains e_{ij} can be written in terms of the fourth rank tensor C_{ijkl}:

$$\sigma_{ij} = C_{ijkl} e_{kl} \tag{2.13}$$

where i, j, k and l all take values from 1 to 3 and Einstein summation over repeated subscripts is carried out. Strains e_{kl} can be expressed as:

$$e_{kl} = \frac{1}{2}(\frac{\partial u_k}{\partial x_l} + \frac{\partial u_l}{\partial u_k}) \tag{2.14}$$

Substituting Eq. 2.14 into Eq. 2.13, the stresses can be written in terms of the displacements:

$$\sigma_{ij} = c_{ijkl}(\frac{\partial u_k}{\partial x_l}) \tag{2.15}$$

In the case of no body forces, substituting Eq. 2.15 into static equilibrium equation, we can get:

$$C_{ijkl}(\frac{\partial u_k}{\partial x_j \partial x_l}) = 0 \tag{2.16}$$

In the study of Eshelby et al. [20], the axis x_3 was taken to be parallel to the dislocation line, which means that the elastic state is independent of x_3. Thus, the standard form of solutions for Eq. 2.16 can be shown as:

$$u_k = A_k f\left(x_1 + px_2\right) \tag{2.17}$$

where p and A_k are constants. Substitution Eq. 2.17 into Eq. 2.16, we have:

$$(C_{i1k1} + C_{i1k2}p + C_{i2k1}p + C_{i2k2}p^2)A_k = 0 \tag{2.18}$$

The linear Eqs. 2.18 have a nonzero solution for the A_k only if p is such that the determinant of their coefficient is zero, i.e.

$$\left|C_{i1k1} + C_{i1k2}p + C_{i2k1}p + C_{i2k2}p^2\right| = 0 \tag{2.19}$$

It was shown that the roots p_n are never real. Since the elastic constants are real, the roots must be pairs of complex conjugates, i.e.

$$p_4 = p_1^* \quad p_5 = p_2^* \quad p_6 = p_3^* \tag{2.20}$$

Only three roots $p_\alpha(\alpha = 1,2,3)$ with positive imaginary parts are used in Stroh's theory. Numerical methods are needed to obtain these three roots. Once $p_\alpha(\alpha = 1,2,3)$ are

found, the corresponding non-zero vector A_k can also be found to satisfy Eq. 2.18. Stroh then defines:

$$L_{i\alpha} = (C_{i2k1} + p_\alpha C_{i2k2}) A_{k\alpha} \tag{2.21}$$

and $M_{\alpha j}$, which is the inverse of $L_{i\alpha}$; and

$$B_{ij} = \frac{1}{2} i \sum_{\alpha} (A_{i\alpha} M_{\alpha j} - \bar{A}_{i\alpha} \bar{M}_{\alpha j}) \tag{2.22}$$

H_{ij} is defined as the inverse of B_{ij}. Here the matrices *A, L, M, B,* and *H* are same for any dislocation with some geometry and not related with the Burgers vector. In Stroh's theory, the relation between the Burgers vector and the matrix B is given as:

$$\begin{aligned} b_i &= B_{ij} d_j \\ d_i &= H_{ij} b_j \end{aligned} \tag{2.23}$$

Then the elastic energy, *E*, can be calculated by

$$E = \frac{C_{44}}{4\pi} H_{ij} b_i b_j \ln\left(\frac{R}{r_0}\right) \tag{2.24}$$

Preprocessed tables for E and E'' with the angle variation from *0* to π were also set up to lower the computational burden greatly. Likewise, for given angles between Burgers vectors and dislocation lines, again, the interpolation approach can be used (subroutine SPLINE and SPLINT [7]) to calculate the values of line tension and the resulting self-forces at the Gauss integration points.

Once the stress tensor σ^D and the self-force were calculated, the force on the Gauss point in question can be obtained by utilizing Eq. 2.2. Then the forces on the two ends of this segment can be calculated by the integration along this segment and the global force

vector for the whole dislocation line can be assembled with the force vector of each dislocation node.

2.3 Equation of Mobility

According to the calculated forces on nodes, the governing equation of motion of a single dislocation loop is given by [2]:

$$\int_{\Gamma}(F_k^t - B_{\alpha k}V_\alpha)\delta_{rk}\left|ds\right| = 0 \tag{2.25}$$

Here, F_k^t are the components of the resultant force, consisting of the PK force (Eq. 2.2); $B_{\alpha k}$ is the resistivity (inverse mobility) matrix; V_α are velocity vector components; δ_{rk} are distance vector components, and the line integral is carried along the arc length of the dislocation *ds*. Once the velocities of the nodal points on dislocation lines are determined from Eq. 2.25, the positions of dislocations are updated, and then dislocation reactions are carried out.

For clarity, the flow charts of 3D dislocation dynamics employed in the simulations are shown in Figures 2.4 and 2.5 for isotropic and anisotropic cases, respectively.

Isotropic Elasticity:

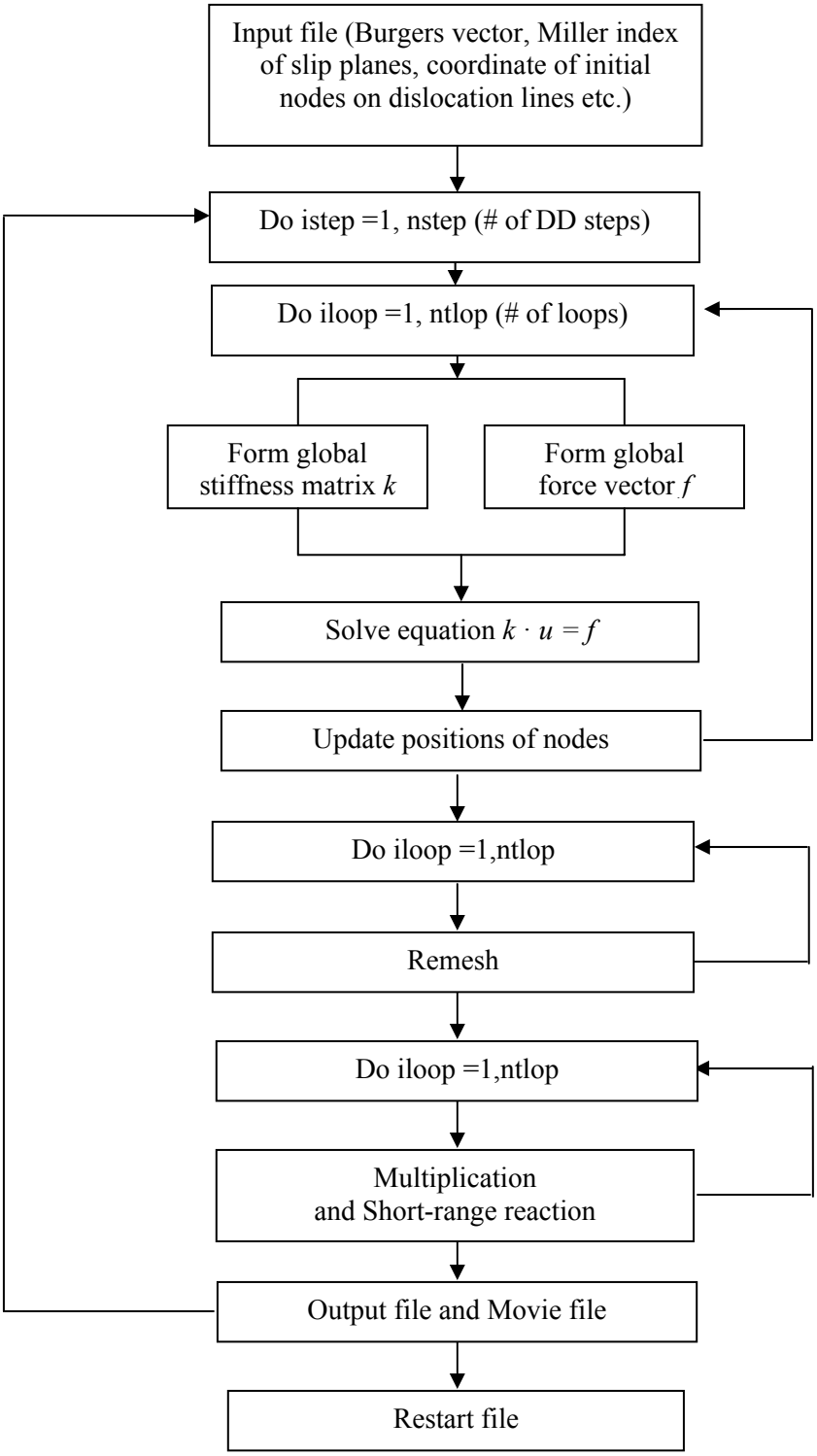

Figure 2.4 Flow chart of isotropic dislocation dynamics simulations.

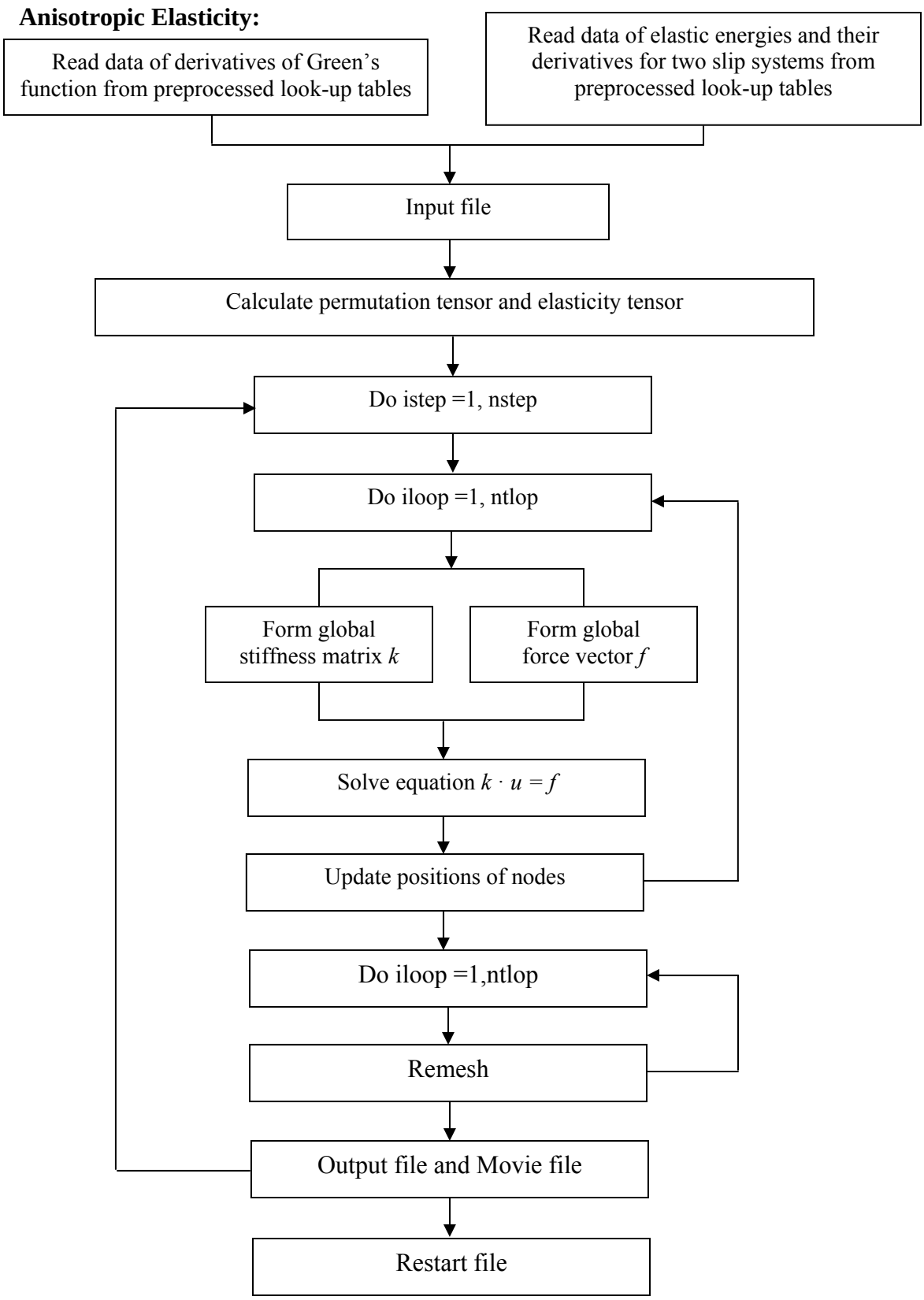

Figure 2.5 Flow chart of anisotropic dislocation dynamics simulations.

Reference

[1] Ghoniem, N. M. and Sun L. Z., 1999, *Phys. Rev. B*, **60**(1), 128.

[2] Ghoniem, N. M., Tong, S. H., and Sun, L. Z., 2000, *Phys. Rev. B*, **61**(2), 913.

[3] Ghoniem, N. M., Huang, J., and Wang Z., 2002, *Phil. Mag. Lett.*, **82**(2), 55.

[4] Huang, J. and Ghoniem, N. M., 2002, *Mod. Sim. Mat. Sci. Engr.*,**10**, 1.

[5] Zbib, H. M., Rhee, M., and Hirth, J. P., 1998, *Int. J. Mech. Science*, **40,** 113.

[6] Rhee, M., Zbib, H. M., and Hirth, J. P., 1998, *Mod. Sim. Mat. Sci. Engr.*, **6,** 467.

[7] Press, W. H. et al., *Numerical Recipes in FORTRAN: The Art of Scientific Computing*, 2nd Edition, (Cambridge University Press, 1992).

[8] Volterra, V., 1907, *Annal. Sci. Ec. Norm. Super.*, **24**, 401.

[9] Mura, T., 1963, *Phil. Mag.*, **3**, 625.

[10] Stroh, A. N., 1958, *Phil. Mag.*, **3,** 625.

[11] Stroh, A. N., 1962, *J. Math. Phys.*, **41,** 77.

[12] Barnett, D. M. and Lothe, J., 1973, *Phys. Norv.*, **7**, 13.

[13] Barnett, D. M., 1972, *Phys. Stat. Sol. (b)*, **49**, 741.

[14] Hearmon, R., *Applied Anisotropic Elasticity*, (Oxford University Press, Oxford, 1961).

[15] Brown, L. M., 1964, *Phil. Mag.*, **10**, 441.

[16] Zbib, H. M., Rhee, M., and Hirth, J. P., 1998, *Int. J. Mech. Science*, **40,** 113.

[17] Faradjian, A. K., Friedman, L. H., and Chrzan, D. C., 1999, *Mod. Sim. Mat. Sci. Engr.*, **7**, 479.

[18] Barnett, D. M., 1976, *Phys. Stat. Sol. (a)*, **38**, 637.

[19] Gavazza, S. D. and Barnett, D. M., 1976, *J. Mech. Phys. Solids.*, **24**, 171.

[20] Eshelby, J. D., Read, W. T., and Shockley, W., 1953, *Acta Mat.,* **1**, 251.

CHAPTER 3

INTRINSIC PROPERTIES OF PERFECT DISLOCATIONS IN INTERMETALLICS

3.1 Stability of perfect dislocations in intermetallics

Stability of the dislocations in intermetallics plays an important role in deformation mechanisms for yielding and work hardening [1-3]. In order to better understand the deformation behavior in these new rare-earth based intermetallics and also provide guidance to experimental efforts, the stability of the ordinary dislocations in YCu, YAg, and YZn was studied and the results were compared with the common intermetallic alloys NiAl and Fe-25Al.

In this study the sextic formalism given by Stroh [4], the detail of which has been discussed in Chapter 2, together with the right-handed Cartesian coordinate system shown in Figure 3.1(a), were adopted to determine the values of energy factor K (see Eq. 2.24).

If the logarithmic term in Eq. 1.12 is assumed to be constant for all dislocation orientations, the $1/K$ plots are equivalent to the inverse Wulff plots ($1/E$) [5]. There are two criteria for dislocation line instability [6] as schematically shown in Figure 3.1(b). The first is the concavity of the inverse Wulff plot which can be defined by two common tangent points (θ_A - θ_B). And the second is the negative line tension ($T_L < 0$) that

corresponds to the two inflection points (θ_P - θ_Q). The negative line tension is a sufficient but not necessary condition for instability. All straight dislocations with the interval θ_A - θ_B will relax their energy by transforming into V-shaped bends or zigzagged bends [7].

The elastic constants of the alloys at room temperature used in this study are given in Table 3.1, together with the anisotropy factors $A=2C_{44}/(C_{11}-C_{12})$ and $H=2C_{44}-C_{11}+C_{12}$ for the purpose of comparison. A detailed discussion of the role of anisotropy constants in these intermetallics in terms of Pugh's ductility criterion was recently given in ref. [8].

Table 3.1 Elastic constants and anisotropy factors of five intermetallic alloys.

	C_{11} (10^2GPa)	C_{12} (10^2GPa)	C_{44} (10^2GPa)	A	H
Fe-25Al	1.71	1.31	1.32	6.6	2.24
NiAl	1.703	1.154	0.897	3.27	1.245
YAg	1.024	0.54	0.372	1.54	0.26
YCu	1.134	0.484	0.323	0.99	-0.004
YZn	0.9465	0.4777	0.4716	2.01	0.47

Elastic constants were taken for Fe-25Al and NiAl from [2] and [1], respectively. Experimental values given in [8] were used for YAg and YCu. Values for YZn were measured and they closely agree with [9].

3.1.1 Line stability of glide dislocations (shear loops)

Figure 3.2 compares the inverse energy ($1/K$) plots for $(1\bar{1}0)[111]$ slip. As can be seen from Figure 3.2(a), for NiAl, the dislocations within the angular range of $38^\circ < \theta < 59^\circ$ (θ_A - θ_B) are unstable, and also the dislocations in the range of $41^\circ < \theta < 52^\circ$ (θ_P - θ_Q) have negative line tension values. Similarly, the instability in the range of $24^\circ < \theta < 76^\circ$ and negative line tension between $37^\circ < \theta < 60^\circ$ for Fe-25Al are observed. In contrast, the dislocations with this slip system are all stable in YCu, YAg, and YZn as can be seen

from the convex shape of (1/*K*) plots in Figure 3.2(b); in addition, for all the θ values their line tension is positive.

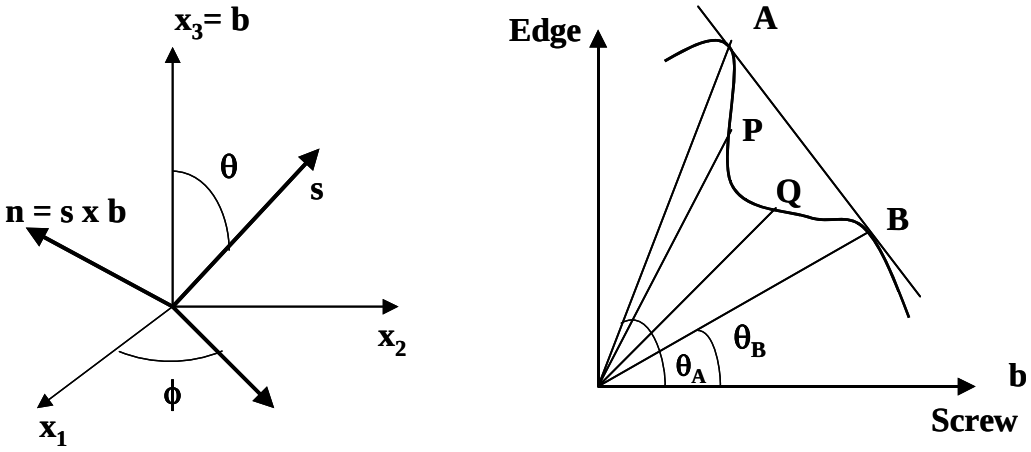

(a) (b)

Figure 3.1 (a) Cartesian coordinate system for a straight dislocation; **b** is the Burgers vector and **s** is the dislocation line vector; (b) A schematic illustration of dislocation instabilities on an inverse Wulff plot; θ is the angle between the Burgers vector and the dislocation line direction; the points labeled P and Q indicate the range where the line tension takes negative values.

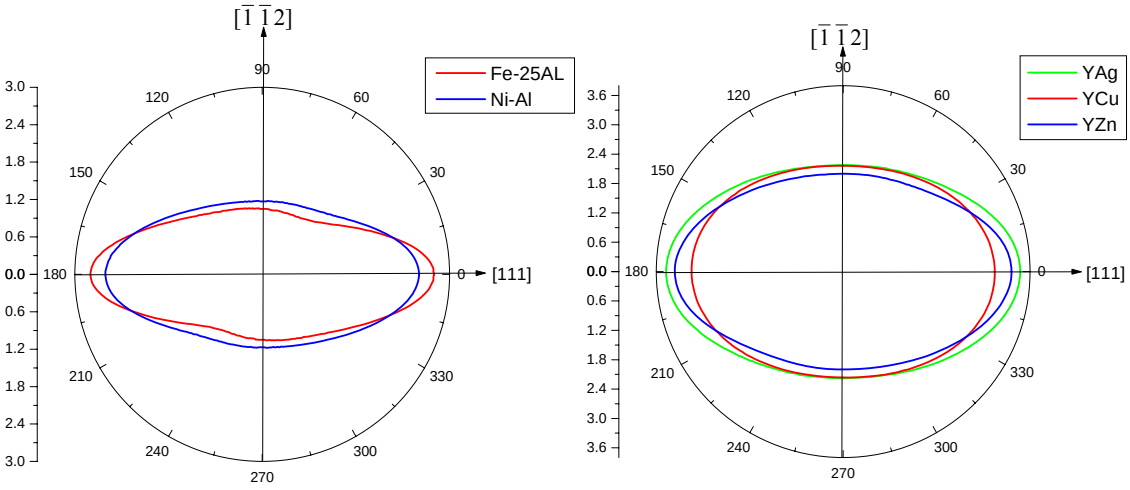

(a) (b)

Figure 3.2 (1/K) plot for $(1\,\bar{1}\,0)[111]$ glide loop. (a) Data for NiAl and Fe-25Al; instabilities for NiAl are: 38°<$\theta_{A\text{-}B}$ <59° and 41°<$\theta_{P\text{-}Q}$ <52°; and for Fe-25Al are: 24°<$\theta_{A\text{-}B}$ <76° and 37°<$\theta_{P\text{-}Q}$ <60°; (b) Data for YCu, YAg, and YZn.

For the case of $(1\bar{1}0)[001]$ slip, Fe-25Al exhibits two ranges of instability, one centering on screw ($\theta = 0^{\circ}$) and the other centering on edge dislocations ($\theta = 90^{\circ}$). As for NiAl, the instability is only centered on the screw dislocations; no instability is present near the edge dislocations as can be seen in Figure 3.3(a). The angles for these instabilities are listed in the Figure caption. However, $(1\bar{1}0)[001]$ slip in YCu, YAg, and YZn is stable in all directions together with all positive line tension as seen in Figure 3.3(b).

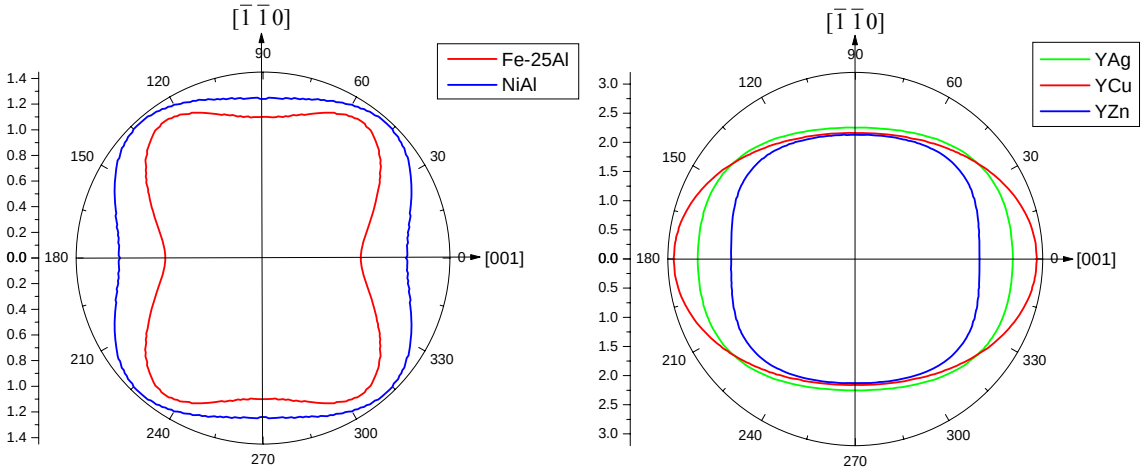

(a) (b)

Figure 3.3 (1/K) plot for $(1\bar{1}0)[001]$ glide loop. (a) Data for NiAl and Fe-25Al; instabilities for NiAl are: $-17^{\circ}<\theta_{A\text{-}B}<17^{\circ}$ and $-12^{\circ}<\theta_{P\text{-}Q}<12^{\circ}$; and for Fe-25Al are: $-36^{\circ}<\theta_{A\text{-}B}<36^{\circ}$, $66^{\circ}<\theta_{P\text{-}Q}<114^{\circ}$ and $-15^{\circ}<\theta_{A\text{-}B}<15^{\circ}$, $77^{\circ}<\theta_{P\text{-}Q}<103^{\circ}$; (b) Data for YCu, YAg, and YZn.

The *(1/K)* plots for $(1\bar{1}0)[110]$ slip are shown in Figure 3.4. As can be seen from the Figure, this slip system appears to be stable in both conventional intermetallics NiAl and Fe-25Al and the rare-earth based YCu, YAg, and YZn.

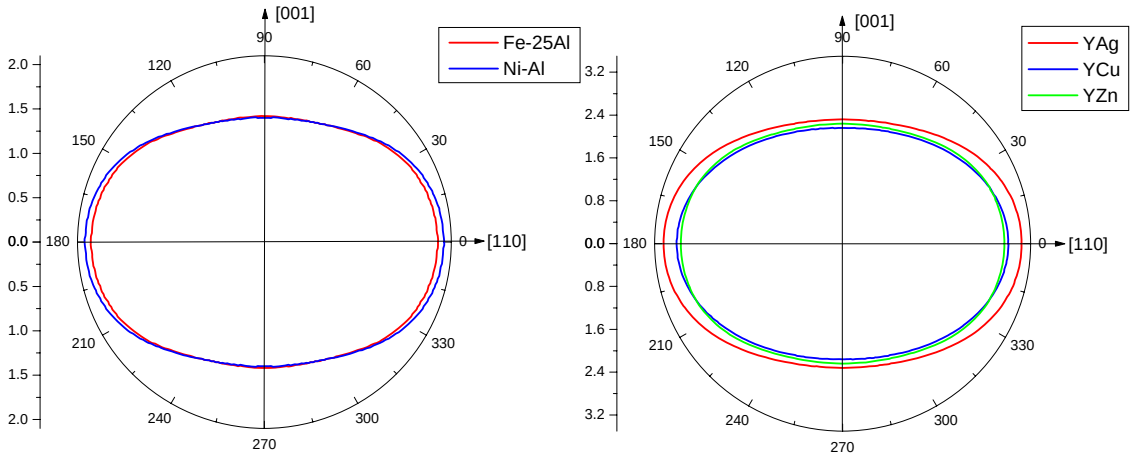

Figure 3.4 (1/K) plot for $(1\bar{1}0)[110]$ glide loop. (a) Data for NiAl and Fe-25Al; (b) Data for YCu, YAg, and YZn.

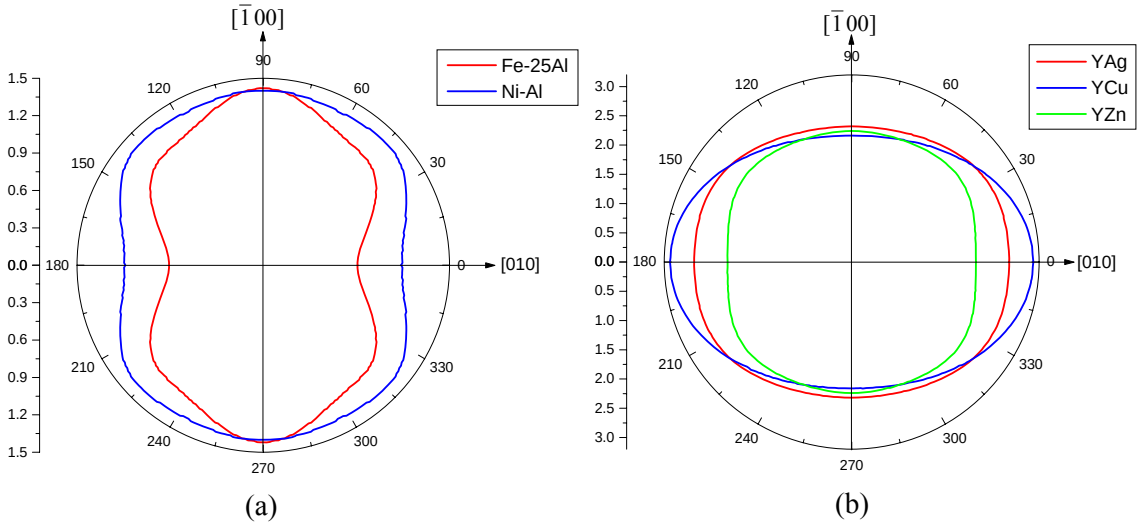

Figure 3.5 (1/K) plot for (001)[010] glide loop. (a) Data for NiAl and Fe-25Al; instabilities for NiAl are: $-30^\circ<\theta_{A\text{-}B}<30^\circ$ and $-13^\circ<\theta_{P\text{-}Q}<13^\circ$; and for Fe-25Al are: $-34^\circ<\theta_{A\text{-}B}<34^\circ$, $-16^\circ<\theta_{P\text{-}Q}<16^\circ$, and $52^\circ<\theta_{A\text{-}B}<68^\circ$, $56^\circ<\theta_{P\text{-}Q}<63^\circ$; (b) Data for YCu, YAg, and YZn.

In the case of (001)[010] slip, as seen in Figure 3.5(a), while Fe-25Al exhibits instability in two angular ranges, one in screw orientation ($\theta = 0^\circ$) and the other in mixed orientation ($\theta \approx 60^\circ$), for NiAl the instability range is only in screw orientation. Again for this slip

system, either concavity in the (1/*K*) plot, or negative values for the line tension in YCu, YAg, and YZn is not observed, as can be seen in Figure 3.5(b).

For all these slip systems, the energy factors for edge component K_e and screw component K_s together with their ratios (K_e / K_s) indicating the stability are summarized in Table 3.2. For $(K_e / K_s) > 1$, pure screw dislocations are more energetically favorable than pure edge dislocations. In the case of $(1\bar{1}0)[001]$ and (001)[010] slip systems the edge dislocations are more stable for Fe-25Al and NiAl. For these slip systems, in YZn the edge and the screw dislocations are almost equally stable. On the other hand, in YAg and YCu the energetically favorable dislocations appear to be of screw character in all the slip systems.

Table 3.2 Energy factor and stability ratio of the glide dislocations on the four different slip systems (unit: 10^2 GPa).

	$(1\bar{1}0)[111]$			$(1\bar{1}0)[001]$			$(1\bar{1}0)[110]$			(001)[010]		
	Ke	Ks	Ke/Ks	Ke	Ks	Ke/Ks	Ke	Ks	Ke/Ks	Ke	Ks	Ke/Ks
Fe-25Al	0.95	0.36	2.64	0.91	1.32	0.67	0.71	0.51	1.39	0.70	1.32	0.53
NiAl	0.85	0.40	2.13	0.80	0.89	0.90	0.71	0.50	1.42	0.71	0.90	0.79
YAg	0.46	0.28	1.64	0.44	0.37	1.19	0.43	0.30	1.43	0.43	0.37	1.16
YCu	0.46	0.32	1.44	0.46	0.32	1.44	0.46	0.32	1.44	0.46	0.32	1.44
YZn	0.50	0.29	1.72	0.47	0.47	1.00	0.45	0.33	1.36	0.45	0.47	0.96

The stability of dislocations in NiAl and iron aluminates was studied previously in [1] and [2], respectively. The results for these alloys with regard to line instabilities, Figures 3.2-3.5, are exactly the same for most of the slip systems as given in [1,2], and any deviations seen are only within one degree. These stability analyses of dislocation systems in NiAl and iron aluminates have been correlated well with many detailed microstructural analyses [2,10-14] and molecular dynamics simulations [15-17]. At this

stage, such detailed correlation for YCu, YAg, and YZn cannot be made, due to the extremely limited availability of TEM data. Nevertheless, it is expected that the results presented for these new rare-earth based intermetallics are equally as valid as in the case of NiAl and Fe-25Al and that they elucidate the differences in single crystalline deformation behavior.

As seen from the (1/*K*) plots, the slip systems in the rare-earth based intermetallic compounds YCu, YAg, and YZn are all stable, in contrast to NiAl and Fe-25Al. For both screw and edge dislocations the energy factor values for these systems are about half of the values seen for Fe-25Al and NiAl. The results also indicate that for YAg and YCu the energetically favorable dislocations appear to be of screw character in all the slip systems; however, for YZn, both the edge and the screw dislocations are approximately equally stable in $\langle 001 \rangle$ orientation.

3.1.2 Line tension and kink pair interaction energy

The elastic interaction energy of kink pairs, *W*, is given by:

$$W = \frac{b^2}{8\pi}\left(K(\theta) + \frac{\partial^2 K(\theta)}{\partial \theta^2} \right)\frac{h^2}{L} \tag{3.1}$$

where *h* is the height of the kink and *L* is the length of the kink. As can be seen from Eqs. 1.10 and 3.1, for the same dislocation orientation, the line tension and kink pair interaction energy have the same energy factor *K* terms. Therefore, their angular plots will have the same shape but different units. The additional stress needed to move the

dislocations with a kink/bowing part increases with increasing line tension; therefore, glide becomes more difficult for dislocations having larger line tension.

Because there is no negative line tension for $(1\bar{1}0)[110]$ slip system in any of the alloys investigated, the angular variation of the line tension factor values is shown in Figure 3.6 for this slip system. The inserts indicate the kink pairs or bowing parts on the dislocations. As can be seen from the Figure, with the exception of YCu, the angular values for the minimum/maximum values of line tension factor are very similar in all alloys for this slip system. The line tension factor values of screw and edge dislocations, the minimum/maximum values together with the angular values and corresponding approximate directions, for all the slip systems under consideration, are summarized in Table 3.3. In general, it is observed that the angles θ_{min} and θ_{max} where the line tension has minimum or maximum values do not correspond to screw or edge orientations. Moreover, the ratio $(K+K'')_{min} / (K+K'')_{max}$ is less than $(K+K'')_{edge} / (K+K'')_{screw}$. With the exception of YZn under $(1\bar{1}0)[001]$ and $(001)[010]$ slip condition, the line tension factor values for screw segments are higher than the values seen for edge segments indicating higher attractive interactions between the screw segments. Also, $(K+K'')_{edge} / (K+K'')_{screw} < 1$ indicates that the edge dislocations with kinks/bowing parts are much easier to glide than screw dislocations in their respective slip planes. Therefore, glide is easier for edge dislocations with kinks in YCu, YAg, Fe-25Al, and NiAl in all the slip systems, and in YZn except for the $(1\bar{1}0)[001]$ and $(001)[010]$ slip systems in which glide is easier for the screw dislocations. For YCu, the line tension

factor values for both screw and edge segments are almost independent of the slip system, while for the others they vary from slip system to slip system. For both edge and screw segments, the line tension factor values in Fe-25Al and NiAl are about a factor of 2-4 more than the ones seen for the rare-earth based intermetallic compounds.

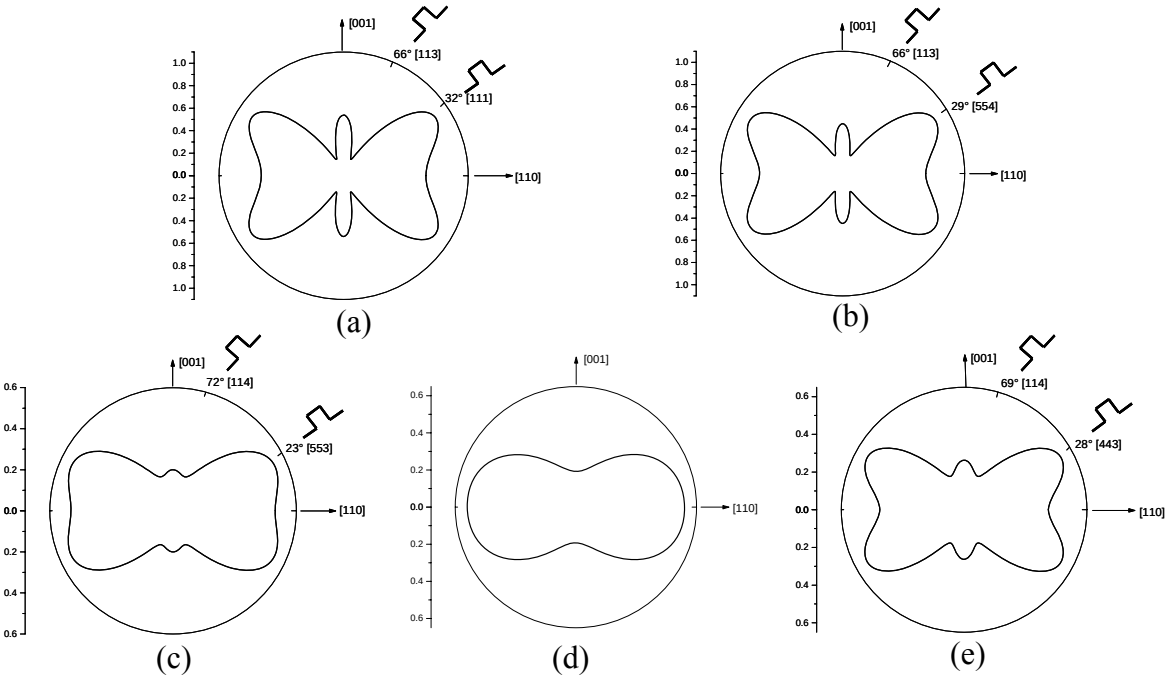

Figure 3.6 Angular variation of the line tension factor of $(1\bar{1}0)[110]$ slip dislocations; the inserts indicate the kink pairs or bowing parts on certain orientated dislocations. Data for (a) Fe-25Al, (b) NiAl, (c)YAg, (d) YCu, and (e) YZn.

Table 3.3 Line tension factor $(K + K'')$ of the glide dislocations under the different slip systems (unit: 10^2 GPa).

	$Ke + Ke''$	$Ks + Ks''$	$(K+K'')_{\min}$		$(K+K'')_{\max}$		$\frac{Ke+Ke''}{Ks+Ks''}$	$\frac{(K+K'')_{\min}}{(K+K'')_{\max}}$
			$\theta_{\min}$	[uvw]	$\theta_{\max}$	[uvw]		
$(1\bar{1}0)[111]$ Slip								
Fe25Al	0.5352	2.818					0.19	
NiAl	0.3346	2.037					0.16	
YAg	0.2025	0.7401	0.1861		0.7401		0.27	0.25
			66°	$[\bar{1}\bar{1}7]$	0°	[111]		
YCu	0.1855	0.5984	0.1855		0.5984		0.31	0.31
			90°	$[\bar{1}\bar{1}2]$	0°	[111]		
YZn	0.2799	0.8917	0.1529		0.8917		0.31	0.17
			57°	$[\bar{2}\bar{2}7]$	0°	[111]		

Table 3.3 (continued)

			$(1\bar{1}0)[001]$ Slip			
Fe25Al	*	*				
NiAl	*	*				
YAg	0.1676	0.2846	0.1676 90° $[\bar{1}\bar{1}0]$	0.6125 36° $[\bar{1}\bar{1}2]$	0.59	0.27
YCu	0.1850	0.6052	0.1850 90° $[\bar{1}\bar{1}0]$	0.6052 0° [001]	0.31	0.31
YZn	0.2074	0.0428	0.0428 0° [001]	0.7969 40° $[\bar{2}\bar{2}3]$	4.84	0.05
			$(1\bar{1}0)[110]$ Slip			
Fe25Al	0.5402	0.7273	0.1582 66° [113]	0.9613 32° [111]	0.74	0.16
NiAl	0.4481	0.7489	0.1752 66° [113]	0.9628 29° [554]	0.60	0.18
YAg	0.2	0.4969	0.1749 72° [114]	0.5412 23° [553]	0.40	0.32
YCu	0.1926	0.5852	0.1926 90° [001]	0.5852 0° [110]	0.33	0.33
YZn	0.2628	0.4464	0.1914 69° [114]	0.5826 28° [443]	0.59	0.33
			(001)[010] Slip			
Fe25Al	0.2177	*				
NiAl	0.9668	*				
YAg	0.2768	0.2829	0.2415 72° $[\bar{3}10]$	0.6045 34° $[\bar{2}30]$	0.98	0.40
YCu	0.1831	0.6042	0.1831 90° $[\bar{1}00]$	0.6042 0° [010]	0.30	0.30
YZn	0.4398	0.0281	0.0281 0° [010]	0.7808 36° $[\bar{5}70]$	15.6	0.035

* negative line tension

3.1.3 Line tension of screw dislocations on cross-slip planes

The line tension of screw dislocations is important primarily because of its role in deformation involving cross-slip. If the line tension on a cross-slip plane is many times larger than the line tension on a primary-slip plane, because the bowing of a dislocation on the cross-slip plane is more difficult, higher line tension counterbalances the external

forces that drive the cross-slip from the primary-slip plane to the cross-slip plane. On the other hand, if the line tension is negative on one or more cross-slip planes, since they are elastically unstable, cross-slip may occur by lengthening/bending (i.e. zigzag formation) even in the absence of any external driving force [18].

It was shown that the line tension values for <111> and <001> screw dislocations are independent of the cross-slip planes [18]. The results obtained here also support this and did not indicate any substantial difference in the line tension of [111] and [001] screw dislocations for the cross-slip planes in YCu, YAg, and YZn by taking $(1\bar{1}0)$ plane as the reference primary-slip plane. However, cross-slip for these screw dislocations will depend on the line tension factor values given in Table 3.3. For [111] screw dislocations it is much easier to cross-slip in YCu, followed by YAg and then YZn, than in NiAl and Fe-25Al. On the other hand, for $(1\bar{1}0)[001]$ and $(001)[010]$ screw dislocations, while the NiAl and Fe-25Al show negative line tensions, the values for YCu, YAg, and YZn are all positive, Figures 3.3 and 3.5. Therefore, cross-slip of <001> screw dislocations is more favorable in NiAl and Fe-25Al than in the new rare-earth based intermetallic compounds. For <001> screw dislocations cross-slip becomes much easier in YZn, than in YAg and lastly in YCu, Table 3.3.

For $(1\bar{1}0)[110]$ dislocations there is no line tension instability, Figure 3.4. Taking $(1\bar{1}0)$ plane as the reference primary-slip plane, variation of the line tension factor values on its cross-slip planes for this screw dislocation is shown in Figure 3.7. As can be seen

from the Figure, the variations of the line tension factor values at different cross-slip planes are much smaller for rare-earth based alloys, which makes this cross-slip possible at much smaller external driving forces than the ones required for Fe-25Al and NiAl. In the case of YCu, there is no difference in the line tension values for the different cross-slip planes due to its almost isotropic nature, Table 3.1, and again YAg exhibits a smaller variation in comparison to YZn.

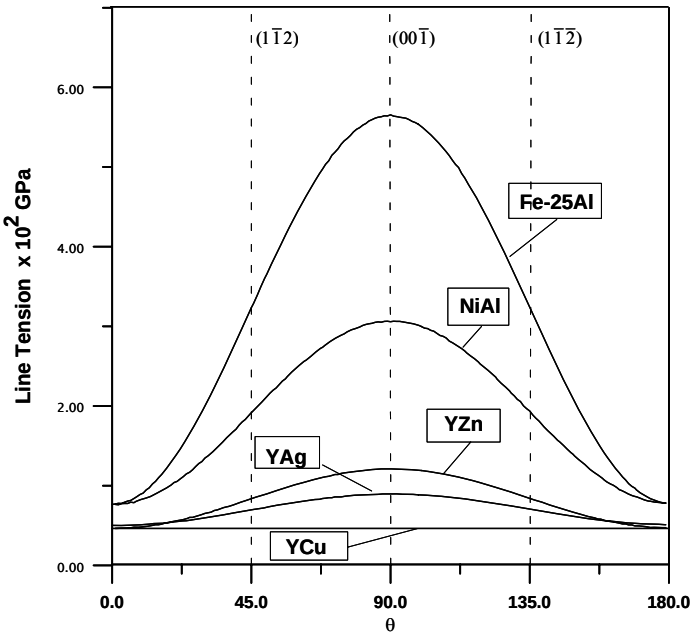

Figure 3.7 Variation of the line tension factor of [110] screw dislocations on various cross-slip planes.

3.2 Core properties of dislocations in YAg, YCu, and NiAl B2 intermetallics

3.2.1 Introduction

In recent years, there has been considerable renewed interest in the Peierls-Nabarro (P-N) model [19,20] to describe the dislocation cores and the mobility of dislocations, due to the accurate determination of generalized stacking fault energies (γ-surface) and the relatively small computational demand required by the model itself. The details of the

generalization of the P-N model from its original 1D treatment to 2D and stress assisted dislocation constriction and cross slip can be found in refs [21-24].

In this study, a generalized P-N model fitted to the generalized stacking fault energies calculated from *ab initio* density functional theory for YAg, YCu, and NiAl was employed in order to elucidate the intrinsic character of dislocations in ductile B2 YAg and YCu intermetallic alloys.

3.2.2 Methodology

The methodology used in this study closely follows the work of Schoeck [25,26] in which the core structure of dissociated dislocations in NiAl was studied within the framework of the generalized P-N model. It was shown [25] that the results obtained from the generalized P-N model by using the γ-surface determined from an EAM potential for NiAl were in excellent agreement with the result obtained from the direct atomistic simulations, which also used the same EAM potential [27].

For a dislocation having total Burgers vector $\boldsymbol{B}$, the resulting displacement can be expressed by superposition of fractional Peierls dislocations as:

$$u(x) = \sum \left(\frac{b_i}{\pi} \right) arctg \left[\frac{x - d_i}{w_i} \right] + \frac{b_i}{2} \tag{3.2}$$

where coordinate x is perpendicular to the dislocation line; b_i is the Burgers vector of the ith fractional dislocation positioned at d_i with width w_i and the condition such that

$B = \sum b_i$ is satisfied. The resulting elastic energy from the distribution of these fractional dislocations can be expressed in the compact form as:

$$E_{el} = \iint \frac{\partial u(s)}{\partial s} \frac{H}{x - s} u(x) ds dx \tag{3.3}$$

where H is the Stroh tensor for the prelogarithmic energy coefficients (see Eq. 2.24). Based on the anisotropic elastic constants and the dislocation line orientation, the H matrix can be calculated by the sextic formalism discussed in Chapter 2. A useful routine for H matrix calculation is given in ref. [28]. For YAg and YCu, the anisotropic elastic constants used in the calculation of this study are the same as the ones in Table 3.1; the data for NiAl are the same as those used in ref. [25] for comparison.

The misfit energy in the glide plane, part of the total energy, can be evaluated, by integrating the local γ-surface values along the displacement path:

$$E_{misfit} = \int_{-\infty}^{\infty} \gamma(u(x)) dx \tag{3.4}$$

In this study, the γ-surfaces for YAg, YCu, and NiAl were determined by using *ab initio* electronic-structure calculations based on DFT, namely, the Vienna *ab initio* simulation code (VASP) [29-31] and provided by C.Z. Wang and M. Ji [32]. Due to the symmetry, the results obtained from *ab initio* studies can be represented by a 2D Fourier series using reciprocal lattice vectors in the form of:

$$\gamma(y, z) = \sum_{m,n} C_{mn} \cos \frac{2\pi m y}{a\sqrt{2}} \cos \frac{2\pi n z}{a} \tag{3.5}$$

where y and z are the displacements in the lattice frame. The resulting Fourier series coefficients C_{mn} for YAg, YCu, and NiAl are given in Table 3.4.

Table 3.4 Fourier coefficients Cmn in Eq. 3.5 (unit: J/m^2).

YAg	n = 0	1	2	3	4	5
m = 0	5.27E-01	4.37E-02	-1.95E-02	9.62E-04	-1.59E-03	2.83E-04
1	-3.41E-01	-2.23E-01	1.35E-03	-4.49E-03	-4.87E-04	-2.95E-04
2	1.61E-02	1.17E-02	-1.47E-02	4.27E-04	-1.40E-03	1.10E-04
3	-1.70E-02	2.32E-02	1.82E-03	-8.79E-04	-1.54E-04	-3.70E-04
4	-4.58E-04	-4.28E-03	4.64E-03	5.15E-05	-2.29E-04	-1.91E-04
5	1.04E-03	-2.94E-03	-1.92E-04	1.19E-03	1.69E-04	-3.65E-05

YCu	n = 0	1	2	3	4	5
m = 0	6.46E-01	2.00E-02	-2.28E-02	-4.30E-05	-1.17E-03	4.26E-04
1	-4.10E-01	-1.90E-01	-1.48E-03	-7.47E-03	3.76E-04	-6.88E-04
2	-2.39E-02	7.80E-03	-1.46E-02	1.40E-03	-2.07E-03	-1.39E-04
3	-1.47E-02	1.04E-02	6.72E-03	-2.75E-04	3.96E-04	-1.18E-04
4	1.54E-03	-6.71E-03	3.40E-03	1.04E-03	1.93E-04	1.86E-04
5	-1.97E-04	3.83E-04	-3.21E-03	2.60E-04	5.27E-06	-1.87E-04

NiAl	n = 0	1	2	3	4	5
m = 0	2.61E-01	9.01E-02	-4.64E-02	5.60E-04	-1.25E-03	-7.30E-05
1	-3.64E-01	-5.96E-01	2.95E-03	-9.85E-03	-3.30E-04	-2.60E-04
2	1.23E-01	-1.10E-01	-2.59E-02	-1.83E-03	-1.41E-03	7.49E-05
3	7.67E-03	2.84E-02	-1.14E-02	-3.80E-03	-2.56E-04	-2.83E-04
4	-4.22E-03	7.90E-03	2.85E-03	-1.51E-03	-4.34E-04	-3.31E-04
5	-1.73E-04	-1.17E-03	1.04E-03	5.71E-04	-4.20E-05	5.64E-05

The γ-surfaces from the Fourier series fit are shown in Figure 3.8(a) and corresponding γ-surfaces contour plots are given in Figure 3.8(b).

The total energy due to the elastic energy and the misfit energy

$$E_{total} = E_{el} + E_{misfit} \tag{3.6}$$

can be minimized with the geometrical parameters in Eq. 3.2 that describe all possible configurations of the dislocations core. Therefore, according to Eq. 3.2, each partial can be designated with three geometrical parameters b_i, d_i and w_i. Due to the symmetry of γ-surface, it was assumed that one partial is located in the center ($x = 0$) with the width w_2, and the other two partials are positioned at d and $-d$, respectively, with the same width w_1. Furthermore, the Burgers vector of partials can be expressed by its screw r and edge s components, i.e.

$$b_1 = |b|\sqrt{r^2 + s^2}$$
$$b_2 = 2|b|\sqrt{(1-r)^2 + s^2} \qquad (3.7)$$
$$|b| = a\sqrt{3}/2$$

For example, when $r = 1$, $s = 0$, and $d = 0$, the dislocation is undissociated; when $r = 1$, $s = 0$, and $d \neq 0$, the dislocation is decomposed into two partials.

For $[100](01\bar{1})$ dislocations, to follow the energy-favorable path on the γ-surface, it was assumed that the [100] dislocation is dissociated into two symmetrical partials with the same screw components *B/2* and opposite edge components *s* and *–s*, respectively. Again, the two partials with the same width *w* are positioned at *d* and *–d*.

In this simulation, downhill simplex method (subroutine AMOEBA [33]) was used to minimize the total energy and obtain the balanced values for all of parameters. In the numerical evaluation of the misfit energy (Eq. 3.4) the value for the infinite integral and also in the evaluation of *H* tensor the required value for the outer cut of radius were all taken as $R = 1000|b|$.

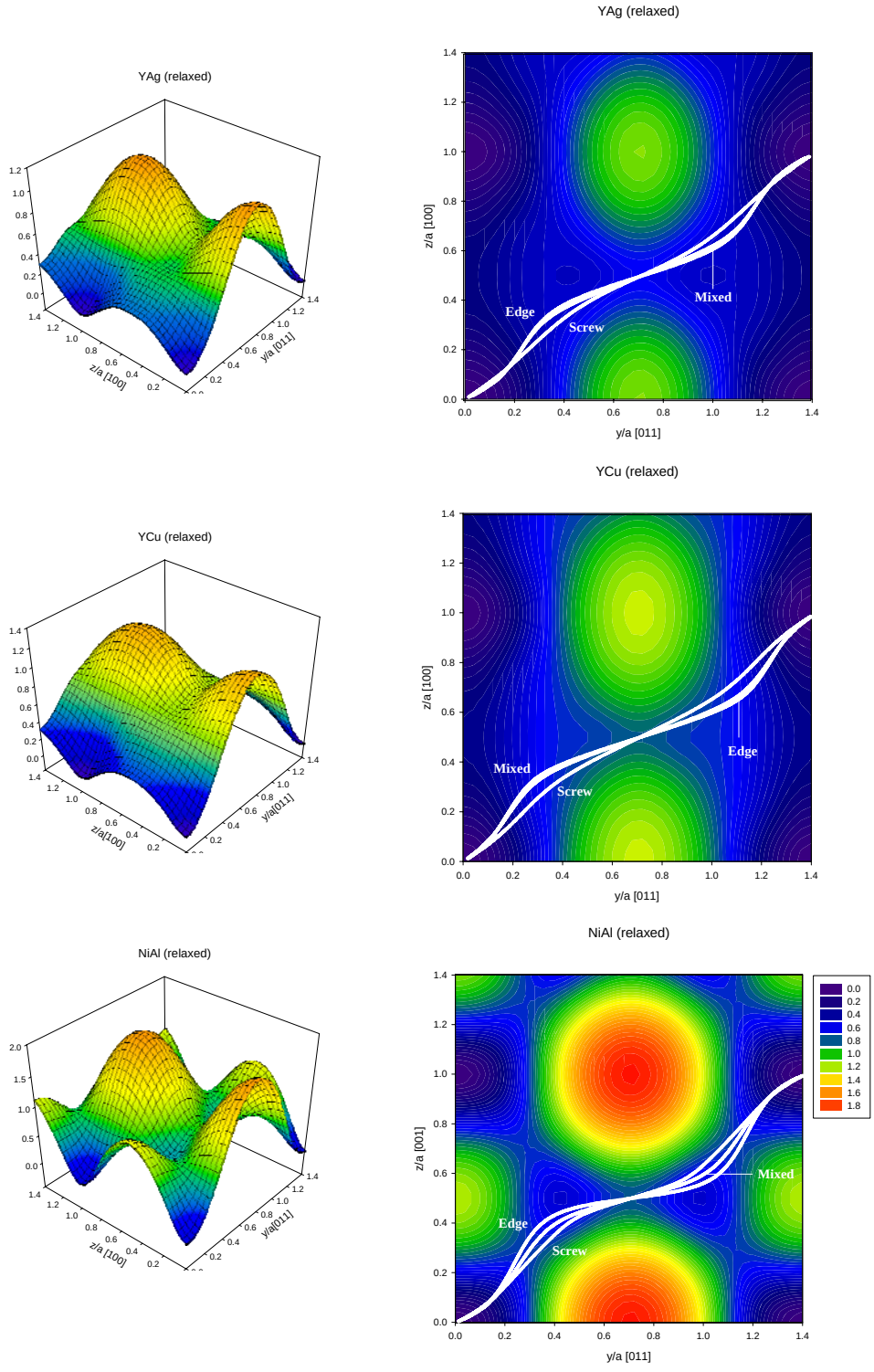

Figure 3.8 $(01\bar{1})$ γ-surfaces of YAg, YCu, and NiAl.

3.2.3 Results and discussion of dislocation core sizes

Figure 3.9 shows the generalized stacking fault energy (γ-curves) along <001> and <011> directions for YAg, YCu, and NiAl obtained from the *ab initio* calculations. The Figure also includes the results obtained from an EAM potential for NiAl as provided in [25]. For all three alloys, the absence of the intrinsic stacking faults (a local minimum) for both directions on $(01\bar{1})$ plane can be clearly seen from the Figure. In addition, unstable stacking fault energies (the maximum values on the curves) are lower for YAg and YCu than the one seen for the NiAl. The value for YAg is slightly lower than that of YCu. Also, the difference between the maximum values is larger in <001> direction. While the generalized stacking fault energy for NiAl obtained from the *ab inito* calculations and the EAM potentials agree closely with each other in <011> direction, somewhat, the values differ in <001> direction.

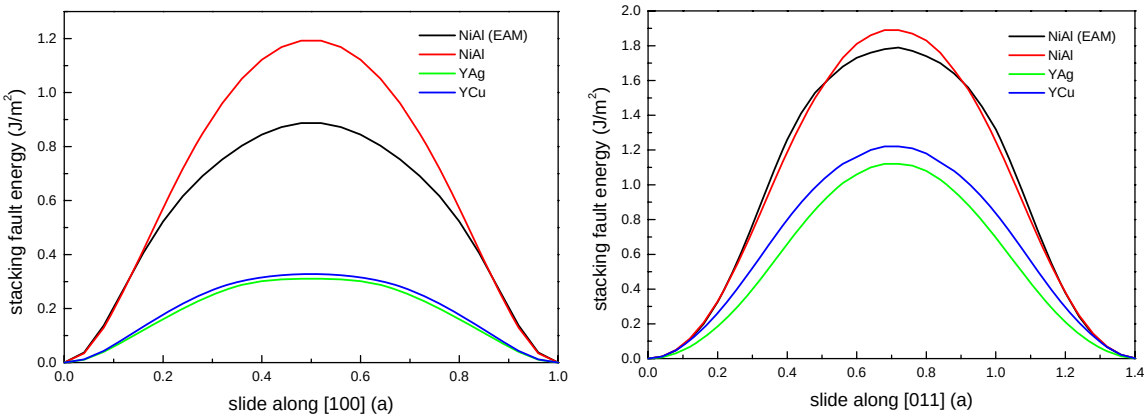

(a) (b)

Figure 3.9 (a) Cross sections at y = 0 of the γ-surfaces for $(01\bar{1})$ plane in NiAl, YAg, and YCu; (b) cross sections at z = 0 of the γ-surfaces for $(01\bar{1})$ plane in NiAl, YAg, and YCu.

3.2.3.1 [111]{110} dislocations

For $[111](01\bar{1})$ dislocations, based on the shape of the γ-surface in $(01\bar{1})$ plane, it can decompose into three partials as suggested in ref. [25]. After the minimization process, the resulting equilibrium values of the geometrical parameters, for the dislocations having edge, mixed (with [100] line direction), and screw characters for this slip system are summarized in Table 3.5. Also, the results based on the γ-surface derived from Ludwig potential (an EAM potential) [25] for NiAl are given for the comparison purpose.

As can be seen from Table 3.5, for the edge and mixed character in NiAl, the calculation results are very close to those from ref. [25] in terms of the five parameters, and the total minimized energy evaluated here is even lower. For any dislocation character, it is seen that [111]{110} dislocations in NiAl, YAg, and YCu can dissociate into three partials to follow the lowest energy path determined by the $\gamma\,(01\bar{1})$ surface (see Figure 3.8). The similar splitting mode, based on the direct atomistic calculations [34,35] is also seen for NiAl. For the edge character, the splitting distances for NiAl, YAg, and YCu are 6.42 Å, 6.74 Å, and 6.38 Å, respectively. For the mixed character, they decrease to 5.58 Å, 6.4 Å, and 6.06 Å. For the screw character, the splitting distances further drop to 2.9 Å, 3.28 Å, and 3.06 Å, which are approximately half of those of the edge dislocations. This trend of change has a close agreement with the results calculated from the atomistic calculation and the reason is the weaker interactions between the partials in case of the screw character [27]. The displacement path u(x) of these dislocations is shown in the

Table 3.5 Summary of the calculated equilibrium geometrical parameters, peierls energy and peierls stress for [111]{011} dislocations.

	Line direction	Character	Geometrical parameters					Peierls energy (eV/ Å)	Peierls stress (GPa)
			r	s	d (Å)	w_1 (Å)	w_2 (Å)		
YAg	$[2\bar{1}\bar{1}]$	Edge	0.25	0.35	6.74	3.09	4.55	0.0083	0.11
	[100]	Mixed	0.26	0.26	6.4	2.39	3.85	0.0091	0.12
	[111]	Screw	0.5	0.2	3.28	2.19	2.55	0.017	0.23
YCu	$[2\bar{1}\bar{1}]$	Edge	0.34	0.24	6.38	2.56	2.56	0.0053	0.095
	[100]	Mixed	0.34	0.24	6.06	1.89	2.24	0.0024	0.075
	[111]	Screw	0.28	0.18	3.06	1.67	2.02	0.0074	0.11
NiAl	$[2\bar{1}\bar{1}]$	Edge	0.43	0.43	6.42	2.39	3.83	0.0029	0.06
	[100]	Mixed	0.44	0.34	5.58	2.13	3.57	0.0072	0.14
	[111]	Screw	0.61	0.21	2.9	0.88	1.75	0.066	1.8
NiAl (EAM)	$[2\bar{1}\bar{1}]$	Edge	0.44	0.34	7.26	1.27	3.77	0.0061 (0.165)	0.13 (0.07)
	[100]	Mixed	0.44	0.27	6.48	1.18	3.69	0.0066	0.14 (0.23)
	[111]	Screw	-	-	-	-	-	0.028 (0.524)	2.02 (2.0)

contour plots Figure 3.8(b). For the pure edge and screw character, the edge components u_e (Å) and the corresponding dislocation density du_e / dx of three fractional dislocations are shown in Figure 3.10, and for the mixed character, the screw components z(x) (Å) (along [100] direction) and the corresponding dislocation density dz / dx of three partials are shown in Figure 3.11. Again, the dissociation into three partials (three peaks on the dislocation density curves) can be clearly seen and the pure edge dislocations present the largest splitting distances, followed by the mixed dislocations and the pure screw dislocations. In addition, the splitting distances of those dislocations determine the level of the magnitude of Peierls stress, which will be discussed later.

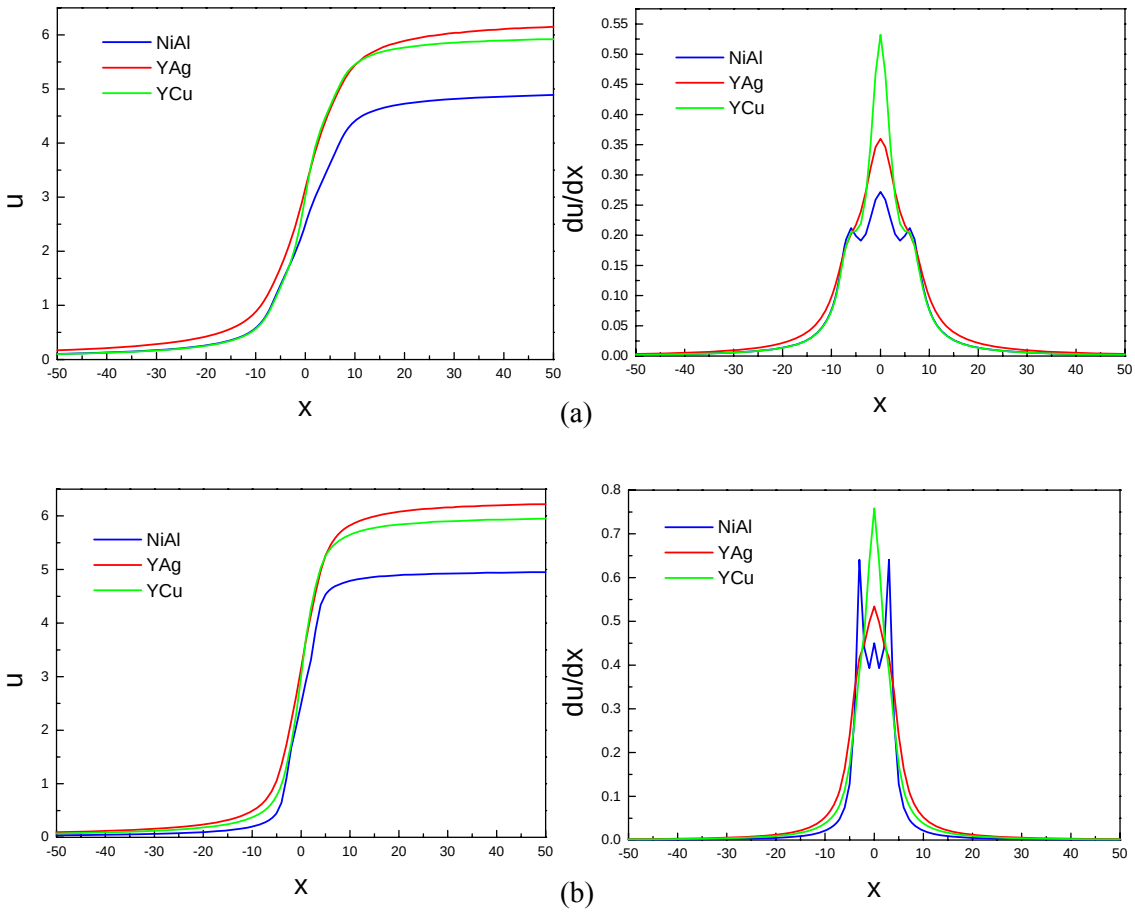

Figure 3.10 Displacement profile u(x) and density distribution du/dx of the edge components in the (a) edge character and (b) screw character of [111]{110} dislocations.

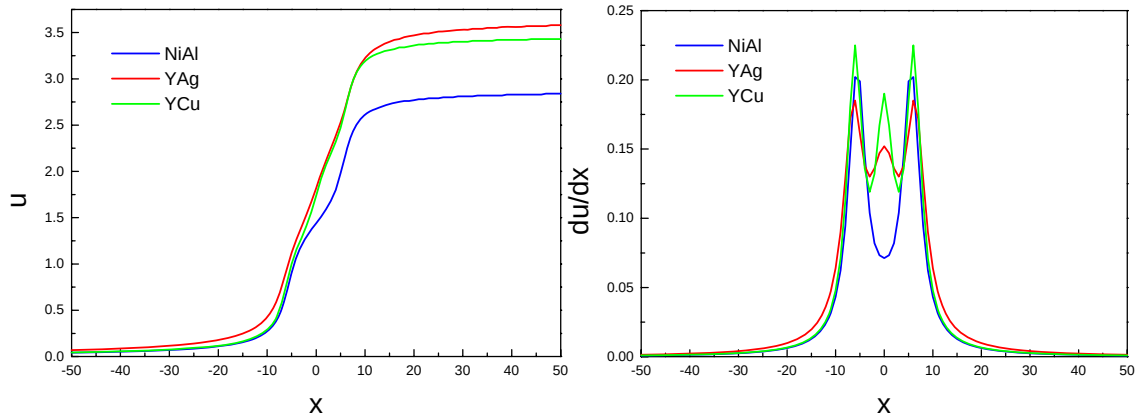

Figure 3.11 Displacement profile Z(x) and density distribution dZ/dx in the mixed [111]{110} dislocations with [100] line direction.

3.2.3.2 [100]{110} dislocations

As can be seen from Table 3.6, unlike [111] dislocations, [100] dislocations on the same slip plane show different splitting modes in NiAl, YAg, and YCu. The dislocation with the pure screw character in NiAl clearly dissociates into two partials to follow the energy-favorable displacement path (s = 1.88 Å and d = 8.22 Å). However, due to the lower stacking fault energy along [100] direction in YAg and YCu, although the [100] dislocations in these RM B2 intemetallics also show certain splitting behavior with splitting distance at 5.52 Å and 2.06 Å, respectively, it was noticed that the value of s for them is so small (-0.32 Å and –0.03 Å) and approximately near to zero. Thus, the [100] screw dislocation in YAg and YCu is expected to dissociate with the reaction:

$$[100] \longrightarrow \tfrac{1}{2}[100] + \tfrac{1}{2}[100]$$

For the pure edge and mixed character, [100] dislocations in YAg and YCu show the dissociation mode similar to that seen for the pure screw character. But the magnitude of splitting distance for three B2 alloys is clearly different. The dislocation in NiAl shows

the narrowest core splitting (0.99 Å for mixed and 1.92 Å for edge), followed by YCu (3.11 Å for mixed and 3.07 Å for edge), and YAg (3.15 Å for mixed and 3.51 Å for edge).

The displacement paths u(x) of the [100] dislocations in these three alloys are shown on their γ-surface contour plots in Figure 3.12. For NiAl, the result from the atomistic simulation with EAM potentials [35] is also shown for comparison. It can be clearly seen that the displacement path in NiAl calculated here shows a good agreement with that from atomistic simulation. Likewise, the edge components u_e and the corresponding dislocation density du_e / dx of two fractional dislocations are shown in Figure 3.13. The dissociation into two partials is apparent. The variation of splitting distances, as discussed before, is also presented in the dislocation density curves.

Table 3.6 Summary of the calculated equilibrium geometrical parameters, peierls energy and peierls stress for [100]{011} dislocations.

	Line direction	Character	Geometrical parameters			Peierls energy (eV/ Å)	Peierls stress (GPa)
			s (Å)	d (Å)	w (Å)		
YAg	[100]	screw	-0.32	5.52	6.25	0.41e-4	0.0016
	[111]	mixed	-0.13	3.15	2.79	0.0029	0.12
	[011]	edge	-0.14	3.51	3.15	0.0017	0.066
YCu	[100]	screw	-0.03	2.06	1.71	0.0092	0.39
	[111]	mixed	-0.02	3.11	2.07	0.0037	0.16
	[011]	edge	-0.057	3.07	2.38	0.0025	0.1
NiAl	[100]	screw	1.88	8.22	5.63	0.27e-4	0.0016
	[111]	mixed	1.28	0.99	0.99	0.032	6.06
	[011]	edge	1.34	1.92	1.05	0.02	1.32
NiAl (EAM)	[100]	screw	-	-	-	0.41e-4 (0.013)	0.0009 (0.07)
	[111]	mixed	-	-	-	0.016	1.01 (0.17)
	[011]	edge	-	-	-	0.056 (0.008)	3.99 (0.06)

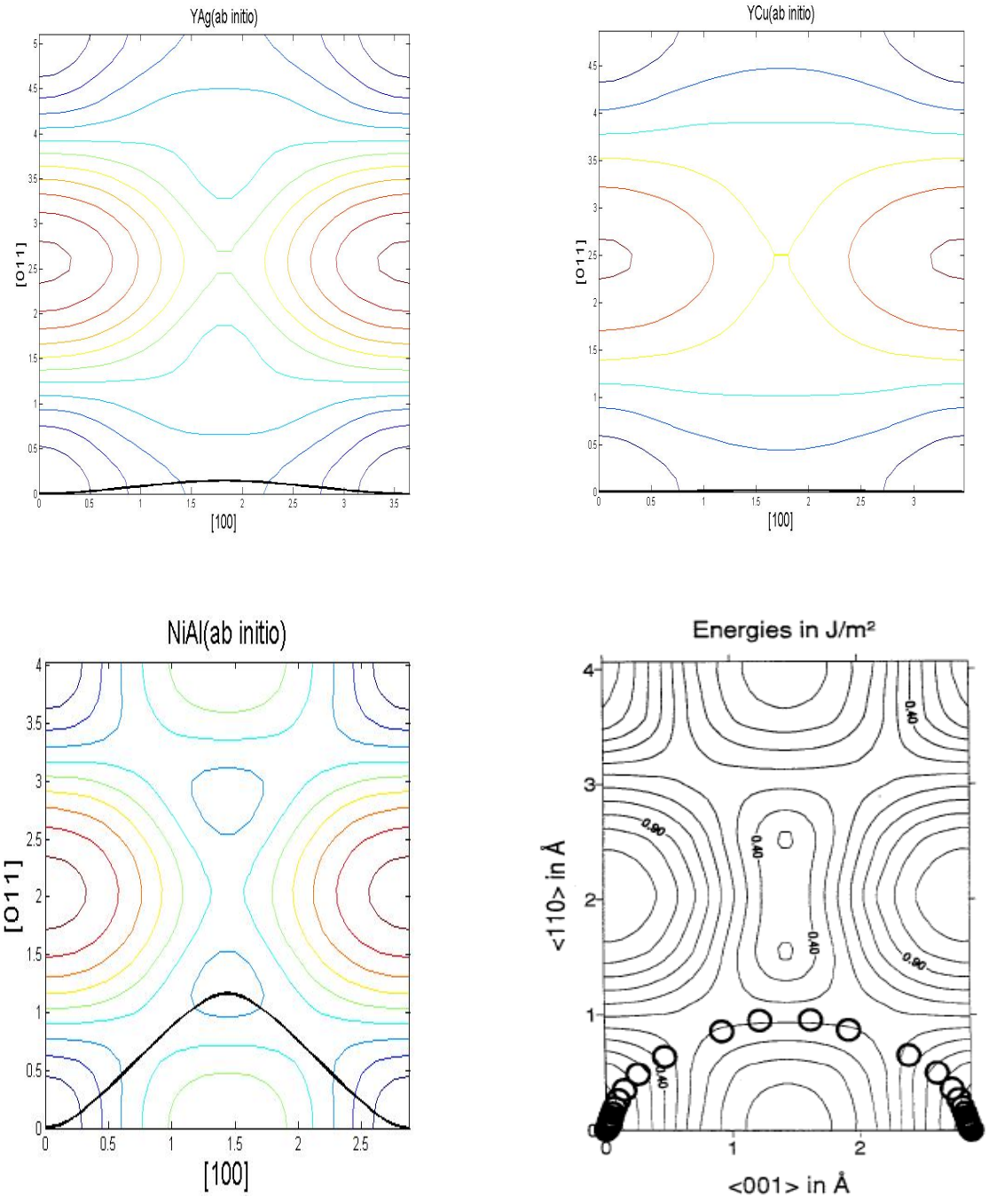

Figure 3.12 Displace path of [100] screw dislocations in (a) YAg, (b) YCu, and (c) NiAl; (d) results from atomic calculation with EAM potential [35].

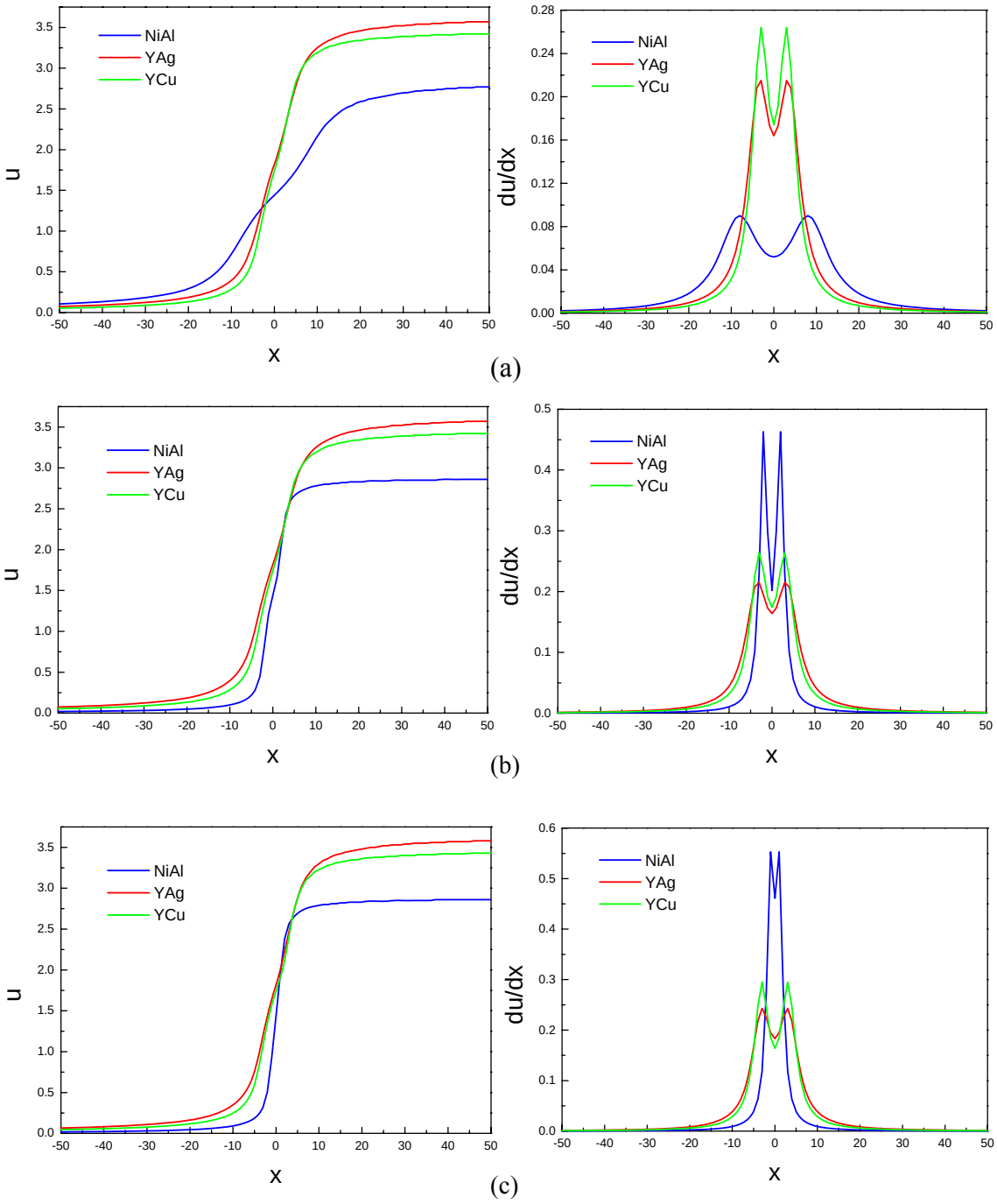

Figure 3.13 Displacement profile u(x) and density distribution du/dx of the edge components in (a) screw character, (b) edge character, and (c) mixed character with [111] line direction of [100]{110} dislocations

3.2.4 Peierls Energy and Peierls Stress

In this study, the analysis on the Peierls energy and the Peierls stress is also included. To calculate the misfit energy by integrating γ-surface along the displacement path u(x), the misfit energy on the slip plane is averaged. In fact, the misfit energy is only defined at the atomic positions. Thus, the calculation of misfit energy should be performed by the discrete summation of the γ-surface value at each parallel atom rows positioned at $x = nh$, where h is the distance between two neighbor atom rows. In addition, when the center of a dislocation in shifted within one lattice cell, the dislocation energy is also changed periodically and is the function of a fraction t $(0 \le t \le 1)$ of the lattice constants. The amplitude of the variation of dislocation energy is defined as Peierls energy. The corresponding value of Peierls stress can be calculated as $(1/b^2) \cdot (dE(t)/dt)_{\max}$. Originally, it was assumed that the shifting of a dislocation center from its equilibrium position is rigid and only the variation of the misfit energy contributes to the Peierls energy; however, when the further relaxation is permitted, the geometrical parameters can also be adjusted to obtain the lower energy. In this case, the variation of both elastic energy and misfit energy makes effects on the resulting Peierls energy. In this study, during the minimization process, for a given *t*, all possible geometrical parameters were allowed to be relaxed to obtain the lowest total energy.

The Peierls energy and the Peierls stress calculated from this simulation and from the atomistic calculation with Ludwig potential [27] for NiAl (values in the parentheses) are all included in Tables 3.5 and 3.6.

For [111]{110} dislocations**,** for the edge character, YAg has the highest Peierls stress at 0.11GPa, followed by YCu at 0.095GPa and NiAl at 0.06GPa. For the mixed character, the Peierls stress for NiAl increases to more than twice of one with the edge character, and for YAg the stress value also increases a little, from 0.11GPa to 0.12GPa. But for YCu, the stress value decreases to 0.075GPa. More importantly, for the screw character, the Peierls stress for NiAl (1.8GPa) is approximately one order of magnitude higher than that of the edge and mixed types, and for YAg (0.23 GPa) and YCu (0.11GPa), the corresponding Peierls stress is also the largest compared to the case of edge and mixed character. The contracted core width (splitting distance) makes dislocations move harder and contributes to this increase on the Peierls stress. In many bcc crystals, [111] screw dislocations restrict the plastic deformation of [111]{110} slip system [27], which is also observed in the deformation experiments of NiAl single crystals [36].

For [100]{110}dislocations, due to the relation between splitting distance and Peierls stress, the Peierls stress of [100] screw dislocations in YCu (0.39GPa) shows two orders of magnitude larger than those in NiAl (0.0016GPa) and YAg (0.0016GPa). However, it is shown that the Peierls stress of [100] edge and mixed dislocation in NiAl is at least one order of magnitude larger than that in YAg and YCu, and the stress value of YAg is slightly lower than that of YCu. As seen in the {110} γ surface, the stacking fault energy along [100] slip direction in YAg (315mJ/m^2) and YCu (325mJ/m^2) is lower; however, the corresponding energy level for NiAl (1290mJ/m^2) exceeds the anti-phase boundary (APB) energy, which suggests that [100] slip modes in RM B2 alloys are much easier to

be activated [8]. Russell et al. [37,38] also found that the <001> direction was the active slip direction from the tensile test on single crystal specimens of YAg and YCu.

It can be seen that there is a significant difference on the values of Peierls energy and Peierls stress between the results calculated from the generalized P-N model and the ones from the atomistic calculation. There are several factors that could influence the absolute value of the Peierls energy and the Peierls stress given in Tables 3.5 and 3.6 [25,27,39,40]. First, fully atomic relaxation may change those values [27,40]. As discussed before, the relaxation of all the possible geometrical parameters during the process of shifting the dislocation center is allowed to consider the contribution of the variation of elastic energy to the Peierls energy. However, the calculation in ref. [27] is based on a simple method with the assumption that the core structure doesn't change during the shifting, i.e. "rigid shift". Since the Peierls energy is usually only a fraction of (in the order of 10^{-2}-10^{-3}) the elastic energy, the small fluctuation of the elastic energy may cause the significant change on the Peierls energy. Second, given the lattice resistance to the dislocation motion, the displacement is only defined at the discrete atomic positions; however, the elastic energy still depends on the displacement between parallel rows of atoms. Although the approach of interpolation is used, this still may result in the variation of the elastic energy because the interpolation affects both the screw and edge components simultaneously when the dislocation core spreads to 2D [39]. Finally, as it was pointed out in ref. [41] that summing the atomic energy only at the positions of atoms is not physically realistic. Within the framework of *ab initio* electronic-structure calculations based on DFT, the misfit energy is not localized, but

involved in the electron distribution. Therefore, the misfit energy has to be averaged, which can lead to a considerable reduction in the Peierls energy and the resulting Peierls stress.

3.3 Summary

In the first section of this chapter, the stability of ordinary dislocations, the interaction energies of kink pairs and the cross-slip behavior of screw dislocations in ductile rare-earth intermetallic compounds YCu, YAg, and YZn were evaluated by calculating energy factor K and the corresponding line tension factor $K + K''$. The results were also compared to the ones from the common intermetallics NiAl and Fe-25Al.

Subsequently, in the second section, the generalized 2-D Peierls-Nabarro Model was employed to study [111]{110} and [001]{110} dislocation core properties in NiAl, YAg, and YCu, including dislocation dissociation, Peierls energy, and Peierls stress.

The conclusions from these two studies are summarized as follows:

- The convex shape of the inverse energy plots and positive line tension show that the elastic anisotropy does not cause any instability of ordinary dislocations in YCu, YAg, and YZn.
- Kink pair interaction characteristics of YAg and YZn are similar to those seen for NiAl and Fe-25Al.
- Cross-slip in YCu, YAg, and YZn is less favorable for certain slip systems, in comparison to NiAl and Fe-25Al, due to the absence of negative line tension in

these rare-earth intermetallic compounds. On the other hand, cross-slip for [110] orientation is more favorable in YCu, YAg, and YZn due to the small differences in the line tension values of the cross-slip planes.

- [111]{110} dislocations in NiAl, YAg, and YCu can dissociate into three partials to follow the lowest energy path determined by the $\gamma-(01\bar{1})$ surface. Given a certain dislocation orientation, the splitting distances of partials in the three intermetallics are very close.
- [100]{110} dislocations in YAg and YCu are expected to dissociate into two partials with the same Burgers vector $\frac{1}{2}[100]$.
- The Peierls stress of [100]{110} dislocations with the pure edge and mixed character in NiAl is at least one order of magnitude larger than that in YAg and YCu, which indicates that [100] slip modes in RM B2 alloys are much easier to be activated.

Reference

[1] Glatzel, U., Forbes, K., and Nix, W., 1993, *Phil. Mag.*, **67**, 307.
[2] Yoo, M., Yoshimi, K., and Hanada, S., 1999, *Acta Mater.*, **47**, 3579.
[3] Jiao, Z., Whang, S., Yoo, M. and Feng, Q., 2002, *Mater. Sci. Eng.*, **A329**, 171.
[4] Stroh, A., *Phil. Mag.*, 1958, **3**, 625.
[5] Head, A., 1967, *Phys status solidi*, **19**,185.
[6] Friedel, J., 1964, *Dislocations.*, Pergamon Press, Oxford, p.32
[7] Wang, L. and Lothe, J., 1995, *Phil. Mag. A*, **71**, 359.
[8] Morris, J., Ye, Y., Lee, Y-B, Harmon, B., Gschneidner, Jr. K. and Russell, A., 2004, *Acta Mater.*, **52**, 4849.

[9] Schiltz, Jr. R., Prevender, T., and Smith, J., 1971, *J. App. Phys*., **42**, 4680.

[10] Shi, X., Mahajan, S., Pollock, T. M., and Arunachalam, V. S., 1999, *Phil. Mag. A*, **79**, 1555.

[11] Field, R., Lahrman, D., and Darollia, R. 1991, *Acta Metall. Mater*., **39**, 2951.

[12] Crimp, M., Tonn, S.C., and Zhang, Y., 1993, *Mater. Sci. Eng.*, **A170**, 95.

[13] Shi, X., Pollock, T., and Arunachalam, V., 1997, *Mater. Res. Soc. Symp. Proc*., **460**, 493.

[14] Fraser, H., Smallman, R., and Loretto, M., 1973, *Phil. Mag.*, **28**, 651.

[15] Caillard, D., Vailhe, V., and Farkas, D., 1999, *Phil. Mag. A*, **79**, 723.

[16] Schroll, R., Gumbsch, P., and Vitek, V., 1997, *Mater. Sci. Eng. A*, **233**, 116.

[17] Schroll, R., Vitek, V., and Gumbsch, P., 1997, *Acta Mater*., **46**, 903.

[18] Sun, Y. and Ngan, A., 1996, *Phil. Mag. Let*., **74**, 175.

[19] Peierls, R., 1940, *Proc. Phys. Soc. Lond*., **52**, 34.

[20] Nabarro, F., 1947, *Proc. Phys. Soc. Lond*., **59**, 256.

[21] Schoeck, G., 1994, *Phil. Mag. A*, **69**, 1085.

[22] Schoeck, G., 1997, *Acta Metall. Mater*., **45,** 2597.

[23] Bulatov, V. V. and Kaxiras, E., 1997, *Phys. Rev. Lett*, **78**, 4221.

[24] Lu, G., Bulatov, V., and Kioussis, N., 2004, *Int. J. Plasticity*, **20**, 447.

[25] Schoeck, G., 2001, *Acta Mater*., **49,** 1179.

[26] Schoeck, G., 1997, *Phil. Mag. Lett*., **76**, 15.

[27] Schroll, R., Vitek, V., and Gumbsch, P., 1998, *Acta Mater*., **46**, 903.

[28] Head, A. et al., 1973, in *Computed Electron Micrographs and Defect Identification*, Vol. 7, *Defects in Crystalline Solids*, ed. S. Amelinckx. North-Holland, Amsterdam.

[29] Kresse, G. and Joubert, J., 1999, *Phys. Rev. B*, **59**,1758.

[30] Perdew J., Burke K., and Ernzerhof M., 1996, *Phys. Rev. Lett.*, **77**, 3865.

[31] Kresse G. and Furthmuller J., 1996, *Phys. Rev. B*, **54**, 11169.

[32] Wang, C. Z. and Ji, M. (unpublished work).

[33] Press W. et al., *Numerical Recipes in FORTRAN: The Art of Scientific Computing*, 2nd Edition, (Cambridge University Press, 1992).

[34] Xie, Z., Vailhe, C., and Farkas, D., 1993, *Mater. Sci. Engng A*, **170**, 59.

[35] Vailhe, C. and Farkas, D., 1999, *Phil. Mag. A*, **79**, 921.

[36] Sun, Y., Taylor, G., Darolia, R., and Hazzledine, P., 1995, *Mater. Res. Soc. Symp. Proc.*, **364**, 261.

[37] Russell, A., Zhang, Z., Lograsso, T. A., Lo, C., Pecharsky, A., Morris, J. R., Ye, Y., Gschneidner, Jr. K., and Slager, A., 2004, *Acta Mater*., **52**, 4033.

[38] Russell, A., Zhang, Z., Gchneidner, Jr. K., Lagrasso T., Pecharsky, A., Slager, A., and Kesse, D., 2005, *Intermetallics*, **13**, 565.

[39] Schoeck G., 2001, *Comp. Mate. Sci.*, **21**, 124.

[40] Lu G., Kioussis N., Bulatov V. V., and Kaxiras E., 2000, *Phil. Mag. Lett.*, **80**, 675.

[41] Schoeck G., 1999, *Phy. Rev. Lett.*, **82**, 2310.

CHAPTER 4

EVOLUTION AND INTERACTION OF DISLOCATIONS IN INTERMETALLIC COMPOUNDS: 3D ANISOTROPIC DISLOCATION DYNAMICS SIMULATIONS

This chapter presents the results obtained from the fully 3D anisotropic dislocation dynamics simulations, the algorithm of which can be found in Chapter 2, for five intermetallic alloys YAg, YCu, YZn, NiAl, and Fe-25Al and discusses the effect of anisotropy on typical dislocation mechanisms, including Frank-Read source evolution, dislocation dipole formation, and dislocation junction formation.

4.1 Frank-Read source evolution

It is known that Frank-Read mechanism of dislocation generation and multiplication is one of the main sources for the increase in plastic strain during the course of deformation. Figure 4.1 summarizes the evolution of dislocation loops from a Frank-Read (F-R) source in Fe-25Al, NiAl, and YCu (The results in YAg and YZn are omitted here for clarity.). The configuration of the F-R source is a pure screw dislocation ($b = \frac{1}{2}[111]$), located on $(1\bar{1}0)$ glide plane and $1000\sqrt{3}|b|$ in length with two pinned ends. The segment length used in the simulation is $40|b|$. At the first step, the initial applied uniaxial stress is 75 *MPa* with [100] direction, and after that, the increment of applied stress $\Delta\sigma$ equals to 0.1 *MPa* at each time step which is taken as 1.0e-13s. The evolution of dislocation loops in Figure 4.1 at different applied stress levels clearly reflects the role of the elastic

anisotropy. As can be seen, in the case of YCu, a second loop has already formed and expanded considerably at 1088 *MPa* stress level, however, the original F-R sources in both NiAl and Fe-25Al are at very early stages of this process (Figure 4.1c). Moreover, this Figure also clearly indicates one of the possible reasons for the high ductility of B2 rare-earth intermetallics, since the plastic strain is described with the area swept by dislocation loops.

4.2 Dislocation dipole formation and breakup

Two approaching dislocations with opposite Burgers vectors, gliding on nearby parallel planes, can reach an equilibrium configuration by forming a dipole. This stable configuration arises because the interaction forces between them reduce to zero resulting from the opposing signs of theirs Burger vectors. In the numerical simulations, if proper care is taken, the dipoles form naturally. Of course, one of the critical criteria is the separation distance of the glide planes due to the long-range stress field of dislocations. M. Rhee et al. [1] developed a criterion for the infinite length dipole formation, i.e., there is a critical separation distance h_c for dipole formation, which is a function of their relative velocity V_R. When the stress applied on the dipoles exceeds the attractive forces between the dislocations forming the dipole, the dipole will eventually break, and the two dislocations involved in this process will separate from each other.

J. Huang et al. [2] focused on the study of dynamic formation and breakup for finite-size dipoles. In their work, the two dislocation lines with mixed character form a dipole with a straight and tilted middle section. The attractive forces on the middle straight section

and the self-forces on the two end sections close to the pinning points determine the length of this middle section. Their results also show that it is much easier to unzip the dipole in the reverse direction than to destroy it in the forward direction (pushing the two dislocations past one another). That is, the unzipping strength is smaller than that destructive force in the forward direction. Because of the self-forces generated by the curvature at the two end sections, the unzipping strength is also smaller than the strength of infinite dipoles. In addition, increasing the distance between two parallel planes makes the effect from the curvature at the two end sections weaker, and thus both unzipping and forward destructive stresses approach the values of an infinite dipole.

Figure 4.2 shows the configurations (2-D projections on $(1\bar{1}0)$ plane) of two pinned dislocation segments in five intermetallics, which are located on two parallel $(1\bar{1}0)$ planes with the separated distance $100\sqrt{2}|b|$. The two dislocations with the opposite line direction and the same Burgers vector $b=\frac{1}{2}[111]$ are initially straight, parallel and along [110] direction. The length of each dislocation is $1000\sqrt{2}|b|$. The segment length and the time step used in this simulation are $40|b|$ and 5.0e-13s, respectively. Without any applied external force, the two dislocation segments attract each other and form an equilibrium status of dipole. Again, the dislocations in alloys with higher anisotropic ratio move slower because of the higher line tension. Also, it can be seen that there are some kinks generated along the two dislocations in Fe-25Al due to the negative line tension as discussed in Chapter 3.

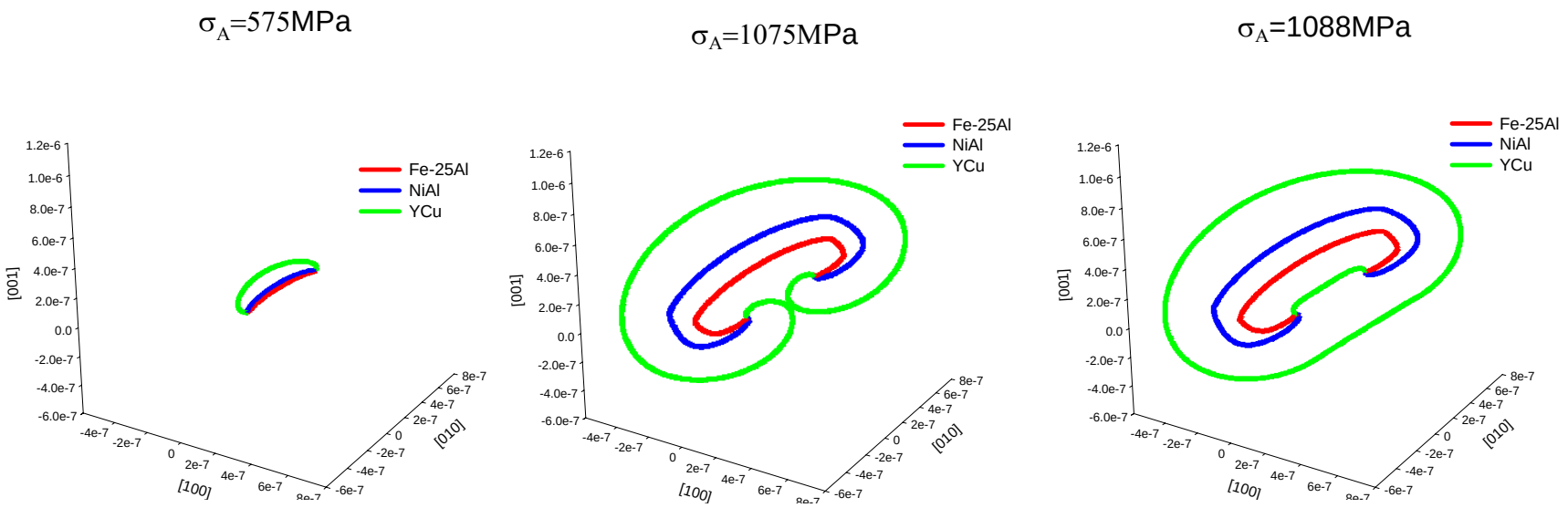

Figure 4.1 Evolution of an F-R source under an applied stress.

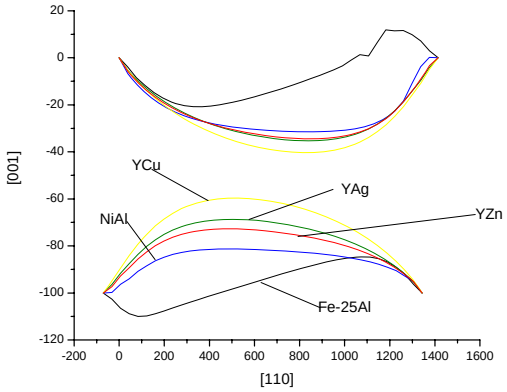

Figure 4.2 Evolution of dislocation dipoles (equilibrium status).

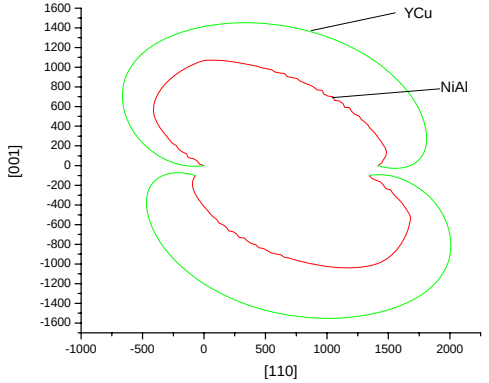

Figure 4.3 Dipole breaking in YCu and NiAl.

In the simulation of the breakup process, the applied stress increment at each time step (Δt=5.0e-13s) equals to 0.2 *MPa* along $[\bar{1}00]$ direction. Under the increasing applied stress, the two dislocations bow toward the opposite direction destroying the dipole configuration. Figure 4.3 shows the configuration of the dislocations at this breakup moment in NiAl and YCu under the same external applied stress level ($\sigma = 600MPa$ at $t = 1.5ns$). It can be clearly seen that the dipoles more easily break in the intermetallic alloys with lower anisotropic ratio than the ones in intermetallics with higher anisotropic ratio. This process can also lead to higher ductility in new rare-earth based B2 alloys.

4.3 Dislocation junction formation and breakup

When two attractive dislocations with nonparallel Burgers vectors in intersecting planes approach each other, the junction forms once the force between them reaches a critical value. In most cases, the junction nodes are immobile because of the geometry of the slip planes. Thus the formation of the junction resists the further motion of dislocations leading to the macroscopically observed work hardening during the course of the plastic deformation. Many researchers have studied the process of dislocation junction formation, but no quantitative analysis was performed except for the recent work of Bulatov et al. [3]. Generally, whether a junction can form depends upon the energy value between two junction nodes. That means two dislocation lines need to align themselves to minimize the energy and then form a junction. Let the two reaction dislocation segments 1 and 2 and the resulting junction 3 be arranged as shown in Figure 4.4. Along the direction of the junction, for a given virtual junction length, Δx, the corresponding energy change was given as: [4]

$$\Delta E = [-E_3 + E_1 \cos\alpha - \frac{\partial E_1}{\partial \varphi_1}\sin\alpha + E_2 \cos\beta - \frac{\partial E_2}{\partial \varphi_2}\sin\beta]\Delta x \tag{4.1}$$

As shown in Figure 4.4, *E_1, E_2 and E_3* are elastic energies of the two dislocations and the junction; α and β are angles between the two dislocation lines and the intersection line, respectively; φ_1 and φ_2 represent the angles between each Burgers vector and the corresponding dislocation line. If $F = \Delta E / \Delta x \geq 0$ (which can be interpreted as the energy decrease of the system per unit length of junction line formation), the reaction is stable and junction forms; otherwise, it's unstable. In the case of no external applied stress, the attractive forces on the middle straight section of a junction balance the self-forces on the four curved arms.

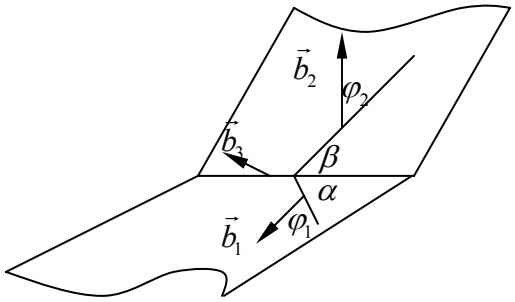

Figure 4.4 Schematic configuration of a junction reaction.

Eq. 4.1 is just a simple approximation, since the core energy of the reacting dislocations and the elastic interactions between different arms are not included. However, this simple and computationally very efficient energy minimization procedure quickly yields information about the possible junction configurations for given anisotropic elastic properties, slip systems and dislocation configurations. It can be used as the guidance to the computationally demanding discrete dislocation simulations. It is estimated that there are over 1700 such possible dislocation configurations that form junctions in *bcc* crystalline systems [4]. In this calculation, in order to take into account the full

anisotropy, sextic formalism (Eq. 2.24) was utilized to obtain the elastic energies of dislocations and corresponding derivatives. From this procedure, the resulting energy decrease contours for $[111](1\bar{1}0)\,\&\,[1\bar{1}\,\bar{1}](101)$ and $[111](1\bar{1}0)\,\&\,[1\,\bar{1}\,\bar{1}](110)$ slip systems for these five intermetallic alloys are summarized in Figures 4.5 and 4.6, respectively. In these figures, each contour map was normalized with the largest value of the energy decrease among the five intermetallic alloys. The x and y axes signify the angles between two dislocation arms and the intersection line, which correspond to the angles α and β as shown in Figure 4.4, respectively. As can be seen, the stable junction formation takes place at much wider angular range in Fe-25Al and NiAl in comparison to ones that are seen for the rare earth intermetallics. Furthermore, the contour plots also indicate that the junction formation is more favorable in these two common intermetallic alloys than the ones in YCu, YAg, and YZn due to the larger energy decrease.

In this section, a more detailed analysis for the evolution of dislocation junctions in these five intermetallic alloys was performed by using 3D anisotopic dislocation dynamics simulations. During these simulations, the dislocations had the initial length around 700 Å and were composed of linear segments 12.5 Å in length. At the beginning of the simulations, two straight dislocations with the same length, intersecting each other at their midpoints, were placed together. Both dislocations were also pinned at their end points during the course of the simulations. The time step used for junction forming is 2.0e-15 s and the resistivity (B matrix appearing in Eq. 2.25) equals to 1.0e-4 $Pa \cdot s$. During the junction formation process, the simulations were carried out under zero

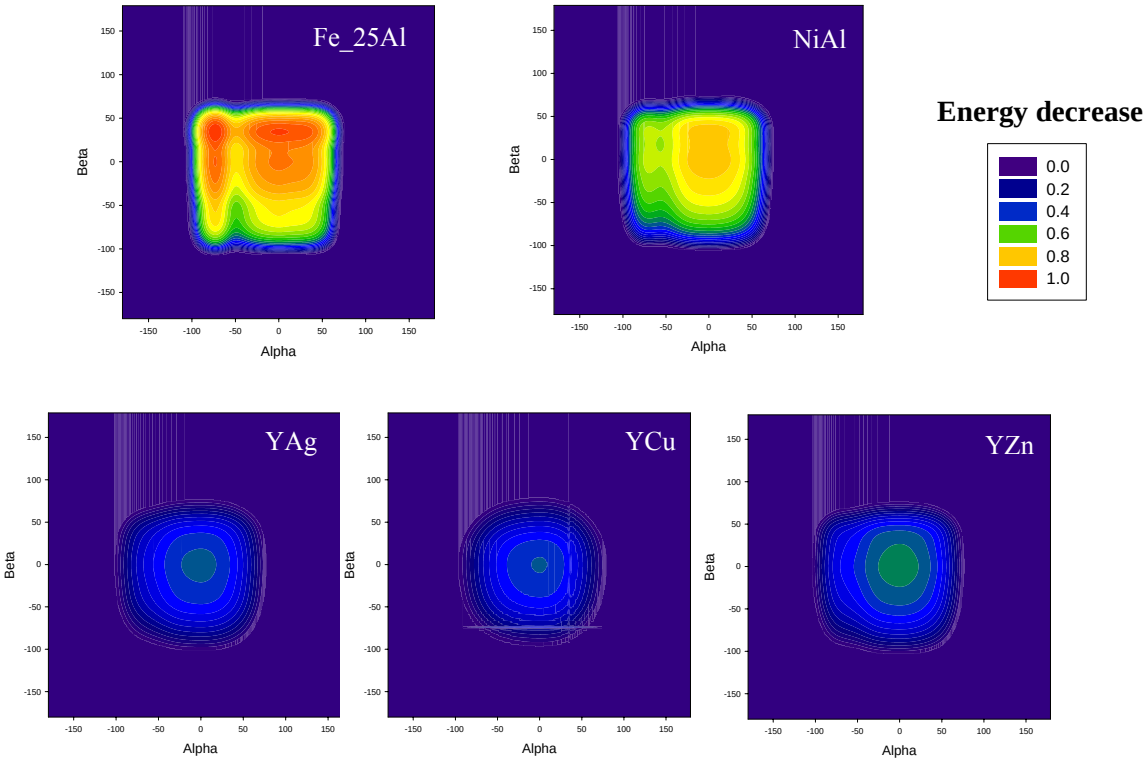

Figure 4.5 Contours of the energy decrease for the junction reactions ($[111](1\bar{1}0)\,\&\,[1\bar{1}\bar{1}](101)$).

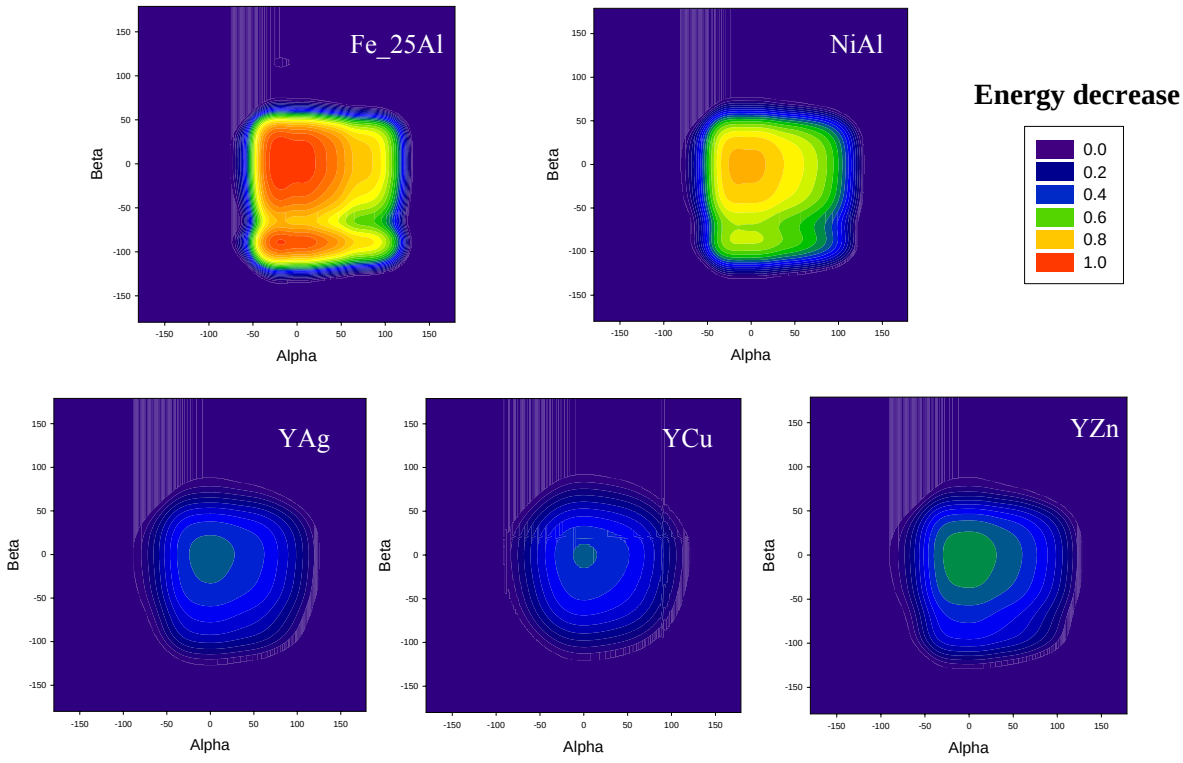

Figure 4.6 Contours of the energy decrease for the junction reactions ($[111](1\bar{1}0)\,\&\,[1\bar{1}\,\bar{1}](110)$).

applied stress and till dislocations were reached their equilibrium configurations. The equilibrium configurations of the junctions formed for these two different junction reactions, together with the slip systems $[111](1\bar{1}0)\&[1\bar{1}\bar{1}](211)$, of which the energy decrease contour is omitted here due to the similarity to the other ones, are shown in Figures 4.7-4.9.

Figure 4.7 shows the resulting junction configuration due to the $[111](1\bar{1}0)\&[1\bar{1}\bar{1}](101)$ slip systems. The initial angles between the dislocation arms and the intersection line $[\bar{1}\bar{1}1]$ were $\alpha = 35.26^{\circ}$ and $\beta = 54.74^{\circ}$, respectively, which were determined from the contour plots shown in Figure 4.5. The kink (zigzag) formation along the dislocation arms for Fe-25Al, due to the negative line tension discussed in Chapter 3, can be clearly depicted in Figure 4.7. On the other hand, for YCu, YZn, and YAg in the equilibrium configurations, the arms in the junctions are straight in agreement with the earlier line tension solutions (see Figure 3.2). Also, the evolution of much longer junction lengths in Fe-25Al and NiAl in comparison to ones that formed in YCu, YZn, and YAg can be clearly seen in the figure. The values of the junction lengths at the equilibrium are summarized in Table 4.1.

For the slip systems $[111](1\bar{1}0)\&[1\bar{1}\bar{1}](110)$ the equilibrium configuration of the junctions are shown in Figure 4.8. In these simulations, the initial angles between the dislocation arms and the intersection line [001] were both 54.73°, which were also in the range of angles to form junctions (Figure 4.6), but at the fringes of the contours.

Similarly, kinks (zigzags) also formed along the dislocation arms in Fe-25Al for this junction configuration as seen from the Figure. The resulting junction lengths formed in Fe-25Al and NiAl are 125 Å and 75 Å and they are much shorter than ones formed for the slip systems $[111](1\bar{1}0)\&[1\bar{1}\bar{1}](101)$. For the same initial configuration dislocations, there is no junction formation for YAg, YCu, and YZn as seen in Figure 4.8(b) and even the two dislocation arms were repulsive to each other. Although the contour plots of the energy decrease predict the possible junction formation in these three B2 alloys, there is no real junction reaction taking place due to the very small energy decrease and the resulting elastic interaction of dislocation arms.

For the slip systems $[111](1\bar{1}0)\&[1\bar{1}\,\bar{1}](211)$, the equilibrium junction configurations in these five intermetallics are summarized in Figure 4.9. The initial angles between the dislocation arms and the intersection line $[\bar{1}\,\bar{1}3]$ for these simulations were $\alpha = -25.23^{\circ}$ and $\beta = 31.48^{\circ}$. Likewise, kink (zigzag) formation along the dislocation arms in Fe-25Al is still noticeable. When a comparison is made with the results from two previous simulations, the junctions formed in $[111](1\bar{1}0)\&[1\bar{1}\,\bar{1}](211)$ have the largest lengths. For this case, under the effect of anisotropy, Fe-25Al is again for the longest junction, followed by NiAl, YZn, YAg, and YCu. The detailed values of the resulting junction lengths are summarized in Table 4.1.

(a)

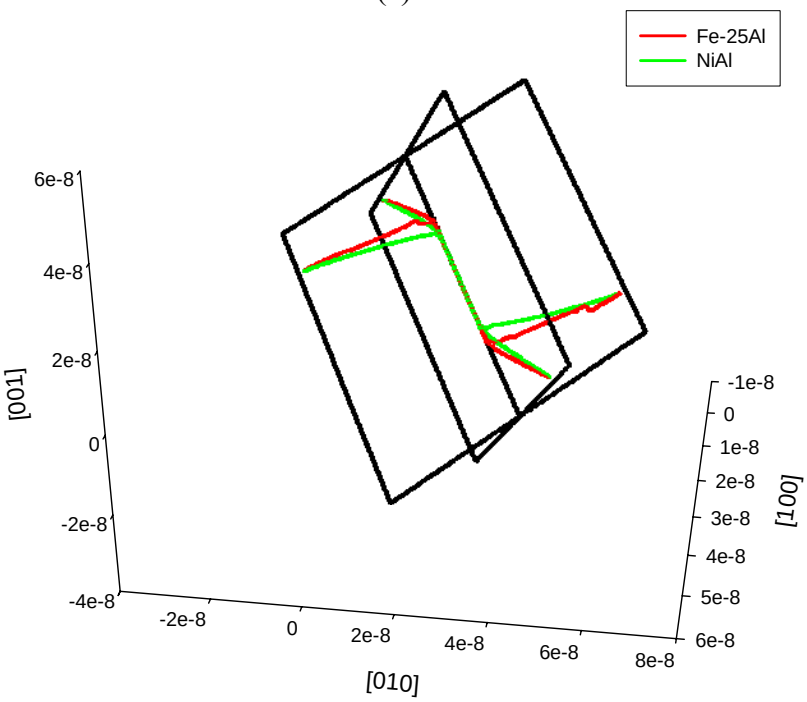

(b)

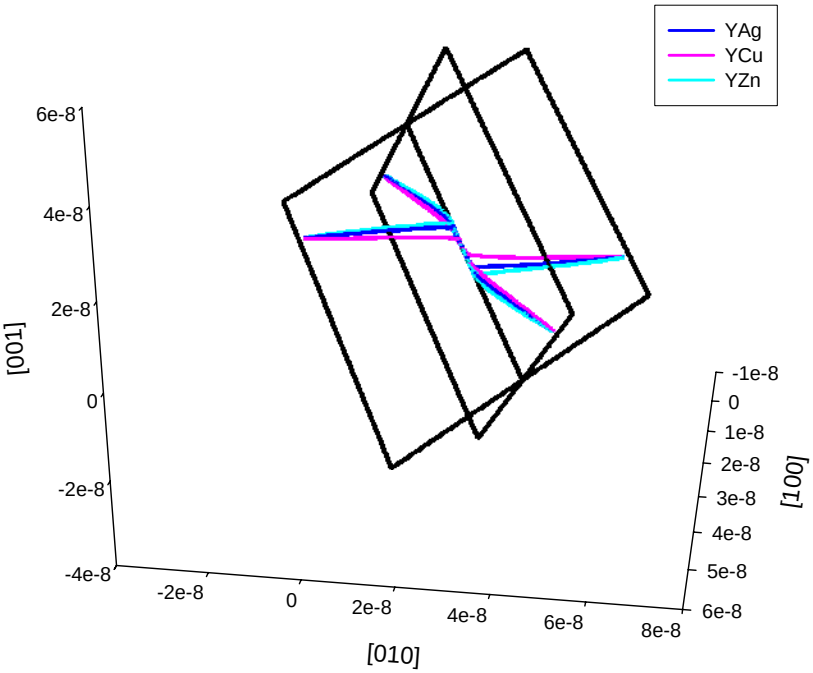

Figure 4.7 Junction configurations at an equilibrium status ($[111](1\bar{1}0)\,\&\,[1\bar{1}\bar{1}](101)$). (a) Fe-25Al and NiAl; (b) YAg, YCu, and YZn.

(a)

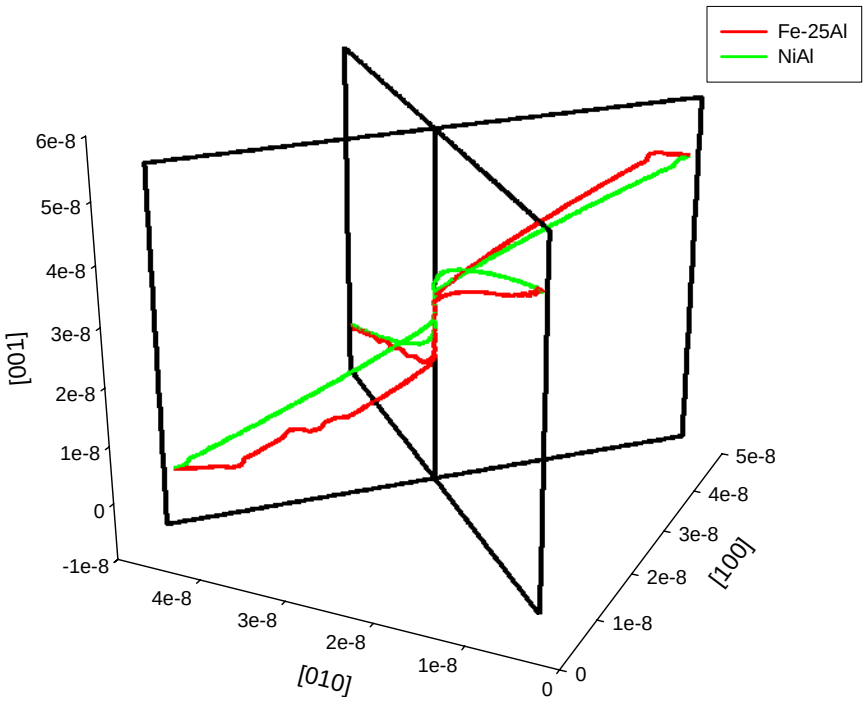

(b)

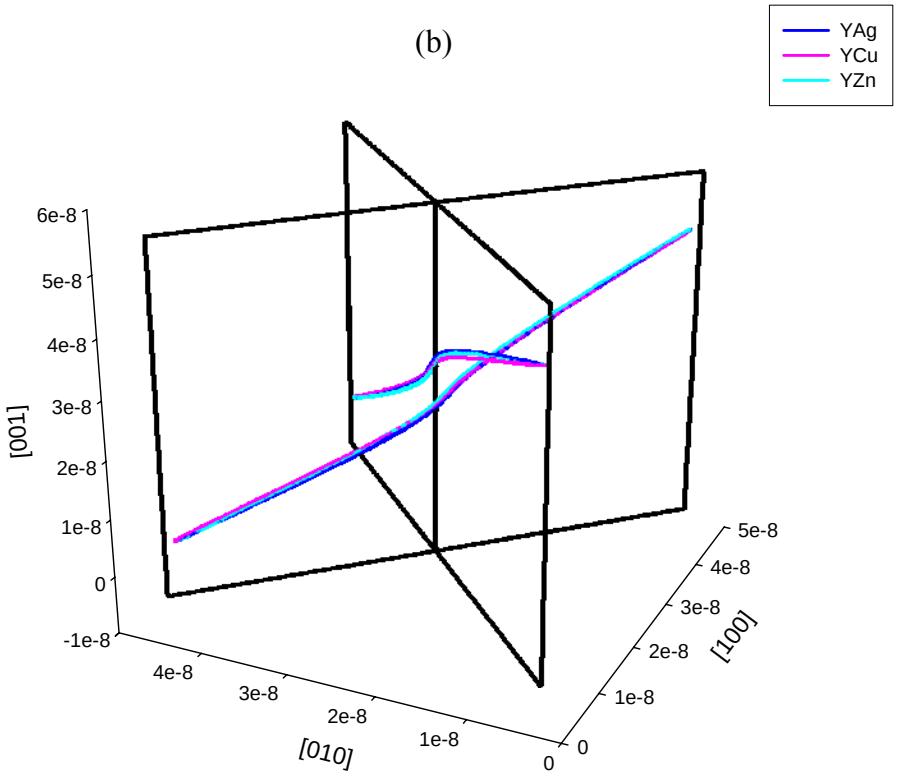

Figure 4.8 Junction configurations at an equilibrium status ($[111](1\bar{1}0)\,\&\,[1\bar{1}\,\bar{1}](110)$).
(a) Fe-25Al and NiAl; (b) YAg, YCu, and YZn.

(a)

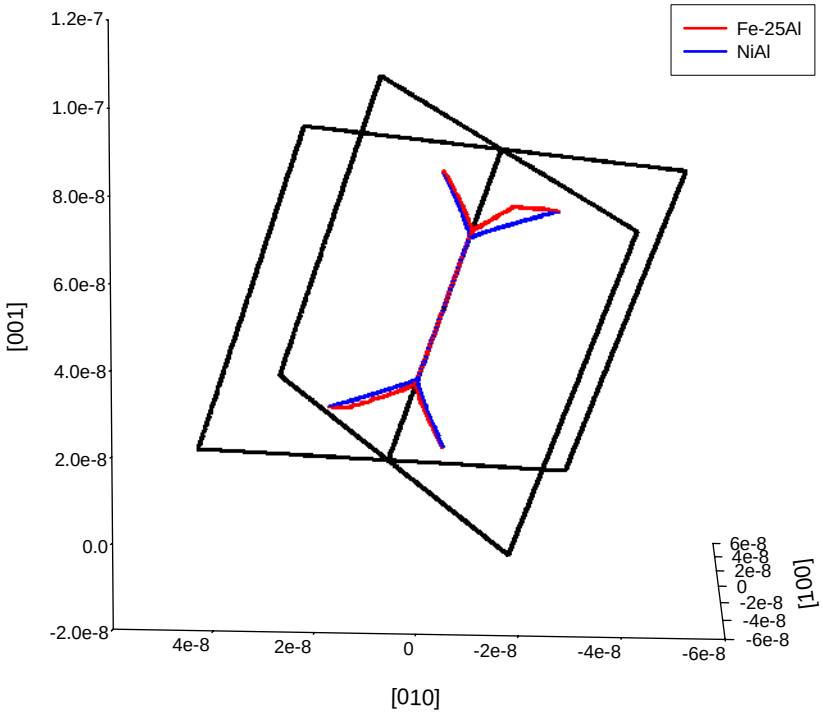

(b)

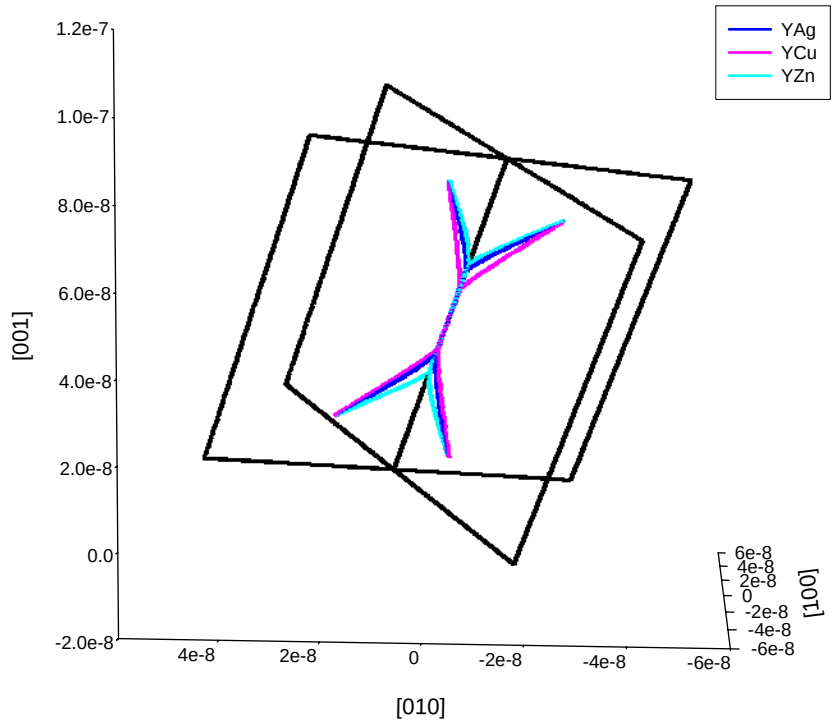

Figure 4.9 Junction configurations at an equilibrium status ($[111](1\bar{1}0)\,\&\,[1\bar{1}\bar{1}](211)$).
(a) Fe-25Al and NiAl; (b) YAg, YCu, and YZn.

In the following simulations, the breakup behavior of the junctions in Figures 4.7-4.9 was studied. The applied stress tensor was formed in such a way that the resulting resolved shear stresses in both slip planes were equal in magnitude and in sign. The critical breakup stress is defined when the junction length become zero during the course of the simulations. The time step used in this breaking process is 2.0e-14s. Starting from the equilibrium configuration, the evolution of the breakup process with increasing applied stress for the junctions formed in Fe-25Al and YCu with the slip systems $[111](1\bar{1}0)\&[1\bar{1}\,\bar{1}](211)$ is shown in Figure 4.10. As can be seen, the four remaining dislocation arms outside the junction increasingly bow out under the applied stress as if they are small F-R resources, and self-forces at their two ends also increase. Once the curvature at two ends reaches a critical value, the "pinning" point will be unstable and then move inward to reduce the junction length with the so-called unzipping process. As a result, the length of F-R resources increases, making the curvature near the "pinning" point even higher. So the destructive process can proceed spontaneously till the two dislocations separate apart each other totally. Of course, besides the level of the applied stress, the initial length of these four arms, the self-force originating from the line tension, and the forces originating from the interaction of the dislocation segments dictate the magnitude of the bow out. Again, due to the negative line tension, kinks formed along the dislocation arms in Fe-25Al can be seen clearly during the breakup process; however, for the same junction in YCu, the four dislocation arms are always smooth as seen in Figure 4.10(b). For the other junction configurations, the breakup process is similar to the unzipping mechanism seen in Fig 4.10.

The detailed critical resolved shear stress values to break the junctions in five intermetallic alloys are given in Table 4.1. It can be clearly seen that much higher applied stress is needed to break the junctions formed in Fe-25Al and NiAl ordinary intermetallics, compared to the values of stress for other three RM alloys, which also indicates the higher ductility of YCu, YAg, and YZn.

Table 4.1 Junction length (Å) and critical resolved shear stress (*MPa*).

	$[111](1\bar{1}0)\,\&\,[1\bar{1}\,\bar{1}](101)$		$[111](1\bar{1}0)\,\&\,[1\bar{1}\,\bar{1}](110)$		$[111](1\bar{1}0)\,\&\,[1\bar{1}\,\bar{1}](211)$	
	L_J	τ_{CRSS}	L_J	τ_{CRSS}	L_J	τ_{CRSS}
Fe-25Al	300	1461.84	125	618.72	462.5	1383.87
NiAl	237.5	1075.17	75	477.3	425	1318.90
YAg	125	632.46	*	*	262.5	831.62
YCu	62.5	442.72	*	*	200	786.14
YZn	137.5	679.89	*	*	325	922.58

***** No junction

4.4 Summary

In this Chapter, Frank-Read source evolution, dislocation dipole formation and breakup process, as well as dislocation junction formation and breakup procedure were studied by utilizing fully anisotropic 3D dislocation dynamics simulations. The results indicate:

- The dislocation emission from a given Frank-Read source takes place at much lower stress levels in rare-earth based intermetallics than the ones in NiAl and Fe-25Al, in agreement with the experimentally observed lower yield strength values for these alloys.
- For a given slip system, in general, there are smaller number of dislocation orientations that form junctions in rare-earth base intermetallics. These junctions are shorter in length and require lower stress levels to break up than the ones in NiAl and Fe-25Al.

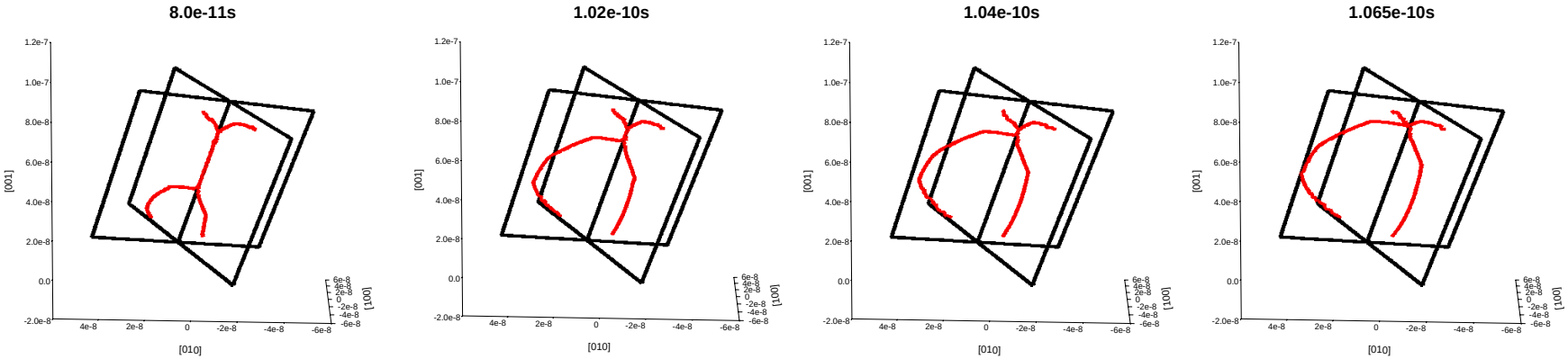

(a)

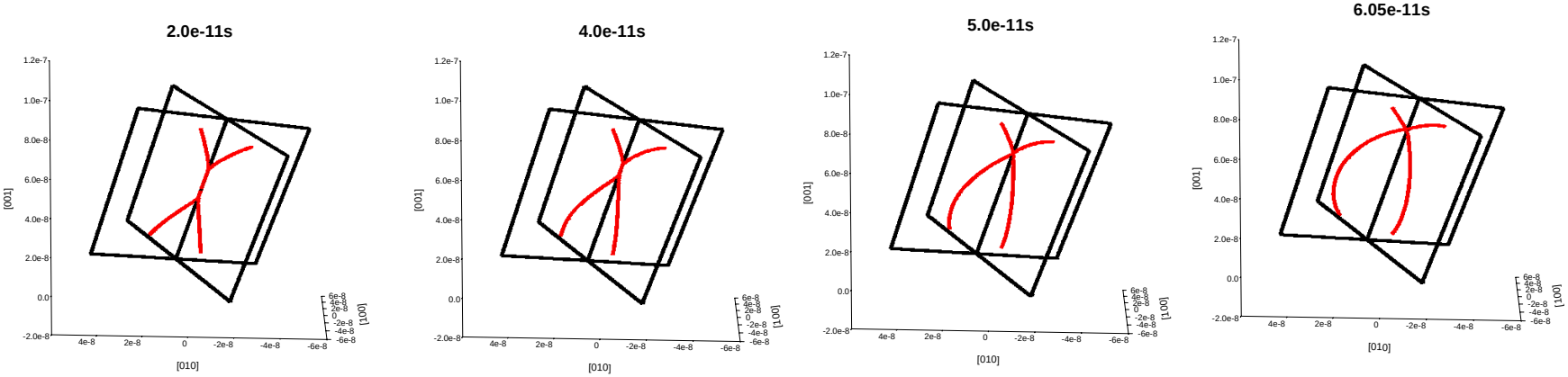

(b)

Figure 4.10 Junction breakup process in (a)Fe-25Al and (b)YCu with the slip systems $[111](1\bar{1}0)$ **&** $[1\bar{1}\bar{1}](211)$.

Reference

[1] Rhee, M., Zbib, H., and Hirth, J., 1998, *Mod. Sim. Mat. Sci. Engr*., **6,** 467.

[2] Huang, J. and Ghoniem, N., 2002, *Mod. Sim. Mat. Sci. Engr*.,**10**, 1.

[3] Bulatov, V., Abraham, F., Kubin L., Devincre B., and Yip S., 1998, *Nature*, **392**, 669.

[4] *W.Püschl* , 1985, *Phys. Stat. Sol. (a)*, **90**,181.

CHAPTER 5

SOLUTE AND DISLOCATION JUNCTION INTERACTIONS

In Chapter 4, the forming and breakup processes of junctions in five intermetallic compounds have been studied with anisotropic 3D dislocation dynamics. In this Chapter, first, the role of solute segregation on the strength and the evolution behavior of dislocation junctions is studied parametrically by utilizing kinetic Monte Carlo and 3D dislocation dynamics simulations in fcc crystal systems due to the high computational demand required for these simulations in case of elastic anisotropy. Later, the effects of elastic anisotropy on the behavior of solute segregation are elucidated.

Recently, other researchers also studied the formation and breakup strength of the junctions with molecular dynamics simulations [1], dislocation dynamics simulations [2,3] and simple line tension models [4,5]. These studies have indicated that, in fcc crystals, Lomer junctions have the highest strength, followed by glissile junctions and Hirth locks. On the other hand, solid solution hardening is one of the effective strengthening mechanisms for almost all alloy systems, resulting from the interactions between dislocations and solutes. Solutes act as point obstacles to moving dislocations at low temperatures or in the case of slow-diffusing solutes [6-11]. However, when solute diffusion is significant, the elastic interactions between solutes and dislocations lead to solute segregation around dislocations (Cottrell atmosphere [12]) and depletion elsewhere. Such a solute atmosphere can produce a large drag force on a mobile

dislocation; such interactions have been studied ranging from asymptotic solute distributions [13-17] to dynamical cases with kinetic Monte Carlo [18] and phase-field models [19]. Recently, the interaction of solutes with dislocation junctions has been shown to be a possible mechanism for dynamics strain aging and softening, leading to the Portevin–LeChatelier effect [5,20]. Also, solute friction resulted in a shielding of elastic interactions leading to significant decreases on junction strengths and annihilation reactions [21].

5.1 Computational procedures

To consider the effects of solutes on dislocation junctions, the Peach-Koehler formula (Eq. 2.2) was modified as

$$F = ((\sigma_{ij}^{D} + \sigma_{ij}^{A} + \sigma_{ij}^{S}) \bullet b) \times t + F_{self} \tag{5.1}$$

Here, the stress σ_{ij}^{S} from the solutes on the dislocations can be treated within the framework of elasticity by modeling the solutes as point sources of expansion for which [11]

$$\begin{aligned} \sigma_{rr}^{S} &= \sum_{1}^{n} -\frac{\mu}{\pi}\frac{\delta v}{r^3} \\ \sigma_{\theta\theta}^{S} &= \sigma_{\phi\phi}^{S} = \sum_{1}^{n} \frac{\mu}{\pi}\frac{\delta v}{r^3} \end{aligned} \tag{5.2}$$

where δv is the defect volume (the magnitude of the unconstrained volume dilatation due to one solute atom in the lattice); μ is the shear modulus; r is the distance between the position of a point defect and a field point on the dislocation line; and n is the number of point defects (solutes) in the system.

Likewise, once the components of the Peach-Koehler force, including the contribution of the solutes, for each segment are determined, Eq. 2.25 was used to obtain the velocities of the nodal points on the dislocation lines. Then the positions of the dislocations were updated and the dislocation reactions based on the constitutive rules were carried out.

The evolution of solute configuration during the simulations was realized through a kinetic Monte Carlo algorithm. For this purpose, the algorithm used in this study is in the form of the N-fold way or Bortz-Kalos-Lebowitz (BKL) method [22]. It is based on a 3D lattice. Initially, all solute atoms are distributed randomly in this 3D lattice. All solute migration events to nearest-neighbor positions are accounted for. Computational efficiency is achieved by constructing and maintaining a neighbor list. The rate of migration is given by an Arrhenius expression:

$$rate = \nu_0 e^{-(E_m + \delta E_{el})/k_B T} \tag{5.3}$$

where ν_0 is a prefactor related to vibration frequency; E_m is the energy of migration between lattices; and δE_{el} is the solute-stress field interaction energy change between neighboring lattices. At each Monte Carlo step, the probability of a given event being selected is determined by the ratio of its rate in the total rates sum, and the time increment dt is computed as

$$dt = -\frac{\ln(\xi)}{R_t} \tag{5.4}$$

where ξ is a random number in the interval (0,1) and R_t is the total rates sum. Mutual interactions among the solutes are ignored owing to the very low global concentration (percentage of occupied lattice sites).

In this study, single Lomer junctions with slip systems $1/2[10\bar{1}](\bar{1}\,\bar{1}\,\bar{1})$ & $1/2[011](11\bar{1})$, in fcc crystals were considered. The dislocations were given an initial length of 150|b| (where |b| is the magnitude of the Burgers vector) and were composed of linear segments 5|b| in length. The values of various material parameters appearing in Eqs. 5.1-5.4 and used during the course of simulations are summarized in Tables 5.1 and 5.2. For all cases, the equilibrium configurations of the junctions were achieved first under zero applied stress. Later, to break the junctions, the applied stress tensor in Eq. 5.1 was formed in such a way that the resulting resolved shear stresses in both slip planes were equal in magnitude but opposite in sign. The critical breakup stress was defined when the junction length became zero during the course of the simulations.

Table 5.1 Materials parameters used in 3D dislocation dynamics.

applied stress every DD step	0.02 MPa along [001] axis
time every DD step	2.5e-15---1.0e-12 s
resistivity	1.0e-4---1.0e-2 Pa·s
cut-off distance used in σ^D calculation	2|b|

Table 5.2 Materials parameters used in Kinetic Monte Carlo.

defect volume*	-11.0 $Å^3$
vibrational frequency	5.0e13 s^{-1} (5.0e12 s^{-1} used in Figure 5.1(a))
migration energy	0.4 ev
temperature	600 K

Table 5.2 (continued)

global solute concentration	0.015%---0.3%
cut-off distance used in σ^S calculation	1|b|

* The cases with figures designated the certain value of defect volume are excluded. Also, the defect volume used in Figure 5.7(a) is -5.6 $Å^3$ and all the results of resolved shear stress are normalized by the shear modulus.

5.2 Results and Discussions

In the first set of the simulations, the role of orientation of dislocations on the evolution and the breakup of Lomer junctions, in the absence of solutes, was considered. For $1/2[10\bar{1}](\bar{1}\,\bar{1}\,\bar{1})$ & $1/2[011](11\bar{1})$ slip systems, the possible initial angles (i.e., the angles between the dislocation lines and the intersection line of the two slip planes) of the dislocations that form a Lomer junction have been given in ref [3]. At the beginning of the simulations, two straight dislocations of equal length, intersecting each other at their midpoints and making equal angles with the intersection line of the two slip planes, were placed together. Both dislocations were also pinned at their end points during the course of the simulations. The equilibrium configurations of this junction system for the initial angles 30º, 45º, and 60º are shown in Figure 5.1 (top). As can be seen, due to the interaction of their stress-fields, two straight dislocations react and form a junction along the intersection of the slip planes. The resulting lengths of the junctions are almost inversely proportional to the initial angles and range from 85|b| to 20|b| with increasing initial angles. Starting from the equilibrium configuration, the evolution of the breakup process with the increasing applied stress for the Lomer junction formed with 30^o initial angles is shown in Figure 5.1 (bottom). As can be seen, the four remaining dislocation arms outside the junction increasingly bow out under the applied stress, leading to a

reduction in the junction length with the so-called unzipping process. Eventually, with the complete loss of junctions, the pinned dislocations expand further and become unstable once the resolved shear stress reaches a critical level. Of course, besides the level of the applied stress, the initial length of these four arms, the self-force originating from the line tension, and the forces originating from the interaction of the dislocation segments dictate the magnitude of the bow-out. The destruction mechanism seen in Figure 5.1 remained the same for all cases, unless shown otherwise. The magnitude of the breakup stress (as defined earlier) for these three Lomer junctions is summarized in Figure 5.2. In agreement with earlier studies [2,4], it is also observed that there is a linear increase in the breakup stress level with increasing junction lengths.

In the next set of simulations, the role of solute segregation on the strength of the preformed Lomer junctions was studied. A total of 500 solute atoms (0.015% global concentration) were randomly distributed into a $(150|b|)^3$ simulation cell containing the preformed junction configurations in its center. For these three junction configurations, the kinetics of segregation to a region within a 5|b| radius along the dislocation lines is shown in Figure 5.3(a). In the Figure, the total number of solutes within this 5|b| region along the dislocations is normalized by the overall number of solutes in the simulation cell. As can be seen, the rate of segregation is initially high, as a result of the very large number of empty sites near the dislocation lines. The rate of segregation decreases with the time, due to the decrease in the number of available empty sites, and also due to the exhaustion of the highly mobile nearby solutes. As a result, the initial segregation behavior for all three junctions is similar. However, with the increasing time, more

segregation takes place for those junctions composed of dislocations having smaller initial angles. In order to explain this segregation behavior, the variation of the character index ($\cos(\alpha)$ where α is the angle between the Burgers vector and the line direction) of the dislocation segments in these junctions is shown in Figure 5.3(b). The solute segregation (Cottrell atmosphere) takes place in the tensile stress field region of a dislocation having an edge component. Therefore, in a junction configuration, more solutes would be segregated toward those segments approaching the edge character. As can be seen from Figure 5.3(b), the junctions formed along the intersection line have the pure edge character. Thus, more solutes can be segregated toward the junctions formed from the dislocations with 30° and 45° initial angles due to the longer junctions in length. Moreover, the dislocation segments on four arms seem to also have more edge character for the dislocations with 30° and 45° initial angles. The spatial distribution of the solutes for these three junction configurations after 0.156 μs of segregation time is also shown in Figure 5.1 (top). During the breakup processes, it is assumed that all the solutes remain immobile in their final configurations. The resulting breakup stress values of the junctions, with the displayed solute atmospheres, are again summarized in Figure 5.2. As can be seen, the increase in breakup strengths is not the same for all junctions, even though the solute segregations are not significantly different [Figure 5.1 (top) and 5.3(a)]. The solute segregation substantially diminishes the large effect of the junction configuration on the breakup, and the resulting strength values seen for all three junctions become comparable. The evolution of the stress-strain curves during the breakup process

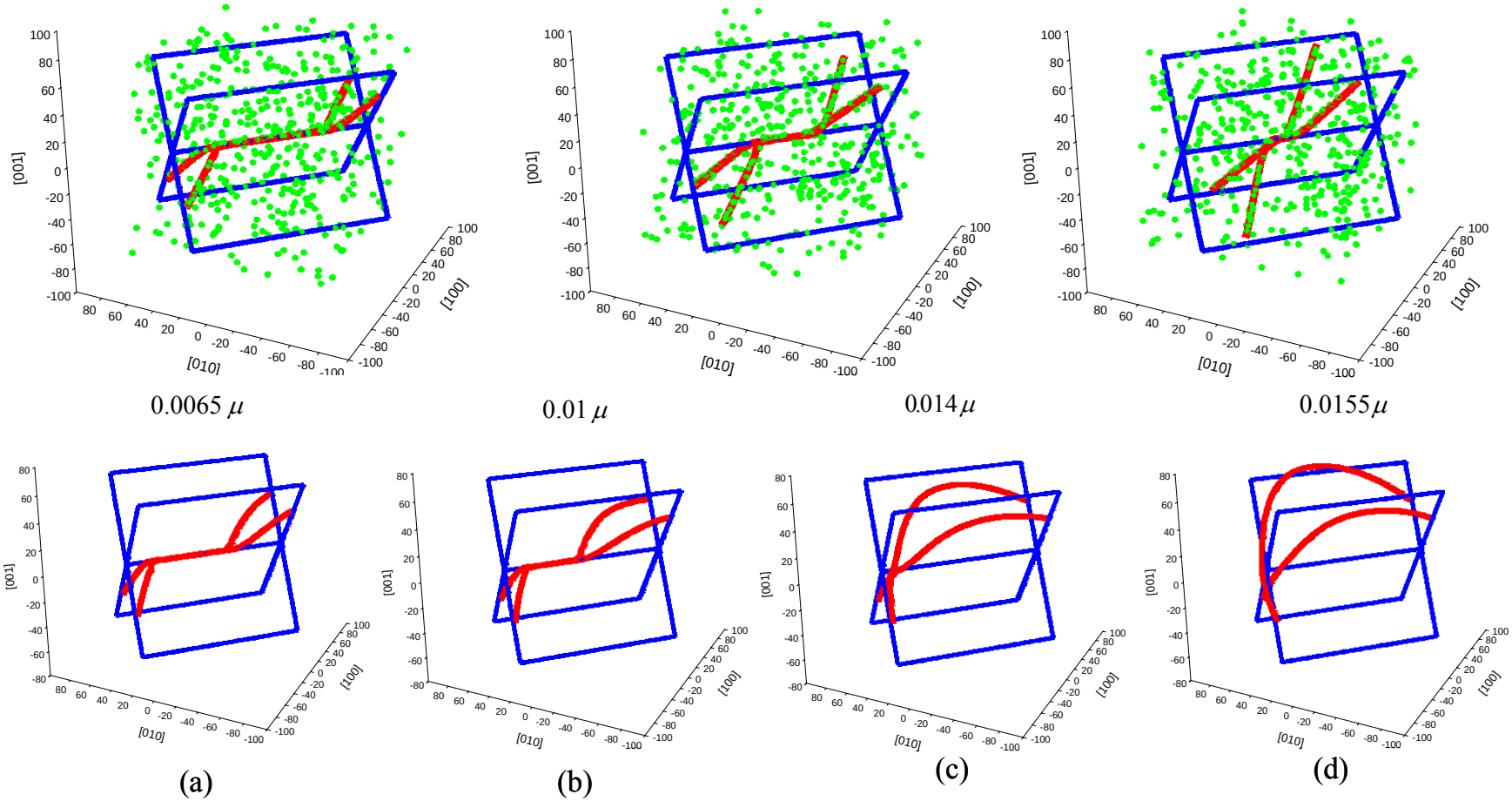

Figure 5.1 Top, equilibrium configurations of Lomer junctions starting with 30°, 45° and 60° initial angles of dislocations (red lines) and solute (green points) distribution after 0.156 μs segregation time. Bottom, breakup process of a Lomer junction formed with 30° initial angles in the absence of solutes.

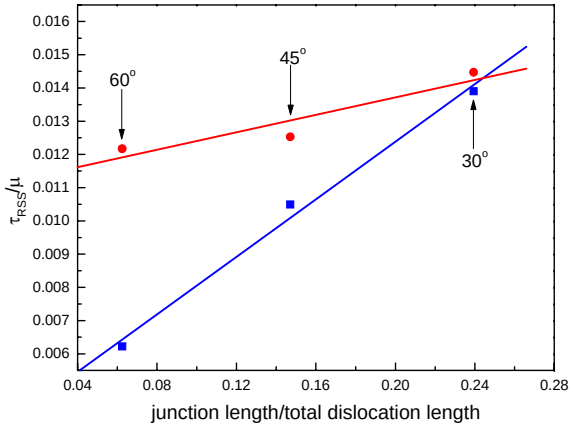

Figure 5.2 Correlation of breakup stress values of junctions formed with 30°, 45° and 60° initial angles with junction lengths for cases with solutes (round symbols) and without solutes (square symbols).

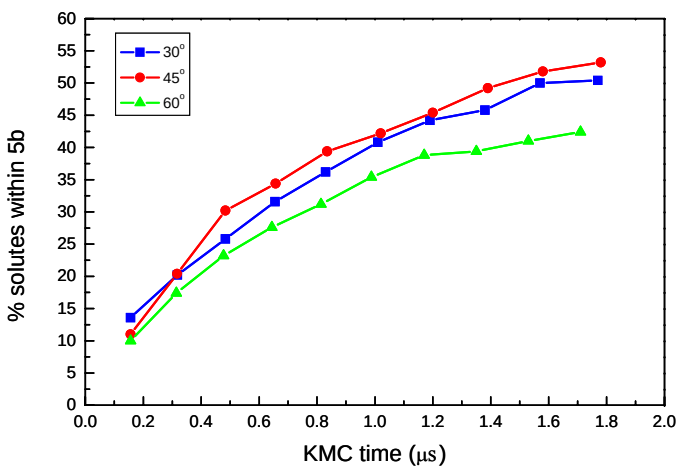

(a)

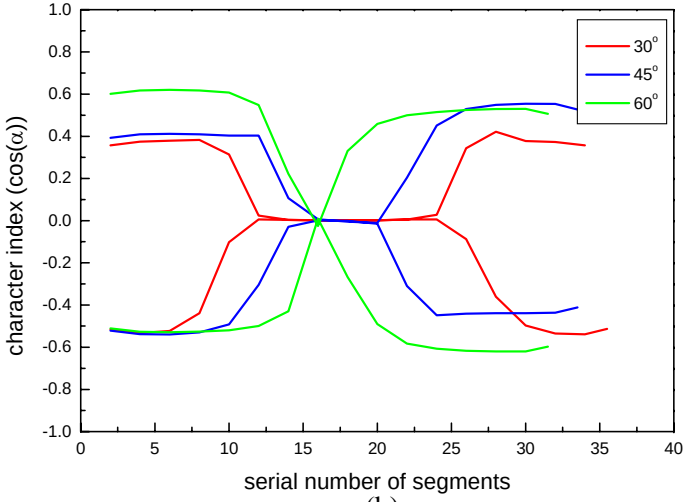

(b)

Figure 5.3 (a) Solute segregation kinetics to junctions formed with 30°, 45° and 60° initial angles; (b) variation of the character index of the dislocation segments in junctions formed with 30°, 45° and 60° initial angles.

with and without the solutes is shown in Figure 5.4 for only the junctions with 30° and 60° initial angles, for the sake of clarity of the figure. The arrows on the stress-strain curves correspond to the junction configurations shown in Figure 5.1 (bottom) during the breakup process. It is possible to divide the stress-strain curve into two regions. The first region, in which the rate of increase in the stress values is high, is associated with the bowing of the junction arms to a critical configuration. This is followed by a second region in which the junction unzips without requiring similar stress elevation. Hardening of the junctions due to the solute segregation is clearly identifiable in the figure. For these cases, the abrupt increases in the stress values reflect the breakup of the dislocation segments from the solutes (overcoming the solute drag).

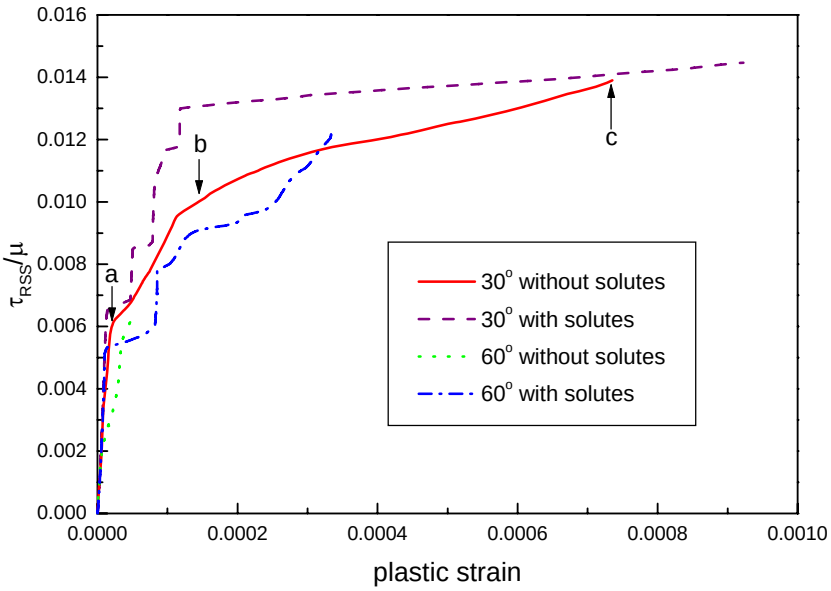

Figure 5.4 Resulting stress-plastic strain curves during the breakup process of junctions formed with 30° and 60° initial angles for cases with and without solutes.

Next, the parameters that are associated with the solutes and influence both the evolution and the strength of the junctions will be elucidated. There are only two parameters. The first is the defect volume δv appearing in Eq. 5.2, which sets the amplitude of the interaction stress with the dislocations as a function of the separation distance. And the second is the concentration of the solutes, which is expressed here as the number of solutes that are within a 5|b| radius of the dislocation lines rather than the global concentration. This choice is assumed to be reasonable when considering a very weak stress singularity $(1/r^3)$ associated with the solutes as shown in Eq. 5.2. In order to parameterize these two variables, the preformed equilibrium configuration of a Lomer junction formed from the dislocations having 30° initial angles (Figure 5.1) was utilized. Again, during the breakup process the solutes remained immobile. The resulting breakup stress values from these sets of simulations are summarized in Figure 5.5. As can be seen from Figure 5.5(a), in order to observe a reasonable increase in the junction strength, for a given δv, it appears that a critical local solute concentration is required. As expected, the junction strength gradually increases as more solutes are segregated along the dislocation lines. But the rate of this increase slows down to a limiting value, owing to the diminished effect of later segregated solutes, which have to be segregated relatively further away from the dislocation lines as a result of the exhaustion of available segregation sites. On the other hand, within this effective local solute concentration range, the strength of the junction increases linearly with the defect volume δv, as seen in Figure 5.5(b).

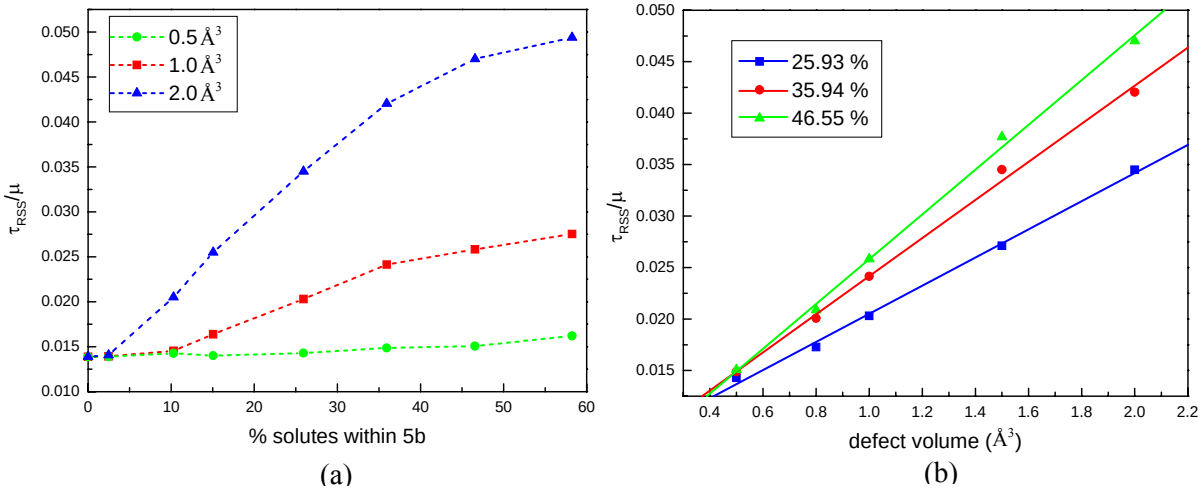

Figure 5.5 Variation of the breakup stress values for a junction formed with 30° initial angles with different local solute concentration and defect volume values. (a) As a function of local solute concentration; (b) as a function of defect volume δv .

In this section, the effects of the solute segregation on the evolution of the junction configurations and the resulting junction strengths are elucidated for two types of solute mobility and for different δv values. These simulations were performed for the junction with 30° initial angles, and it is assumed that the $1/2[10\bar{1}](\bar{1}\,\bar{1}\,\bar{1})$ dislocation is the forest dislocation. Initially, the fixed number of solutes randomly distributed into the simulation cell was allowed to segregate to this forest arm up to a certain local concentration with the kMC simulations. Then, the mobile arm of the junction, the $1/2[011](11\bar{1})$ dislocation, was introduced to interact with the forest dislocation having segregated solutes. For the first case it is assumed that, after the initial segregation, the mobility of the solutes relative to the mobility of the dislocations is considerably slow; so that the solutes remain effectively immobile during the junction formation and breakup processes. The equilibrium junction configurations for different local solute concentrations for the same Lomer junction with 30° initial angle are shown in Figure 5.6.

As can be seen, at low local solute concentrations, the forest dislocation was able to free itself from the solute cloud and to form the junctions in lengths comparable to those seen without the solutes. With the increasing local solute concentration, this breakaway from the solute cloud took place only around the central portion of the forest dislocation where two dislocations meet, and also where the interaction region between the two dislocations is strongest (Figure 5.6(c)). For large local solute concentrations, the forest dislocation remained virtually straight even though the mobile dislocation changed its initial shape due to the forces originating from the forest dislocation; however, the resulting junction was essentially in a so-called cross-state. For the junction configurations shown in Figure 5.6, the resulting breakup stress values are correlated with the junction lengths as a function of the local solute concentrations in Figure 5.7(a). Since the applied stress tensor yielded the equal magnitude of the resolved shear stress in the both planes, it is observed that there is an initial increase in the breakup stress even though the junction lengths are decreasing with the increasing local solute concentration. This is mainly due to the considerable reduction in the arm lengths of the forest dislocation as seen earlier in Figure 5.6. At high local solute concentration levels, where the junction configurations are at or near cross-state, there is a large drop in the breakup stress levels. For these cases the forest arm of the dislocation remained almost inactive and did not participate in the breakup process due to the solute cloud. However, for the junctions only evolving to the cross-state (or with very small junction lengths), their breakup strength also strongly depends upon the value of the defect volume δv of the solutes, as shown in Figure 5.7(b). With the increasing defect volume δv of the solutes segregated to the forest arm, the breakup stress value of these cross-state junctions starts to increase again. In order to

elucidate the resulting limiting behavior, the δv values were increased beyond normal values (up to 100 Å) in some of the simulations. As can be seen, the strength of the junction eventually approaches a limiting value. The reason for this behavior is the change in the junction failure mechanism. For these cases, instead of the usual unzipping process seen in all other cases (Figure 5.1(bottom)), the mobile arm of the junction gradually evolved into two smaller dislocation arcs due to the increasing constraint in the center, resulting from the increasing δv, as shown in Figure 5.8. Of course, these two smaller dislocation arcs require much larger resolved shear stress values to operate. The complete failure of the junction takes place when the bowing sections of this dislocation arm meet and annihilate each other. Therefore, once this effective pinning of the center portion of the mobile dislocation is reached, this failure mechanism remains the same, leading to constant strengthening behavior with the further increase in the defect volume δv.

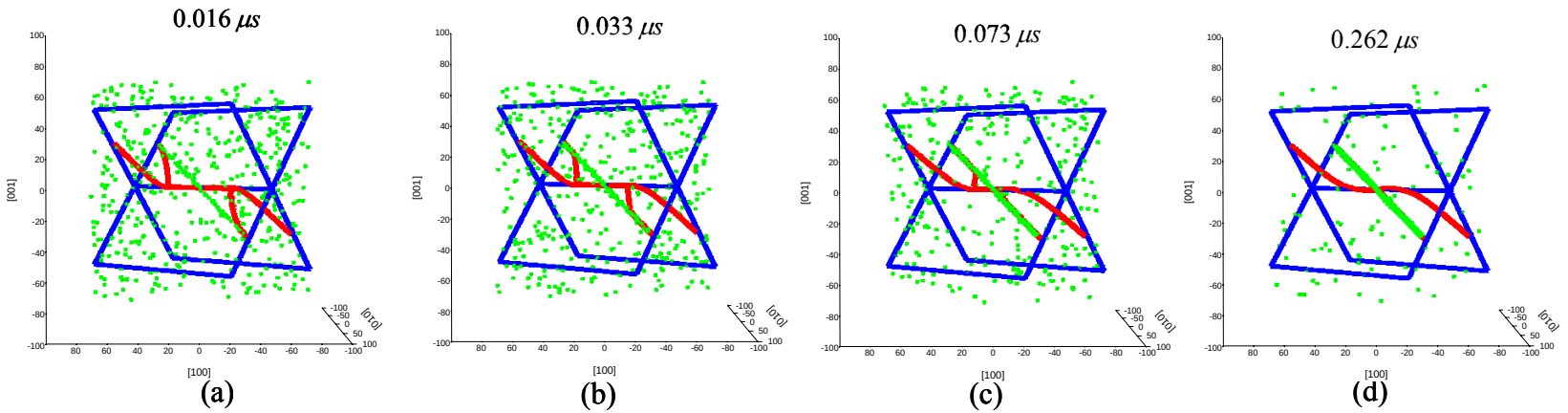

Figure 5.6 Evolution of a junction with 30° initial angles after different solute segregations to its $1/2[10\bar{1}](\bar{1}\ \bar{1}\ \bar{1})$ forest dislocation arm. The red lines represent dislocation configurations and green points represent the spatial distribution of solutes after indicated segregation times.

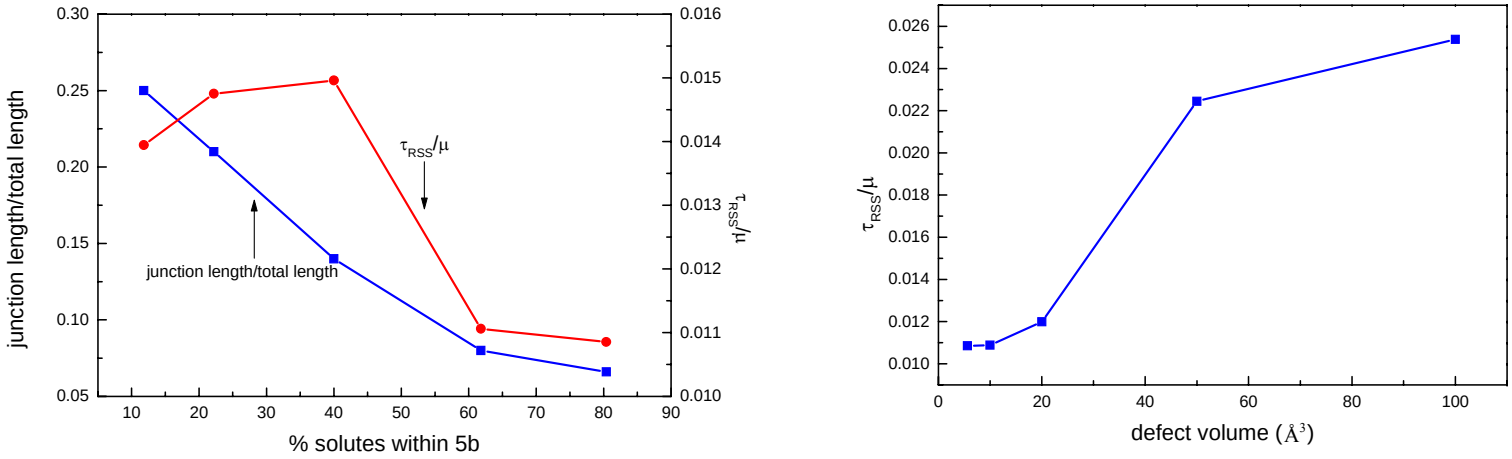

Figure 5.7 Variation of the breakup stress values for a junction formed with 30° initial angles with different local solute concentration and defect volume values. (a) As a function of local solute concentration; (b) as a function of defect volume δv for 80% local solute concentration.

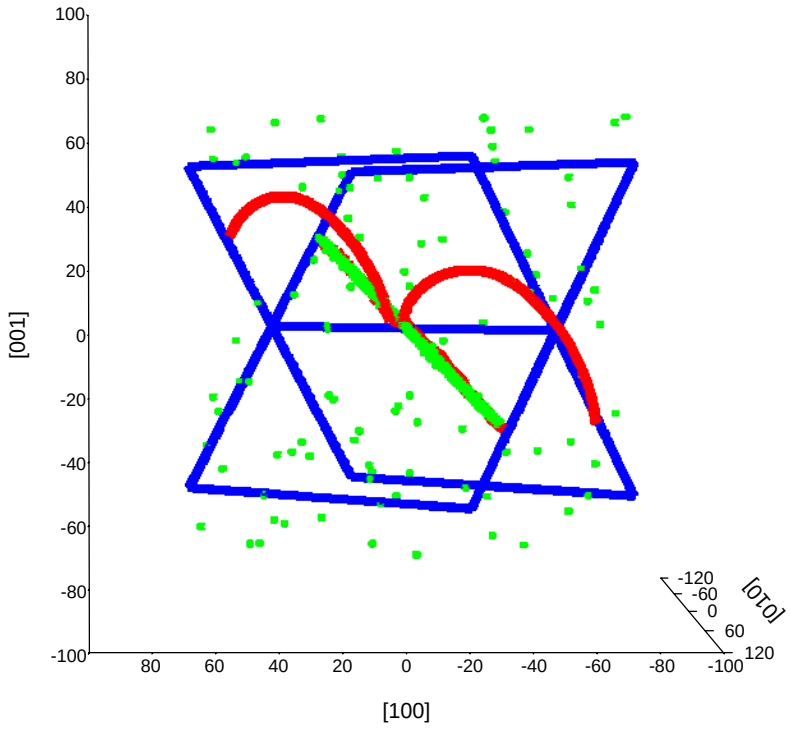

Figure 5.8 Changes in the breakup configuration of a junction formed with 30° initial angles, starting from the cross-state, due to very large value of defect volume δv .

In the next set of simulations, after the initial segregation to the forest dislocation arm, the solutes remained mobile during the junction formation and the following breakup processes. The resulting equilibrium junction configuration for this case is shown in Figure 5.9(a). The corresponding equilibrium junction configuration in the case of immobile solutes (same as Figure 5.6(d)) is also shown here for comparison. Although the starting conditions were the same as in the immobile solutes case, the forest arm was able to participate in the junction reaction, and a junction 40|b| in length was able to form as a result of the rearrangement of solutes due to the perturbation created by the stress field of the incoming mobile dislocation. The evolution of both the junction

configuration and the solute segregation patterns during the following breakup process is shown in Figure 5.9(b). A continuous rearrangement of solutes near the junction lines is clearly evident from the figure. The time evolution of this solute rearrangement, for both arms of the junction, is shown in Figure 5.10(a). As can be seen, during the breakup process, the number of solutes segregated along the $1/2[10\bar{1}](\bar{1}\,\bar{1}\,\bar{1})$ dislocation decreases, but the trend reverses for the$1/2[011](11\bar{1})$ dislocation. To further elucidate this behavior, the initial and the final character index ($\cos(\alpha)$) of the dislocation segments are shown in Figures 5.10(b) and 5.10(c). As can be seen, most of the segments in the $1/2[10\bar{1}](\bar{1}\,\bar{1}\,\bar{1})$ dislocation deviated from near edge character towards screw character during the breakup process. In contrast, for the $1/2[011](11\bar{1})$ dislocation, while the segments along one side of the junction also acquired more screw character, the segments along the other side approached nearly pure edge character, resulting in preferential variations in the local solute concentrations seen in Figures 5.9(b) and 5.10(a). For the mobile case, the breakup stress is about twice the value it has for the case where the solutes remain immobile after the initial segregation to the forest arm (0.022μ versus 0.011 μ), even though all the parameters are identical for these two cases.

The kMC algorithm used for solute movement and segregation in the simulations is based on only lattice (bulk) diffusion. There is still considerable debate on the role of pipe diffusion on the segregation of solutes to dislocations.

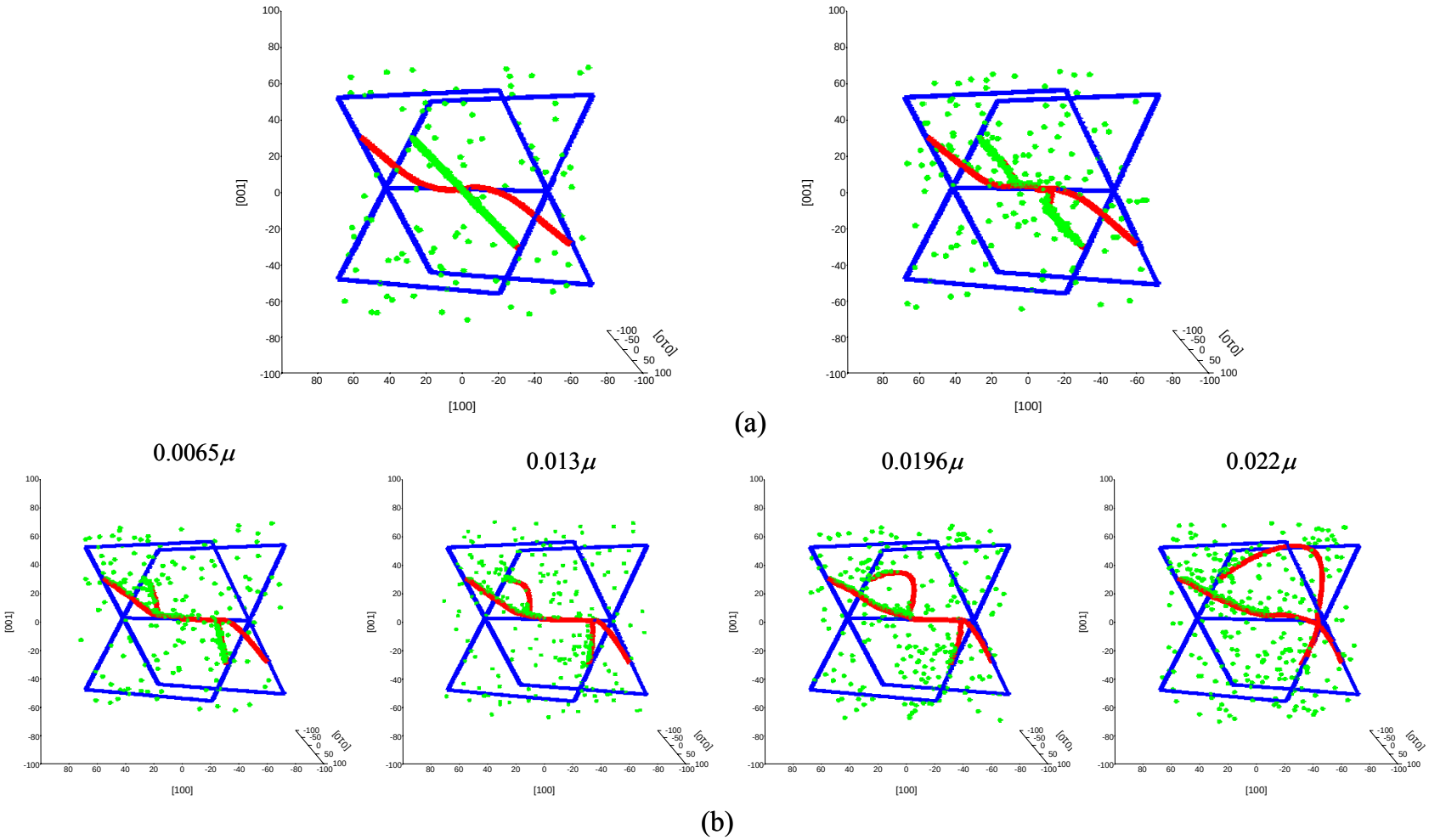

Figure 5.9 Top, equilibrium configurations of a junction formed with 30° initial angles after 0.262 μs solute segregation time to its $1/2[10\bar{1}](\bar{1}\,\bar{1}\,\bar{1})$ forest dislocation arm for cases with immobile (left) and mobile (right) solutes. Bottom, following breakup process of a corresponding junction with mobile solutes.

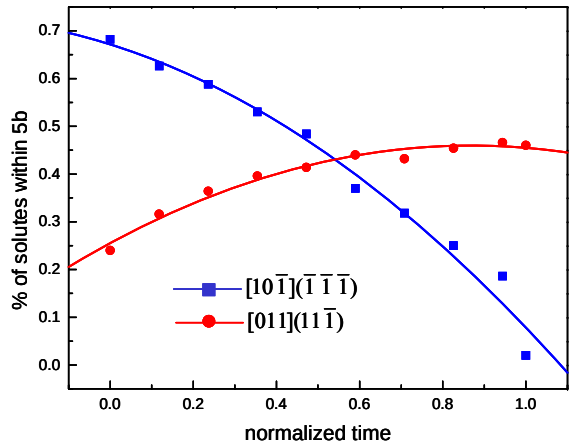

(a)

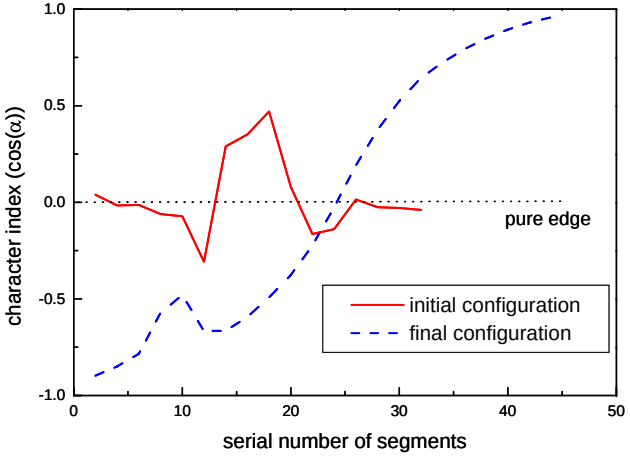

(b)

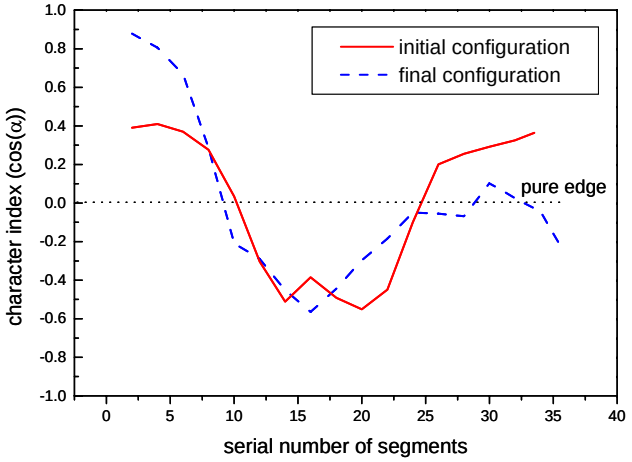

(c)

Figure 5.10 (a) Solute kinetics during the breakup process of a junction formed with 30° initial angles; (b) and (c) variation of the character index of the dislocation segments during the breakup process of a 30° junction.

Calorimetric studies of the kinetics of solute segregation [23] show that pipe diffusion dominates the very early stages of the segregation process, due to lower activation energy and free volume [20,24], followed by bulk diffusion; presumably, this is owing to the depletion of available vacancy sites [20]. The simulations presented in this study clearly show the profound effect of solutes both on the preexisting junctions and on the evolution of the junctions. In the simulations, the interaction of solutes with the dislocations was characterized with two parameters, the defect volume δv and the solute concentration. δv is assumed to be an intrinsic property for a given solute and the host crystal. On the other hand, the solute concentration, usually expressed as a global quantity, can be controlled more easily. However, it appears that its local measure in the surrounding region of the dislocations is somewhat more relevant owing to the short-range stress fields of the solutes as shown in Eq. 5.2. The local solute concentration definitely shows two opposing effects, depending upon the dynamics, in which both cases are plausible during the course of plastic deformation or in a service environment. If the solute segregation takes place on the preformed junctions, it was clearly seen that there is an increase in the strength of the junctions to a limiting value with increasing local solute concentration (Figure 5.5(a)). On the other hand, for the identical junction and solute parameters, if the solute segregation takes place on the forest arm of the dislocation first, before the junction formation, the significant reduction in the junction strength with the increasing local solute concentration was observed (Figure 5.7(a)). If the nature of the solutes or the loading rates permit further mobility of solutes after initial segregation to the forest arm, the rearrangement of local solute concentration during the destruction can

easily alter the strengthening behavior again as seen in Figures 5.9 and 5.10. The nature of solutes, defect volume δv, is of course definitely a factor in determining the ranges of the local solute concentration pertaining to this discussion, as seen in Figures 5.5(a) and 5.7(b). It is conceivable that (at least theoretically) for an extremely large value of δv, even a few solute atoms may lead to the different breakup process of the junctions as seen in Figure 5.8.

All the simulations presented in this study were carried out with the applied stress tensor that created resolved shear stresses in the slip planes that were equal in magnitude but opposite in sign. It is worth mentioning that for other applied stress configurations, it was observed that the effects of the solutes were either further amplified or mitigated as compared with the ones shown here. Of course, this is partially associated with the well-known asymmetry in the breakup behavior of the junctions [2,4] and partially associated with the dynamical effects seen here.

Finally, the effects of solutes on the behavior of junctions have been previously studied within the framework of the much simpler and less computationally demanding line tension model [5,21]. The effects of the solutes were introduced as a simple binding energy per dislocation line into the model in ref. [5]. In contrast, the role of solutes was included as the friction stress, affecting the overall mobility of dislocations, into the same line tension model in ref. [21]. Although both approaches do not explicitly take account of the role of local solute concentration and the intrinsic properties of the solutes, surprisingly, their predictions are qualitatively in agreement with some of the cases seen

in this study. Of course, these simple models do not yield the fine details of the interactions between the solutes and the dislocations as seen here. However, if some of their parameters can be further calibrated or supplemented with the similar simulations undertaken in this study, they may lead to more efficient modeling efforts for the dislocation and solute interactions.

5.3 Effect of anisotropy on the behavior of solute segregation

As noted in Chapter 1, compared to normal pure metals, intermetallic compounds show attractive mechanical and physical properties; however, the very low plastic ductility at or near room temperature presented by most of intermetallics impedes their real application greatly. Extensive investigations have shown that moisture induced environmental embrittlement is the main reason for this low ductility. The kinetic steps of this embrittlement process include [25,26] surface absorption, interaction with active elements (Al in aluminide and Si in silicide) to generate atomic hydrogen and diffusion of dissolved hydrogen from the surface along grain boundaries to bulk, leading to brittle intergranular fracture. Moreover, as discussed in the preceding section, due to the Cottrell atmosphere, the hydrogen atoms may also segregate around the dislocations if the diffusion is significant. Thus, in order to study the effects of hydrogen atoms on the strength and evolution behavior of dislocation junctions formed in the five intermetallics aforementioned in the former Chapters, the factor of anisotropy was included in the simulation of this section to investigate the solute segregation behavior. Due to the demanding computational complexity, the real dynamic junction evolution and breakup process were not included in the study of this section; however, according to the results

from this section and the preceding section, the role of solute segregation under the anisotropic elasticity can be depicted qualitatively.

5.3.1 Pure anisotropy effect on the solute segregation

The junction formed in YCu with the slip systems $[111](1\bar{1}0)\,\&\,[1\bar{1}\bar{1}](211)$ (the pink lines in the Figure 4.9) and the Lomer junction with the slip systems $1/2[10\bar{1}](\bar{1}\,\bar{1}\,\bar{1})\,\&\,1/2[011](11\bar{1})$ for the initial angle 30º (Figure 5.1) were chosen to study the elastic anisotropy effect on the solute segregation. The material parameters used here were the same as the ones in Tables 5.1 and 5.2, except for the migration energy and temperature. Here they were equal to 0.1 ev and 300 K, respectively. In these simulations, the geometry of junctions was always the same; however, the elastic constants (i.e. c11, c12 and c44) were chosen such that the resulting anisotropic factors were equal to 1, 3 and 6. For these two junction configurations, the kinetics of solute segregation to a region within a 5|b| radius along the dislocation lines is shown in Figure 5.11. As can be seen, similar to Figure 5.2(a), the rate of segregation is initially high due to a large number of empty sites near the dislocation lines and then decreases with time as the number of available empty sites and the highly mobile nearby solutes both decrease gradually with time. This tendency seems to occur for all the anisotropy factors considered. Also, it can be clearly seen that more solutes are segregated along the dislocation lines with the higher anisotropy factor, and the amplitude of this variance of the segregation behavior decreases with the increasing anisotropy ratio. As seen in Figure 5.11(b), the solute segregation behavior in the case of A = 3 and A = 6 is very similar.

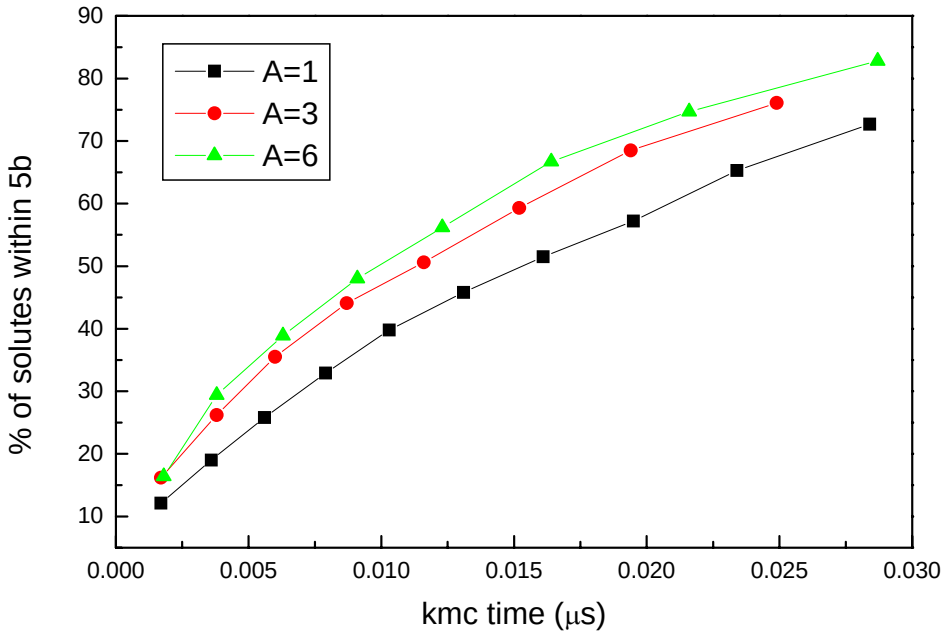

(a)

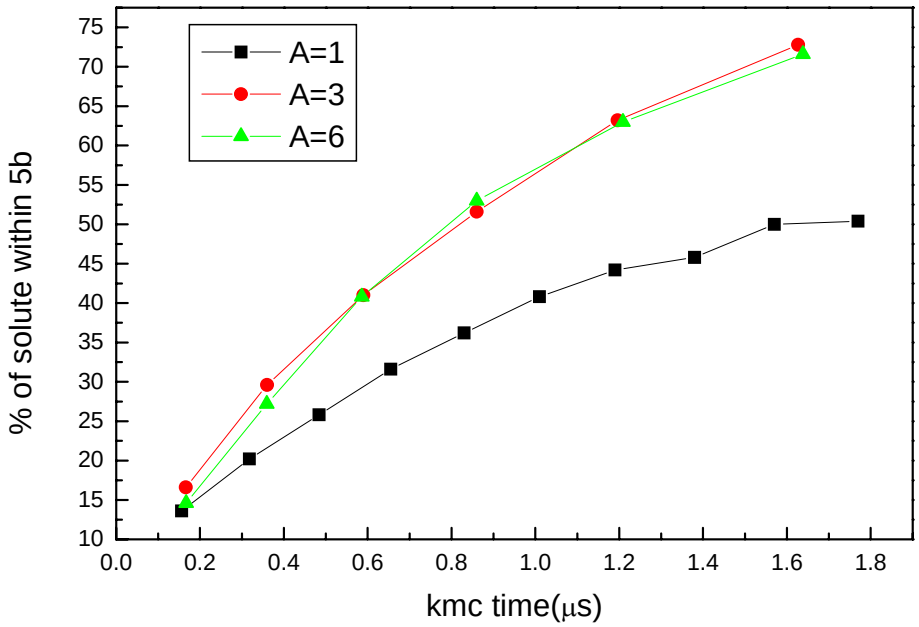

(b)

Figure 5.11 Solute segregation kinetics to junctions with the anisotropic factor A=1, 3 and 6. (a) Junction formed with the slip systems $[111](1\bar{1}0)\&[1\bar{1}\bar{1}](211)$; (b) junction formed with the slip systems $1/2[10\bar{1}](\bar{1}\bar{1}\bar{1})\&1/2[011](11\bar{1})$.

5.3.2 Solute segregation on the junctions formed in YCu, NiAl, and Fe-25Al with the slip systems $[111](1\bar{1}0)$ & $[1\bar{1}\bar{1}](211)$

As discussed in Chapter 4, higher anisotropy results in longer junction length and larger junction strength. In this section, for the junction configurations in these three alloys, the solute segregation behavior is elucidated by taking the fully elastic anisotropy effect. However, the migration energy of the solutes in all these three alloys was assumed to be the same. The plot of the local solute concentration vs. kMC time is shown in Figure 5.12. Again, the effect of elastic anisotropy on the solute segregation behavior can be seen clearly. In addition, the variation of character index (same meaning as that in Figure 5.2(b)) of the dislocation segments in these three junctions, and the resulting solute segregation patterns are summarized in Figure 5.13 (a)-(c). Since the junctions formed in these three intermetallics with the slip systems $[111](1\bar{1}0)\&[1\bar{1}\bar{1}](211)$ are always along the direction of the intersection line $[\bar{1}\bar{1}3]$, the character index for the junction part is same for all three alloys and much closer to the pure edge character. In addition, two arms on (211) slip plane are also more near edge character in YCu than the ones in NiAl and Fe-25Al. And the other two arms belonging to $(1\bar{1}0)$ slip plane are more screw characteristic in these three alloys. Therefore, with the increase of the junction length and the decrease of the length of the four arms, more mobile solutes are segregated toward the junction part, although the character index of the four arms changes to the one approaching the screw character.

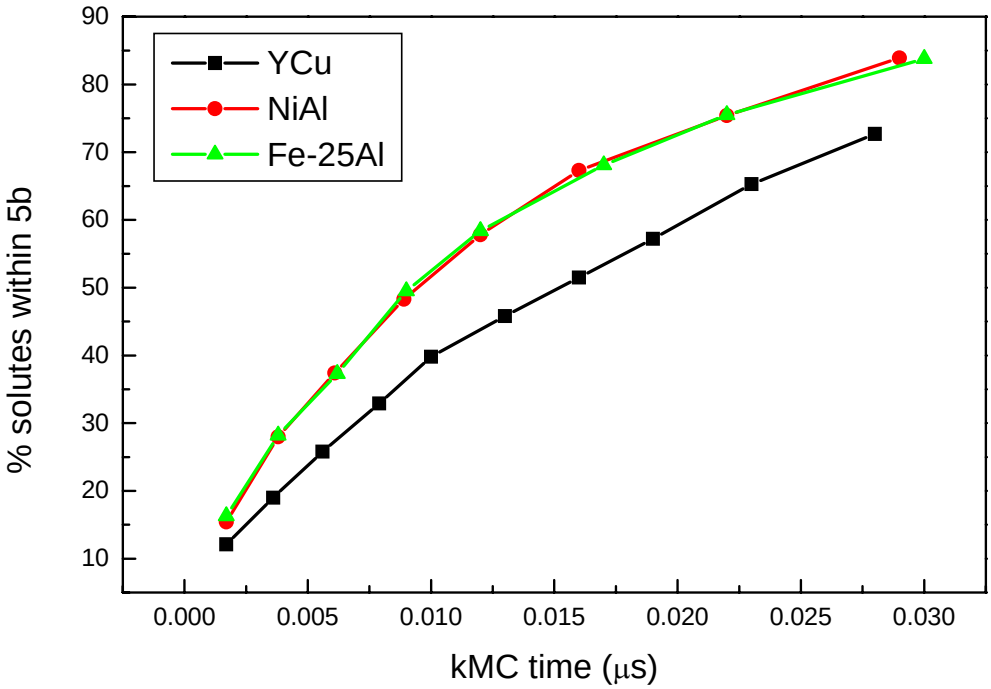

Figure 5.12 Solute segregation kinetics to junctions formed in YCu, NiAl, and Fe-25Al with the slip systems $[111](1\bar{1}0)\,\&\,[1\bar{1}\,\bar{1}](211)$.

Due to the high computational demand for the case of anisotropic solutions (about factor 10 in comparison to isotropic case), the simulations for the destruction of these junctions with segregated solute distributions were not performed. However, as discussed in the preceding section and shown in Figures 5.5(a) and 5.7(a), the local solute concentration clearly shows two opposing effects on the junction strength. If the solute segregation takes place on the preformed junctions, there is an increase in the strength of the junctions to a limiting value with the increasing local solute concentration (Figure 5.5(a)). On the other hand, for the identical junction and solute parameters, if the solute segregation takes place on the forest arm of the dislocation first, before the junction formation, the significant reductions in the junction strengths with the increasing local solute concentration can be observed due to the very short junction length (Figure 5.7(a)).

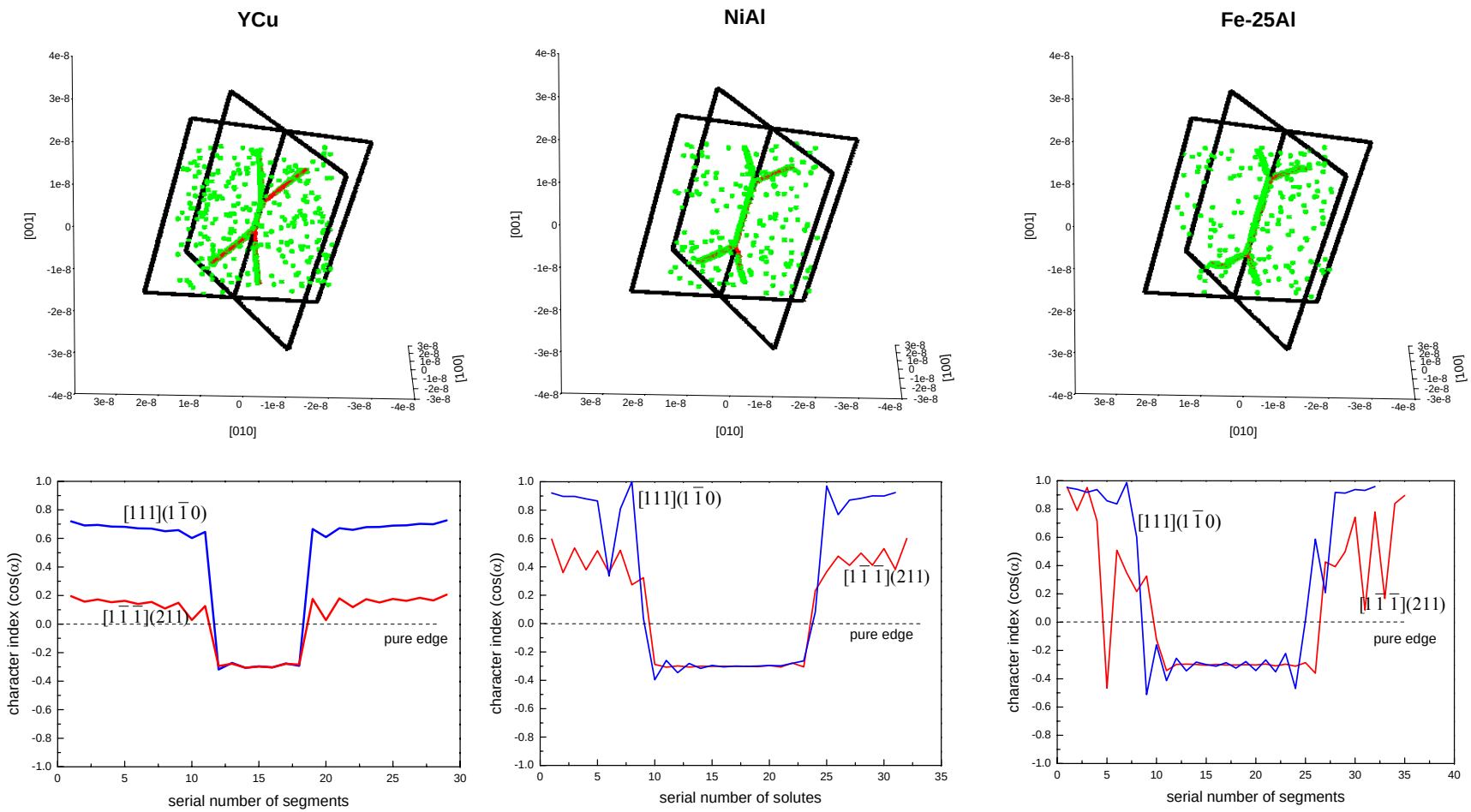

Figure 5.13 Junction configurations with the slip systems $[111](1\,\bar{1}\,0)\,\&\,[1\,\bar{1}\,\bar{1}](211)$ and the variation of the character index of the dislocation segments in corresponding junctions. (a) YCu; (b) NiAl; (c) Fe-25Al.

Therefore, it is expected that these two opposing effects will be further amplified with the increasing elastic anisotropy owing to the faster rate of solute segregation (Figures 5.11, 5.12, and 5.13). In these simulations, although the migration energy of the solutes in these three intermetallics is assumed to be the same, the results clearly shows different intrinsic behaviors originating from the differences in their elastic properties.

5.4 Summary

In this Chapter, the role of solute segregation on the strength and the evolution behavior of dislocation junctions was studied by utilizing kinetic Monte Carlo and 3D dislocation dynamics simulations. The different solute properties, concentration and the character of junctions were all included in the simulations in an effort to make a parametric investigation. Moreover, the preliminary study on the effect of elastic anisotropy on the solute segregation behavior was also included. The results indicate:

- Solute segregation can lead to both strengthening and weakening behaviors depending upon the evolution of the dislocation junctions.
- It is expected that the increase in the elastic anisotropy further amplifies these behaviors, owing to the increase in the segregation rates of solutes.
- The local solute concentration seems to be the more relevant parameter to characterizing the solute and dislocation interactions, due to the short-range stress fields of solutes; and its bounds are set by the unconstrained volume dilatation.

REFERENCES

[1] Rodney, D. and Phillips, R., 1999, *Phys. Rev. Lett*., **82**, 1704.

[2] Shenoy, V. B., Kukta, R. V., and Phillips, R., 2000, *Phys. Rev. Lett*., **84**, 1491.

[3] Devincre, B., Kubin, L., and Hoc, T., 2006, *Scr. Mater.*, **54**, 741.

[4] Dupuy, L. and Fivel, M. C., 2002, *Acta Mater*., **50**, 4873.

[5] Picu, R. C., 2004, *Acta Mater.*, **52**, 3447.

[6] Labusch, R., 1970, *Phys. Stat. Solidi*, **41**, 659.

[7] Mohri, T. and Suzuki, T., 1999, *"Impurities in engineering materials "*, Brian C.L. (Ed), p.259.

[8] Friedel, J., 1963, *"Electron Microscopy and Strength of Materials"*, Interscience, New York.

[9] Lebyodkin, M., Dunin-Barkowskii, L., Brechet, Y., Estrin, Y., and Kubin, L.P., 2000, *Acta Mater.*, **48**, 2529.

[10] Blavette, D., Cadel, E., Fraczkiewicz, A., and Menand, A., 1999, *Science*, **286**, 2317.

[11] Deo, C. S., Srolovitz, D. J., Cai, W., and Bulatov, V. V., 2005, *J. Mech. Phys. Solids*, **53**, 1223.

[12] Cottrell, A. H., 1953, *"Dislocations and plastic flow in crystals"*, Oxford University Press, New York.

[13] Hirth, J. P. and Lothe, J., 1968, *"Theory of dislocations"*, McGraw-Hill, New York.

[14] Yoshinaga, H. and Morozumi, S., 1971, *Philos. Mag*., **23**, 1367.

[15] Chateau, J. P., Delafosse, D., and Magnin, T., 2002, *Acta Mater.*, **50**, 1507.

[16] Sofronis, P., 1995, *J. Mech. Phys. Solids*, **43**, 1385.

[17] Sofronis, P. and Birnbaum, H. K., 1995, *J. Mech. Phys. Solids*, **43**, 49.

[18] Wang, Y., Srolovitz, D. J., Rickman, J. M., and Lesar, R., 2000, *Acta Mater*., **48,** 2163.

[19] Hu, S. Y., Li, Y. L., Zheng, Y. X., and Chen, L.Q., 2004, *Int. J. Plasticity*, **20**, 403.

[20] Picu, R. C. and Zhang, D., 2004, *Acta Mater*., **52**, 161.

[21] Monnet, G. and Devincre, B., 2006*, Phil. Mag*., **86,** 1555.

[22] Bortz, A., Kalos, M., and Lebowitz, J., 1975, *J. Comput. Phys.*, **17**, 10.

[23] Varschavsky, A. and Donoso, E., 1998, *Mater. Sci. Eng. A*, **251,** 208.

[24] Jannot, E., Mohles, V., Gottstein, G., and Thijsee, B., 2006, *Defect Diff. Forum*, **249**, 47.

[25] Cahn, R. W., *Contemp. Phys.*, 2001, **42,** 365.

[26] Chen, G. L. and Liu, C. T., *Int. Mater. Rev.*, 2001, **46,** 253.

CHAPTER 6

CONCLUSIONS

6.1 Conclusions

In this study, a computationally efficient and accurate numerical approach for anisotropic 3D dislocation dynamics was developed by numerically evaluating the derivatives of Green's functions. During the procedure of calculating the stress fields and elastic energies of dislocations, preprocessed look-up Tables were set up to reduce the demanding computational burden greatly with the error around 2%.

In Chapter 3, within the framework of fully anisotropic elasticity, the stability of perfect dislocations in three RM B2 alloys and conventional intermetallics NiAl and Fe-25Al were investigated and the results correlated well with the experimental observations. Also, the core properties of perfect dislocations in YCu, YAg, and NiAl were analyzed by generalized 2D Peierls-Nabarro model. Lower Peierls stress of [100]{110} dislocations with the pure edge and mixed character in YCu and YAg further substantiates the existence of the unusual <100> slip mode in these two ductile intermetallic compounds.

In Chapter 4, fully anisotropic 3D dislocation dynamics simulations were performed to study the evolution and interaction of dislocations in five intermetallic alloys. Owing to the large differences in their anisotropy ratios, both the operation of the Frank-Read

sources and the strength of identical junction configurations were significantly different in these alloys. These results also made the conclusion that the ductility presented in RM B2 alloys originates from the much easier generation of dislocations and their inhibited mobility at a lesser degree, in comparison to the conventional intermetallics, NiAl and Fe-25Al.

In Chapter 5, 3D dislocation dynamics simulations combined with kinetic Monte Carlo algorithm were employed to parametrically study the effects of solute segregation on the strength and the evolution behavior of dislocation junctions in fcc crystal system. The results clearly indicated both strengthening and weakening behaviors resulting from the solute segregation. Later, the solute segregation behavior was further elucidated by taking account the full elastic anisotropy. These simulations clearly indicated an increase in the rate of segregation with the increasing anisotropy factor. Therefore, it is expected that the existence of elastic anisotropy can further amplify these two opposing effects of the solute segregation.

As a summary, the main achievements of this work are:

- The importance of the elastic anisotropy on the behavior of dislocations is elucidated. An efficient methodology is presented for its inclusion into the dislocation dynamics codes.
- Results on the generation, motion, and interaction of dislocations in three RM B2 alloys as well as the analysis on the behavior of the ordinary dislocations clearly elucidate their intrinsic differences from the conventional intermetallics.

- Solute segregation can play both strengthening and weakening roles on the deformation behavior. These two opposing effects are expected to be further amplified with the increasing elastic anisotropy.

6.2 Directions for future research

6.2.1 Cross-slip of screw dislocations in intermetallics

Püschl [1] presented a very detailed review of dislocation cross-slip models and calculations. It was noted that there are three main categories for cross-slip models: line-tension approximation, linear-elastic treatment with long-distance interaction, and atomistic simulation. Simulations of cross-slip in dislocation dynamics were also performed by calculating the resolved shear stress and the corresponding probability of jumping for each possible glide plane [2-4]. In Chapter 3, the possibility of cross-slip of <111>, <100> and <110> screw dislocations in five intermetallics has been discussed based on the line tension calculation. To further understand the effects of the cross-slip behavior of screw dislocations on macroscopic mechanical properties of these alloys, it is suggested to simulate the cross-slip behavior of dislocations in these alloys by utilizing fully anisotropic 3D dislocation dynamics.

6.2.2 Boundary conditions

When dislocations move within a confined volume, the stress on dislocations should be modified with the stress terms from internal or external surfaces (free surface, crack, grain boundary, second phase particle surfaces etc.). The solution to this boundary value problem can be obtained efficiently by numerical methods including Finite Element

Method (FEM) [5] and Boundary Element Method (BEM) [6-8]. It is suggested to study the interactions between dislocations and surfaces by BEM because BEM provides certain computational advantages over the FEM due to the dynamic nature of the problems [9]. First, fewer equations need to be solved in BEM for very large number of time steps. Second, the evaluation of the image stress can be achieved directly from the nodal values of BEM solution rather than using a search and extrapolation scheme needed by FEM. In addition, BEM solution in anisotropic elasticity can also be expressed as the integral of Green's function. Similar look-up tables can make it easier to incorporate BEM into the existing anisotropic dislocation dynamics codes.

In another case, if it is considered that dislocation motions in a bulk single crystal are far from any interfaces, the materials volume can be regarded as a small part of an infinitely large single crystal and then the whole single crystal can be made up by replication of the small representative volume. For mass simulation, periodic boundary conditions (PBC) [10,11] are employed for 3D dislocation dynamics to preserve translational invariance and dislocation line connectivity and balance incoming and outgoing dislocation fluxes. It is suggested to implement PBC into fully anisotropic dislocation dynamics simulations of bulk plasticity, to eliminate the boundary effects entirely.

6.2.3 Computational efficiency

Due to the demanding computational burden arising from the complicated long-ranged interactions among large number of dislocations, parallel algorithm [12,13] has been selected as an alternative approach to solve this problem by distributing the computation

loads into several processors and execute them simultaneously. The core codes in this study have been parallelized by using standard message passing interface (MPI). It is suggested that more efforts are needed to further improve the computational efficiency and extend the range of the application of anisotropic dislocation dynamics on the study of large-scale plasticity.

References

[1] Püschl, W., 2002, *Progress in Materials Science*, **47,** 415.

[2] Rhee, M., Zbib, H. M., and Hirth, J. P., 1998, *Mod. Sim. Mat. Sci. Engr*., **6,** 467.

[3] Zbib, H. M., Rhee, M., and Hirth, J. P., 1998, *Int. J. Mech. Sci.*, **40**, 113.

[4] Quek, S. S., Xiang, Y., Zhang, Y. W., Srolovitz, D. J., and Lu, C., 2006, *Acta Mater.*, **54**, 2371.

[5] Martinez, R. and Ghoniem, N.M., 2002, *J. Comput. Mater. Science*, **3**, 229.

[6] van der Giessen, E. and Needleman, A., 1995, *Mater. Sci. Eng.*, **3**, 689.

[7] von Blanckenhagen, B., Gumbsch, P., and Arzt, E., 2001, *Mod. Sim. Mat. Sci. Engr.*, **9**, 157.

[8] El-Awady, J., Biner, S. B., and Ghoniem, N. M., 2008, *J. Mech. Phys. Solids*, **56**, 2019.

[9] Biner, S. B. and Morris, J. R., 2002, *Mod. Sim. Mat. Sci. Engr*., **10**, 617.

[10] Bulatov, V. V., Rhee, M., and Cai, W., 2001, *Mat. Res. Soc. Symp.*, **653,** Z1.3.1.

[11] Cai, W., Bulatov, V. V., Chang, J., Li, J., and Yip, S., 2003, *Phil. Mag.*, **83**, 539.

[12] Wang, Z., Ghoniem, N., Swaminarayan, S., and Lesar, R., 2006, *J. Comp. Phys.,* **219**, 608.

[13] Shin, C. S., Fivel, M. C., Verdier, M., and Kwon, S. C., 2006, *J. Comp. Phys.,* **215**, 417.

APPENDIX
PUBLICATIONS

Journal papers

Q. Chen and S. B. Biner, "Stability of perfect dislocations in rare-earth intermetallic compounds: YCu, YAg and YZn", *Acta Mater.*, 53 (2005) 3215-3223.

Q. Chen, X.-Y. Liu, and S. B. Biner, "Solute and dislocation junction interactions", *Acta Mater.*, *Acta Mater.*, 56 (2008) 2937-2947.

Q. Chen, X.-Y. Liu, and S. B. Biner, "The effects of solute segregation on the evolution and strength of dislocation junctions", *Solid State Phenomena*, 139 (2008) 65-70.

Conference proceedings

Q. Chen and S. B. Biner, "Deformation behavior in B2 intermetallic systems: fully anisotropic 3D dislocation dynamics study", *Proceedings of the Third International Conference on Multiscale Materials Modeling*, P. Gumbsch Eds., 142-145, Freiburg, Germany, 2006

Q. Chen and S. B. Biner, "Evolution and interaction of dislocation in intermetallics: Fully anisotropic discrete dislocation dynamics simulations", Advanced Intermetallic-Based Alloys, Jörg Wiezorek, Chong Long Fu, Masao Takeyama, David Morris, and Helmut Clemens Eds., (*Mater. Res. Soc. Symp. Proc.* 980, Warrendale, PA, 2007), 0980-II05-16